Deglacial changes in western Atlantic sea surface temperatures and ice sheet variability

by

Johanne Nesbø

Master thesis in Marine Geology

Department of Earth Science

University of Bergen

April 2023

Abstract

Palaeoceanographic reconstructions are required to evaluate potential future climate responses, including the sensitivity of the Greenland Ice Sheet to Arctic temperatures and the impact of a higher freshwater influx on deep-water formation. Understanding past climate fluctuations, their patterns, magnitudes, and causes is important to be able to distinguish between natural and human-induced climate change. Marine sediment cores from the North Atlantic serve as natural climate archives of past climate variability that are used to reconstruct oceanic frontal positions, ice sheet instabilities and the timing and magnitude of past rapid warm and cold oscillations. This knowledge is important for model simulations to constrain the boundary conditions of abrupt climate changes and lead to a better understanding of today's abrupt warming and its consequences.

In this study, the marine sediment core MD03-2665 from the Eirik Drift (57°26.56N 048°36.60W, 3440 m water depth) is investigated over the last deglaciation (25 000–9 000 yr BP). The oxygen isotopes of *N. pachyderma* are used together with planktic foraminiferal assemblage to portray the progression of North Atlantic climate and hydrography, while ice-rafted debris (IRD) is used to monitor changes in Greenland Ice Sheet activity. Our records show that significant amounts of IRD was present during the Last Glacial Maximum, during cold polar conditions. Isotopes and assemblages indicate the site remained north of the Polar Front and with only modest warming occurring at this location prior to a sharp warming at ~14.7 kyr BP associated with the onset of the Bølling. This sudden warming is marked by a decrease in polar *N. pachyderma* percent and $\delta^{18}O$ (by 1.1‰) suggesting a maximum warming of up to 4ºC once ice volume changes over this interval are accounted for. Subsequently, a sudden return to cold conditions, and high $\delta^{18}O$ values marks the onset of the Younger Dryas (YD). The Holocene onset is marked by a sudden warming at the end of YD and is followed by a trend toward gradually warmer but highly variable surface ocean conditions. The Arctic Front finally passes north of the site in the early Holocene and may have been even further north than today. A final distinct climate cooling occurs at 10 ky BP. The cooling is marked by a return to polar surface water conditions (*N. pachyderma* coiling ratio >95%) and an 0.89‰ increase in planktic $\delta^{18}O$ suggests temperatures might have dropped by more than 3ºC and stayed low for approximately two centuries before recovering rapidly. The prominence of the cold event in the subpolar gyre, previously documented in Greenland ice core records, suggests a role for ocean circulation in driving a regional change in circulation. Possibly triggered by a freshwater outburst, the event demonstrates that during periods of warming and ice sheet decay, ice-ocean interactions drove sudden and unexpected changes that persisted for centuries. The IRD records suggest ice sheet activity occurred both with and independent of Heinrich events and may have played an important role in modulating regional circulation and climate even in the warm interglacial period.

Acknowledgements

I would like to thank Associate Professor Dr. Helga (Kikki) F. Kleiven, Researcher Dr. Nil Irvali and Professor Dr. Ulysses S. Ninnemann for supervising this thesis and for helping me through the writing process. I appreciate the informative and honest feedback throughout the writing process and for being available for questions. Thank you for giving me the opportunity to work with such an interesting project.

I would also like to extend an additional thank you to Nil Irvali for helping me with the laboratory work and for always being available throughout this whole process. Thank you for the quick responses and always having an open door to your office. I would not have made it without you!

I would like to thank my family and friends for supporting me these years and believing in me, as well as fellow students for the great company during these years. Lastly, I would like to thank Tim for supporting me financially and emotionally during these last months and for giving me the greatest gift I could possibly imagine. I cannot wait to start this new chapter in our lives together!

Bergen, April 2023
Johanne Nesbø

Table of Contents

1 Introduction

This study contributes to the ongoing work on the sediment cores collected during the research cruise MD132 P.I.C.A.S.S.O. (Paleoclimatologie, Isotopes, Chimie, Atlantique, Séries Sédimentaires Océaniques) in the North Atlantic Ocean (Shipboard Scientific Party, 2003) which was organized under the framework of the IMAGES (the International Marine Past Global Changes Study) program.

In this thesis the near-surface ocean and ice sheet variability in the northwest North Atlantic are studied at high resolution. This thesis investigates the period from ~25–9 kyr BP using previously collected marine sediment core samples from a location south of Greenland with high sedimentation rates. This time interval spans most of the Marine Isotope Stage (MIS) 2 and the early part of MIS 1. During MIS 2, different periods of climate variability have been termed based on their climatic signals. The Last Glacial Maximum (LGM) was a period when the global ice sheets were at their maximum extent and was characterized by a cold climate (Carlson & Winsor, 2012). The retreat of the ice sheets occurred during the last deglaciation which was characterized by shifts between warmer and colder periods. The first distinct period, termed Heinrich Stadial 1 (HS1), is regionally characterized by periods of high deposition of terrigenous sediment from icebergs discharging from the Laurentide Ice Sheet (LIS), possibly as a result of ice sheet build-up and collapse (MacAyeal, 1993). Following this period is the warmer Bølling-Allerød (B/A) interstadial from ~14.6–12.8 kyr which is marked by a distinct decrease in stable oxygen isotope records (Rasmussen et al., 2014). The Younger Dryas (YD) is a cold period hypothesized to be a result of increased freshwater fluxes to the oceans (Broecker et al., 1988); most likely from the LIS (Carlson et al., 2007). Increased meltwater is hypothesized to have affected salinity and density of the surface water in the North Atlantic, which can cause reductions in thermohaline circulation and cause climate change. Reconstructions of ocean circulation indicate that large changes occurred during the YD (McManus et al., 2004). A rapid warming at the end of YD marks the end of the last deglaciation, and the onset of the current interglacial period, the Holocene, beginning at ~11.7 kyr.

The studied material is from the marine sediment core, MD03-2665 (57º26.56N, 048º36.60W; 3440 m water depth), from the Eirik Sediment Drift south of Greenland, a high sedimentation

rate site ideally located to monitor millennial-centennial-timescale oscillations in climate, surface ocean hydrology and Greenland Ice Sheet activity.

This thesis has been supervised by Associate Professor Dr. Helga (Kikki) F. Kleiven, Researcher Dr. Nil Irvali and Professor Dr. Ulysses S. Ninnemann from the Department of Earth Science and the Bjerknes Centre for Climate Research at the University of Bergen. The stable isotope analyses have been done at the Facility for advanced isotopic research and monitoring of weather, climate, and biogeochemical cycling (FARLAB).

1.1 Aim of this study

Knowledge of the climate of the past is important to be able to distinguish natural climate changes from those caused by human emissions. Understanding the response of the Greenland Ice Sheet, sea surface climate variability and the ocean currents in the North Atlantic in the past can contribute to new insights into how this mighty ice sheet and surrounding regions will respond to increased global warming in the future. Contemporary observations of the Greenland Ice Sheet and the North Atlantic are too short (<100 years) to inform our understanding of future climate change and feedbacks over multi-decadal to centennial timescales (Dickson, 1995). Therefore, paleo reconstructions of periods that underwent large-scale rapid climate reorganization in the recent geological past offer considerable potential for understanding ice-sheet-ocean dynamics, thereby extending the short observational window.

Until recently, there have been very few coring sites from the North Atlantic region that have had the opportunity to reconstruct glacial-interglacial climate variability and ocean currents with a high time resolution (centennial-multidecadal). One of the reasons has been the lack of long Pleistocene sediment cores. Access to new marine sediment cores from the International Ocean Discovery Program (IODP) and IMAGES program enabled new opportunities, and the published high-resolution interglacial datasets from the northwest Atlantic show the significance of the Atlantic Meridional Overturning Circulation (AMOC) in the climate system and act as the marine analogues of the Greenland ice cores (e.g., Kleiven et al., 2008; Irvali et al., 2012; Galaasen et al., 2014; Irvali et al., 2016; Galaasen et al., 2020; Irvali et al., 2020). The reconstruction of changes in temperature and salinity in both surface and deep water masses is based on stable isotope analyses, sea surface temperature reconstructions and sedimentological analyses on the sample material obtained from the Eirik Sediment Drift cores

just south of Greenland's southern tip. These sediments contain proxies which can be used to portray variations in meltwater and calving from Greenland, calculate paleocurrent strength, and reconstruct the properties of surface and deep-water masses that are of great importance for understanding the past, present and future of the Earth's climate. Previous studies on the Eirik Drift have focused on resolving millennial-centennial-scale climate change during interglacial periods. These studies have found a strong correlation between freshwater forcings and reduced deep water ventilation (Kleiven et al., 2008; Galaasen et al., 2014; Galaasen et al., 2020). During previous interglacials, when the climate was warmer than present, Irvali et al. (2012), Irvali et al. (2016) and Irvali et al. (2020) also found evidence for rapid climate oscillations with rapid cooling events occurring both during the last interglacial (MIS 5e) and the previous three interglacials over the last 450 kyr. While previous studies from the Eirik Drift have focused on interglacial periods, this Master of Science Project will focus on the last deglaciation from 20 000 to 9 000 yr BP. The results from this thesis can be further used in models that simulate past, present, and future climate changes.

1.2 Objectives

- To analyze the variability in surface ocean masses and Greenland Ice Sheet activity during the deglaciation from IMAGES Core MD03-2665.
- Test whether the climatic signal in the northwestern Atlantic Ocean can be correlated to the signal seen in Greenland (ice cores) and the broader North Atlantic (marine sediment cores) using sea surface temperature/salinity reconstructions and ice-rafted debris from Core MD03-2665.

1.2.1 Test: Resolve deglacial changes in northwest Atlantic Ocean climate, hydrography circulation and ice sheet variability

In this study the climate variability in the northwest North Atlantic will be studied in greater detail with the application of new analytical methods on a sediment core. The material used is a marine sediment core (MD03-2665) previously obtained which spans the last deglaciation (20 000–9 000 yr BP). The aim of this study is 1) to analyze the ocean-atmosphere circulation changes at a high resolution over this period focusing on near-surface ocean temperature variability and changes in oceanic front positions, 2) to reconstruct ice sheet variability using IRD and stable isotope analyses.

2 Background

2.1 The climate system

The Earth's climate is a complex system consisting of multiple components responding to different forcings. These different components are the atmosphere, oceans, lithosphere, cryosphere and biosphere. There are three mechanisms that act as natural forcings of the climate system: the Earth's orbit around the sun, the strength of the sun and tectonic processes. A fourth factor influencing the climate is anthropogenic forcing (greenhouse gases) (Ruddiman, 2014, p. 8). A mechanism influencing the forcings are a process called feedback. Feedbacks either amplify (positive) or reduce (negative) the effect of an initial forcing and act as self-regulating processes operating at different rates until a new climate state has reached equilibrium (Cronin, 2010, pp. 18-19). These forcing mechanisms cause changes and variations in the global climate, and the observed changes are referred to as responses. The responses in the climate system i.e., climate variability and its physical characteristics, are often recorded and preserved in various climate archives such as terrestrial lake sediments, ocean sediments and glacial ice. These archives can be analyzed to reconstruct past climate behavior (Ruddiman, 2014, pp. 10, 56-58).

The incoming solar radiation to the Earth's surface accounts for most of the heat on the Earth. Unequal distribution of the radiation accounts for the temperature differences observed in lower and higher latitudes. In higher latitudes, incoming radiation is spread over a larger geographical area than at lower latitudes, as the sunbeams hit at an indirect angle. An effect that accounts for increasing the latitudinal temperature difference further is the Earth's surface reflecting back some of the solar radiation. The percentage of reflected radiation from a surface is referred to as albedo. The albedo of a surface depends on how light or dark the surface is. Snow and ice in high latitudes have an albedo of 60–90% whereas open ocean reflects less than 5% of the radiation. Since the Earth's surface is mostly covered by open oceans, the average albedo of the Earth is approximately 10% (Ruddiman, 2014, pp. 20-24).

The climate in polar regions tends to respond faster to forcings, especially greenhouse gases, than the tropical regions. Rapid warming in the polar regions compared to lower latitudes in response to forcings have been observed in climatic records as well as in modeled studies (e.g., Screen & Simmonds, 2010; Taylor et al., 2013) and is known as polar amplification. These

studies have suggested that diminishing snow and sea ice coverage in higher latitudes are the largest contributing factor to polar warming as the surface albedo reduces. When the global climate changes, polar regions respond faster and more extremely than the tropics, especially in the Northern Hemisphere, both in terms of warming and cooling events (Cronin, 2010, p. 21).

2.2 The thermohaline circulation

The thermohaline circulation (THC) is the movement of global ocean currents driven by differences in temperature (thermo) and salinity (haline) that result in density gradients in different regions of water. Warm waters are transported northwards to the North Atlantic where the water cools and sinks to the bottom. The water is then transported southward as North Atlantic Deep Water (NADW) along the western Atlantic basin where some continues as deep and bottom flows into the Indian and Pacific Oceans and some rises towards the surface in the Antarctic region (Clark et al., 2002; Rahmstorf, 2002). The reason for the upwelling in the Antarctic region is because of the topography in the area, where the water has no other option than to flow upwards. Waters are then transported northwards again as surface flows creating a circulation pattern with surface waters from south to north, and deep currents from north to south (Figure 2.1) (Rahmstorf, 2002).

Components of the THC includes deep-water formation, spreading and upwelling of deep waters and surface currents. In the North Atlantic, deep-water formation takes place in the Labrador Sea (LS) and in the Greenland–Norwegian Sea. In the South Antarctic, deep-water formation occurs in the Ross Sea and Weddell Sea. The formation occurs when dense water sinks, and this creates vertical mixing in the water column. The spreading of the global deep-water currents is a result of the topography and bathymetry of the ocean basins, creating paths for the deep waters to flow. Upwelling of deep-water is thought to mainly occur in the South Atlantic region though it is difficult to observe. The last component of THC, the surface currents, are driven by the global wind systems and Earth's rotation and close the loop of the conveyor-like THC circulation. Meridional Overturning Circulation (MOC) is a concept of north-south flow relative to latitude and depth and is closely linked to the THC. The main difference between the THC and the MOC is that the MOC includes wind-driven cells called the Ekman cells (Rahmstorf, 2006).

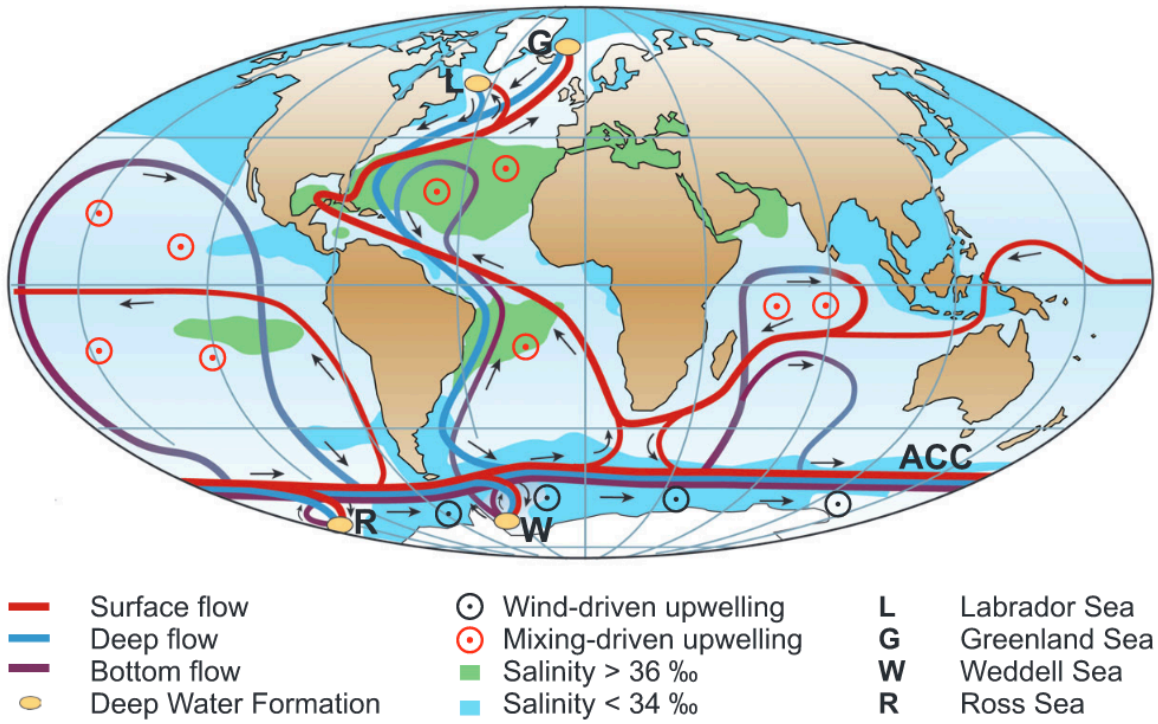

Figure 2.1: Simplified overview of the global ocean circulation. Surface currents are shown in red, deep currents in blue and bottom currents in purple. Deep-water formation areas are marked in yellow and upwelling areas are marked in black (wind-driven) and red (mixing-driven) circles. Waters with high salinity (>36‰) are marked in green, and low-salinity waters (<34‰) in light blue. From Rahmstorf (2006).

The THC has three stable modes depending on the climatic state of the North Atlantic (Weaver & Hughes, 1994). These modes have been termed interstadial, stadial or Heinrich mode, based on their occurrence in different glacial climatic stages, or warm, cold and off mode based on their physical properties observed in the North Atlantic (Figure 2.2). During periods of colder climate, the North Atlantic THC was weakened and NADW formation occurred south of Iceland. In warmer periods, the North Atlantic THC was stronger and NADW formation occurred in the Nordic Seas. During the off mode, no NADW formation occurred, and Antarctic waters supplied the Atlantic basin (Weaver & Hughes, 1994; Rahmstorf, 2002)

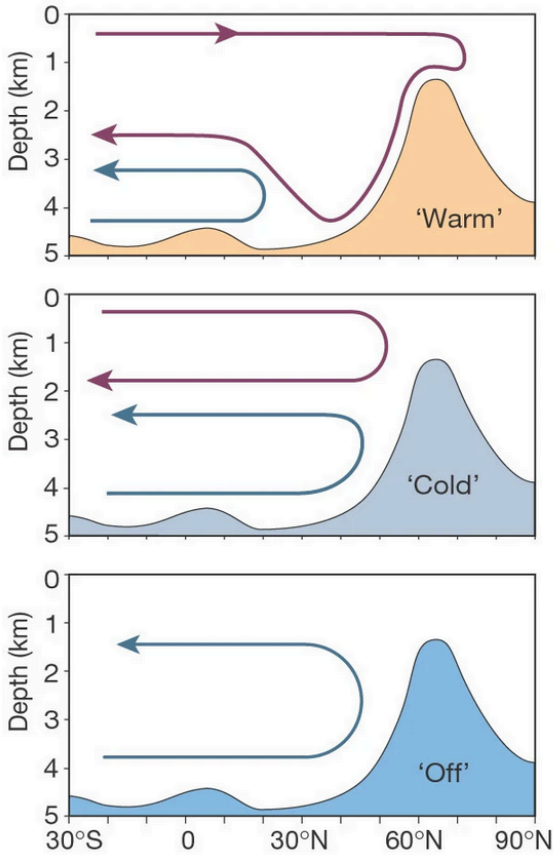

Figure 2.2: Schematic section along the North Atlantic, showing the three modes of ocean circulation: "Warm", "Cold", and "Off" mode. North Atlantic overturning is shown by red line, Antarctic bottom water by blue line. From Rahmstorf (2002).

The THC has a major impact on the global climate as it is important for redistribution of heat to higher latitudes. Changes in the THC can alter the global climate by changing the climatic state in and out of glacial and interglacial periods. Mixing of freshwater into high-latitude surface waters, making the waters less saline and lighter, can interfere with deep-water formation as the surface waters are too light to sink (Broecker & Denton, 1990; Dickson & Brown, 1994). It has been hypothesized that freshwater fluxes are responsible for short periods of cooling seen in climatic records (e.g., Younger Dryas and the 8.2 kyr B.P. event) localized in the North Atlantic region when the THC slowed (Broecker et al., 1988), which later has later been verified (e.g., Kleiven et al., 2008; Ng et al., 2018).

2.3 Deglaciation of the Greenland Ice Sheet

The last major glaciation in the Northern Hemisphere occurred during a period termed the Last Glacial Maximum (LGM). During the LGM most of the Northern Hemisphere ice sheets were at their maximum extent ~26 000 years ago and the climate was cold (Carlson & Winsor, 2012). The Greenland Ice Sheet (GIS) (Figure 2.3) extended out on the continental shelf and operated as a marine terminating glacier, releasing icebergs into the ocean. After the LGM, the GIS started to retreat off the continental shelf encountering numerous advances or still-stands in the process, before retreating within the modern coastline at the latest by ~10 000 yr BP (Bennike & Björck, 2002; Young et al., 2020).

During the LGM, the sea level was ~120 m lower than today (Stanford et al., 2011a). As a result of the retreat of the Northern Hemisphere ice sheets the sea level started to rise. The sea level rise has varied in magnitude with elevated rates during certain intervals (20 000–19 000 yr BP, 14 500–13 500 yr BP, 11 500–10 500 yr BP) which has been correlated to an increased retreat of multiple ice sheets (PALSEA members, 2010; Carlson & Winsor, 2012; Deschamps et al., 2012).

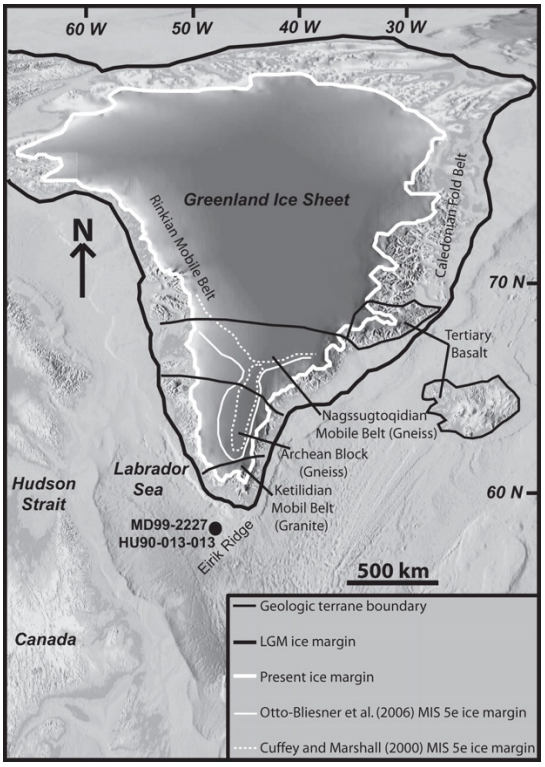

Figure 2.3: The modern and LGM extent of the Greenland Ice Sheet (GIS). From Carlson et al. (2008).

The retreat of the GIS had begun at ~20 000–19 000 yr BP as a response to the warming into the last deglaciation. At the beginning, the GIS fluctuated greatly with re-advances and retreats until the Bølling-Allerød (B/A) warming where increased ablation and runoff occurred (Carlson et al., 2008). The GIS's response to the YD cooling has been observed by a continued retreat of the southern and eastern GIS despite the cold climate (Williams, 1993; Jennings et al., 2006; Carlson et al., 2008).

From the southern Greenland, the oldest radiocarbon dates stems from different climate archives indicating that the GIS retreated on land by the latest at ~10 600 yr BP (Bennike & Björck, 2002), or even as early as 14 100 yr BP (Bennike, 2002). The oldest radiocarbon age of 14 100 yr BP stems from an isolated island off the Greenland mainland giving this age an uncertainty of whether the GIS had retreated on land or still was a marine terminating glacier. The ~10 000 yr BP ages are more certain and is generally the accepted age constrain on the southern Greenland continental shelf retreat (Bennike & Björck, 2002).

3 Study area

The marine sediment core studied in this thesis was retrieved from the Eirik Sediment Drift. The drift is located southwest of the Greenland margin off the tip of Cape Farewell, Greenland's southernmost point. Core MD03-2665 (57°26.56N 048°36.60W, 3440 m water depth) was retrieved using a giant square corer (CASQ) onboard *RV Marion Dufresne,* 13th of June 2003 (Figure 3.1). The core was retrieved as part of the P.I.C.A.S.S.O. (Paleoclimatologie, Isotopes, Chimie, Atlantique, Séries Sédimentaires Océanique) expedition in the South and North Atlantic Ocean.

3.1 Bathymetry

The barrier of ridges collectively termed the Greenland–Scotland Ridge (GSR), that separates the North Atlantic Ocean and Nordic Seas, plays a key role in the heat transport between the northern and southern basins (Figure 3.1). Warm, saline waters flow northward in the surface layers on the eastern side of the basin while cold, fresh waters flow southward on the western side of the basin. The flow is in the surface layers and sometimes at greater depths where the topography allows it, for instance east of Greenland. The exchange of water is steered by the bathymetry and the Coriolis force and has an important function in the global THC including heat transport to northwestern Europe (Hansen & Østerhus, 2000).

The GSR extends from the east coast of Greenland to Scotland (Figure 3.2) with a maximum depth of 840 m. The ridges are characterized by three depths divided by Iceland and the Faroe Islands where deep water from the Nordic Seas flows through. Between Greenland and Iceland, the relatively wide Denmark Strait have a depth of 620 m. Further east, the Iceland-Faroe Ridge between Iceland and the Faroe Islands have minimum depths of 300–500 m with increasing depth eastward toward the Faroe Islands. Between the Faroe Islands and Scotland, there is one channel and one ridge divided by the Faroe Bank below the sea surface. Between the Faroe Islands and the Faroe Bank, the Faroe Bank Channel extends 840 m below sea level. Between the Faroe Bank and Scotland, the Wyville–Thomson Ridge extends down to 600 m (Hansen & Østerhus, 2000).

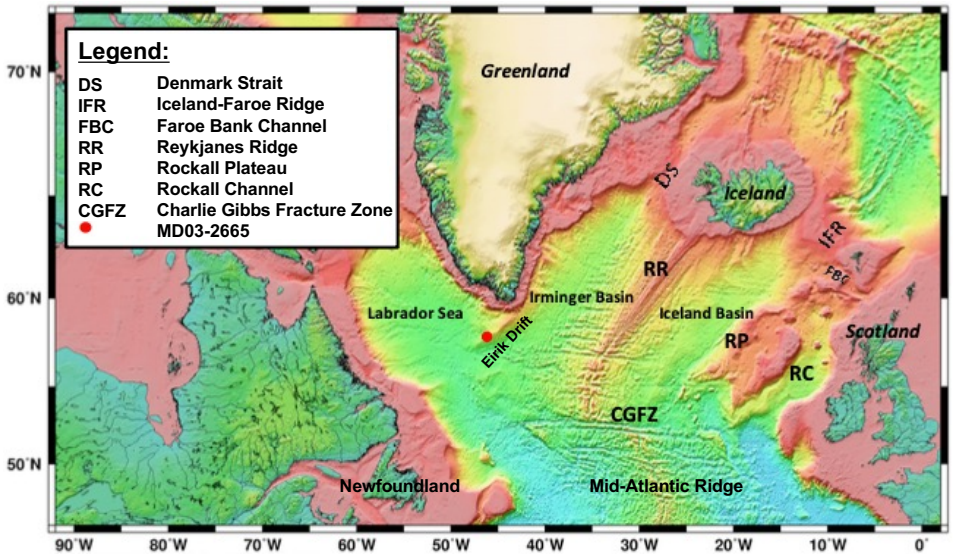

Figure 3.1: Bathymetric map of the North Atlantic. Core MD03-2665 is marked in a red dot. Modified from Smith and Sandwell (1997).

Southwest of the GSR the bathymetry is characterized by three basins. The Irminger Basin is separated from the Iceland Basin by the Reykjanes Ridge (RR). The RR is a part of the Mid-Atlantic Ridge (MAR) that is divided by the Charlie Gibbs Fracture Zone (CGFZ). The two other basins, the Iceland Basin and the Rockall Channel in the east is separated by the Rockall Plateau. The Nordic Seas and the Arctic Ocean are located north of the GSR. The Nordic Seas includes the shallow Barents Sea and the deeper Greenland Sea, the Iceland Sea and the Norwegian Sea. West of the Irminger Basin, separated by the Eirik Drift, the Labrador Sea is located (Hansen & Østerhus, 2000).

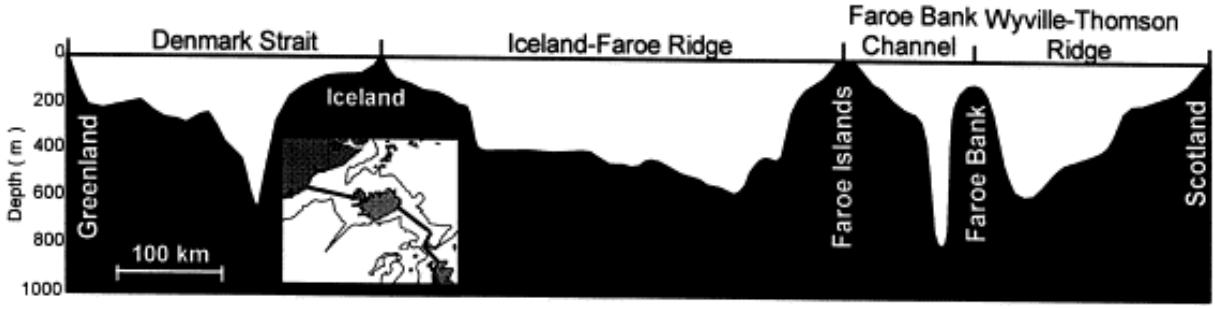

Figure 3.2: Cross-section of the Greenland-Scotland Ridge following the highest points along the ridge shown on the inset map. From Hansen and Østerhus (2000).

3.2 Oceanography

The oceanography in the North Atlantic is composed of surface currents and deep currents redistributing heat and transporting warm and cold waters. The near-surface currents are responsible for heat distribution to northwestern Europe and the return of cold, fresher water southwestward along the Greenland margin. The deep ocean currents flow along the ocean floor and are responsible for the deposition and formation of large sedimentary bodies like the North Atlantic sedimentary drifts, from which this thesis is based on (Stanford et al., 2011b). The following subchapter provides an introduction to the surface and deep ocean currents circulating in the North Atlantic.

3.2.1 Surface ocean circulation

Iselin (1936) proposed to use the terminology "Gulf Stream System" for the previously known Gulf Stream (GS) to differentiate between the currents with different properties across the North Atlantic. The Gulf Stream System consists of three currents where two of these, the Florida Current and the GS, flows from southwest to northeast. The third, the North Atlantic Current (NAC), is defined by Iselin (1936) as all other currents flowing eastward and northward from Newfoundland.

The NAC is initiated east of Newfoundland from a branch of the warm GS water combined with colder water from the inshore Slopewater Jet (SJ) and the Labrador Current (LC) (Figure 3.3). At 40ºN and 46ºW, NAC act as a western boundary current flowing northward, but at 51ºN the NAC turns eastward and is no longer a part of the boundary current but rather a free-flowing current extending the GS. On its way eastwards it is directed through the CGFZ in the MAR and split into several branches. The northward branches of the NAC flows into the Nordic Seas where some returns into the East Greenland Current (EGC) (Talley et al., 2011, pp. 259-260). The westward branch of the NAC flows south of Iceland as the Irminger Current (IC) splitting into new branches by the northwestern coast that either flows northwards into the Nordic Seas or southwestwards joining the EGC (Figure 3.4). The EGC flows southward along the eastern Greenland coast. Turning north at the southern tip of Greenland, the EGC turns into

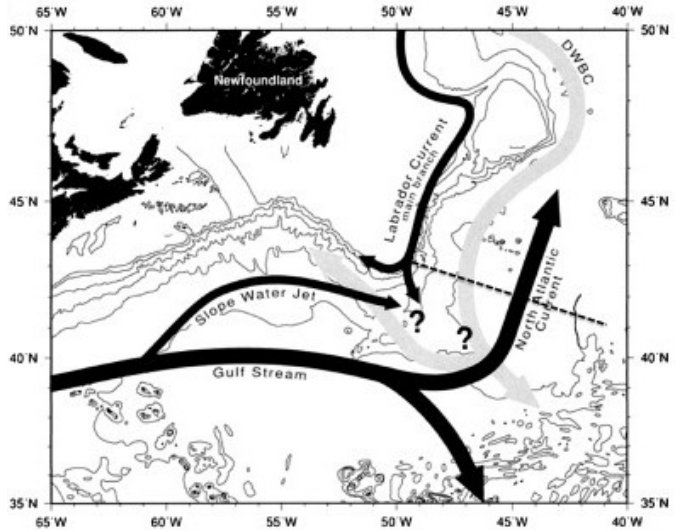

Figure 3.3: Predecessors of the North Atlantic Current (NAC). Water from the Gulf Stream mixes with water from the Slope Water Jet and the Labrador Current before continuing northeastward as the NAC. From Pickart et al. (1999).

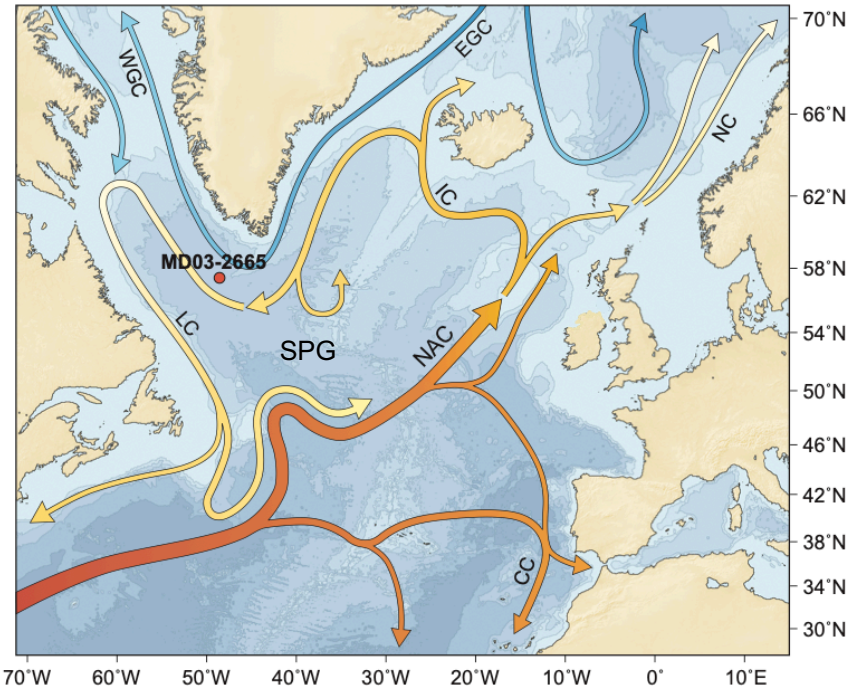

Figure 3.4: Map illustrating surface currents in the North Atlantic and Nordic Seas. The location of core MD03-2665 is shown in a red circle. WGC – West Greenland Current, EGC – East Greenland Current, LC – Labrador Current, IC – Irminger Current, NC – Norwegian Current, NAC – North Atlantic Current, CC – Canary Current. The boundary of the subpolar gyre (SPG) follows the NAC from south to north, the IC westward and the LC southeastward creating a semi-circular pattern. Modified from Irvali et al. (2016).

the West Greenland Current (WGC) flowing northwards before turning south into the Labrador Current (LC). The LC mixes with Arctic waters originating north in the Baffin Bay area west of Greenland. The subpolar circulation includes the northeastward branches of the NAC. The two branches flowing northwards either into the Iceland Basin or the Rockall Through both join the Iceland-Faroe Front at the Iceland-Faroe Ridge flowing into the Norwegian Current (Talley et al., 2011, p. 262).

The subpolar gyre (SPG) is strongly controlled by the bathymetry in the North Atlantic. The IC forms the northeastern branch of the gyre carrying warm and saline waters west and continues as the branch joining the EGC. The northern branch follows the eastern and western Greenland margins as the EGC and the WGC before turning south as a part of the LC forming the western part. The EGC and the LC are western boundary currents that are linked by the eastern boundary current, the WGC, and is part of the cyclonic SPG. The eastward turn of the LC outside Newfoundland joins the NAC to form the southern branch of the SPG. When branches of the NAC joins the IC, the SPG is closed. The anticyclonic subtropical gyre (GS and NAC) consists of strong western boundary currents and weaker eastern boundary currents, like the Canary Current that originates from branches of the NAC (Talley et al., 2011, pp. 252, 262).

3.2.2 Deep ocean circulation

The deep flow pattern of the North Atlantic is largely controlled by bathymetry. In the North Atlantic basin there are distinct deep water masses with different origin. Iceland–Scotland Overflow Water (ISOW) and Denmark Strait Overflow Water (DSOW) originate north of the GSR and flow across the ridge, whereas Labrador Sea Water (LSW) is formed in the Labrador Sea. West of the Greenland coast they merge to form the North Atlantic Deep Water (NADW) that flows westward along the Greenland margin before turning south following the bathymetry of the Labrador basin as the Deep Western Boundary Current (DWBC) that spreads south in the deep Atlantic basins. Antarctic Bottom Water (AABW) is the densest global-scale water mass and underlies the other water masses in the North Atlantic Ocean. It is produced around Antarctica, sinks along the Antarctic continental slope and spreads northward to fill most of the ocean deeper than 4 km (Orsi et al., 1999) (Figure 3.5).

The LSW is formed in the Labrador Sea and the Irminger Sea and is warm and shallow compared to the other water masses (Dickson & Brown, 1994; Pickart et al., 2003). It resides at intermediate depths of 700 to 1500 m. The DSOW and ISOW overflows the GSR with DSOW overflowing the Denmark Strait and ISOW the Faroe Bank Channel. The DSOW is fresher than ISOW because of mixing with the fresh LSW and lesser difference in salinity with overlying water masses (Dickson & Brown, 1994).

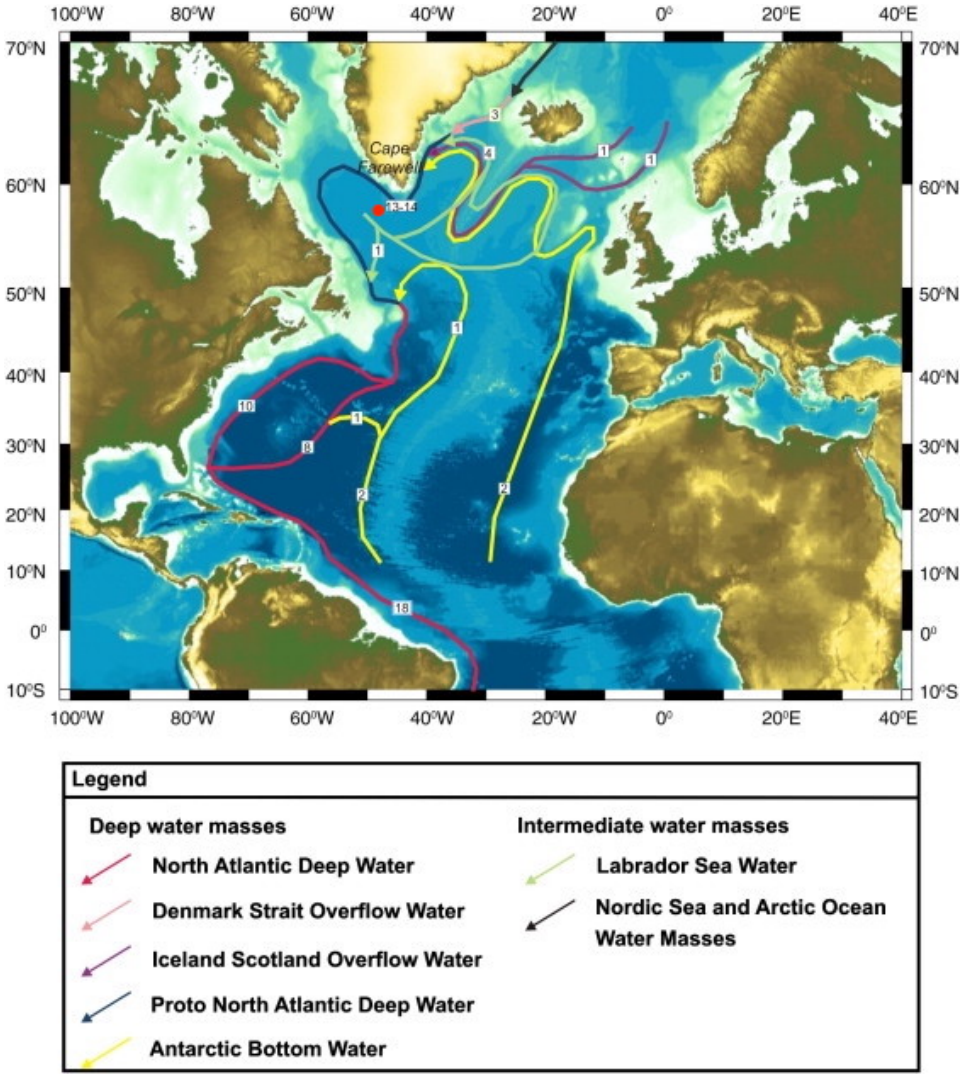

Figure 3.5: Map illustrating the deep currents in the North Atlantic. Boxes indicate water volume flux in Sverdrup (Sv). Red circle indicates the core location of MD03-2665. Modified from Stanford et al. (2011b).

DSOW is a mixture of several different water masses that originate from different regions and its sources comes from the Arctic Ocean and the Nordic Seas (Rudels, 2002; Tanhua et al., 2008; Våge et al., 2013). Mixing of different water masses in the Arctic Ocean and Nordic Seas, such as the re-circulation of Atlantic Water and Arctic Atlantic Water, as well as Polar Deep

Water and Arctic Intermediate Water, becomes almost homogenous upon entering the DSOW. The less dense Polar Intermediate Water in the upper layer also contributes to the DSOW (Rudels, 2002). The DSOW has a potential temperature of 0 to 1 ºC and a salinity of 34.9 when it overflows the Denmark Strait and is the coldest and densest water mass contributing to the NADW (Swift, 1984; Dickson & Brown, 1994).

The ISOW starts as a relatively fresh water mass but mixes with warm and saline waters from the thermocline resulting in a high salinity water mass that flows southwards. AABW originates from the Antarctic regions and are formed in various sites on the Antarctic continental shelf (Dickson & Brown, 1994). This water mass has low salinity and low oxygen levels and is defined by McCartney (1992) as waters colder than 1.8ºC. On its way northward, about half of the AABW volume that crosses the equator warms, mixes and transforms to Lower Deep Water (LDW), the modified water mass of AABW (Dickson & Brown, 1994).

After spilling over the GSR, the ISOW sinks and follows the bathymetry south in the Iceland Basin along the RR, before turning northward at the CGFZ and into the Irminger Basin. The LDW is directed by the Rockall Plateau on its way northward and flows into the Iceland Basin before flowing south again following the same path as the overflows (Dickson & Brown, 1994). The water masses mix intensely creating a nearly homogenous product with an elevated salinity signal compared to the deep water masses west of the CGFZ (McCartney, 1992). During their travel through the Iceland and Irminger Basins the waters entrain LSW. When entering the northwestern coast of Greenland south of the Denmark Strait, these combined water masses meet DSOW which is further mixed into the water mass creating proto–NADW. The proto–NADW, now containing a combination of the overflows (DSOW and ISOW), LSW and LDW, continues westward along the coast of Greenland as a deep western boundary current (DWBC), before turning south in the northwestern Labrador Basin. Continuing southwards along the Canadian coast it mixes with more LSW and AABW forming the fully developed NADW east of Newfoundland (Hunter et al., 2007).

3.3 Sedimentary drifts

A climate archive normally unsuitable for monitoring and reconstructing short-term rapid climate variations are deep-ocean sediments. The reason for this is the slow open ocean sedimentation rates of normally 1–2 cm/kyr and often additional bioturbation of the top 5–10 cm in the bottom sediments. This can provide problems when investigating climate fluctuations on millennial to sub-millennial timescales. However, there are locations in the North Atlantic (Figure 3.6) where deposition exceeds the normal sedimentation rate with up to 10–20 cm/kyr. Marine sediment cores from these locations have been frequently used for high-resolution climate fluctuation studies (Ruddiman, 2014, p. 297) and is thus also the focus area for this thesis.

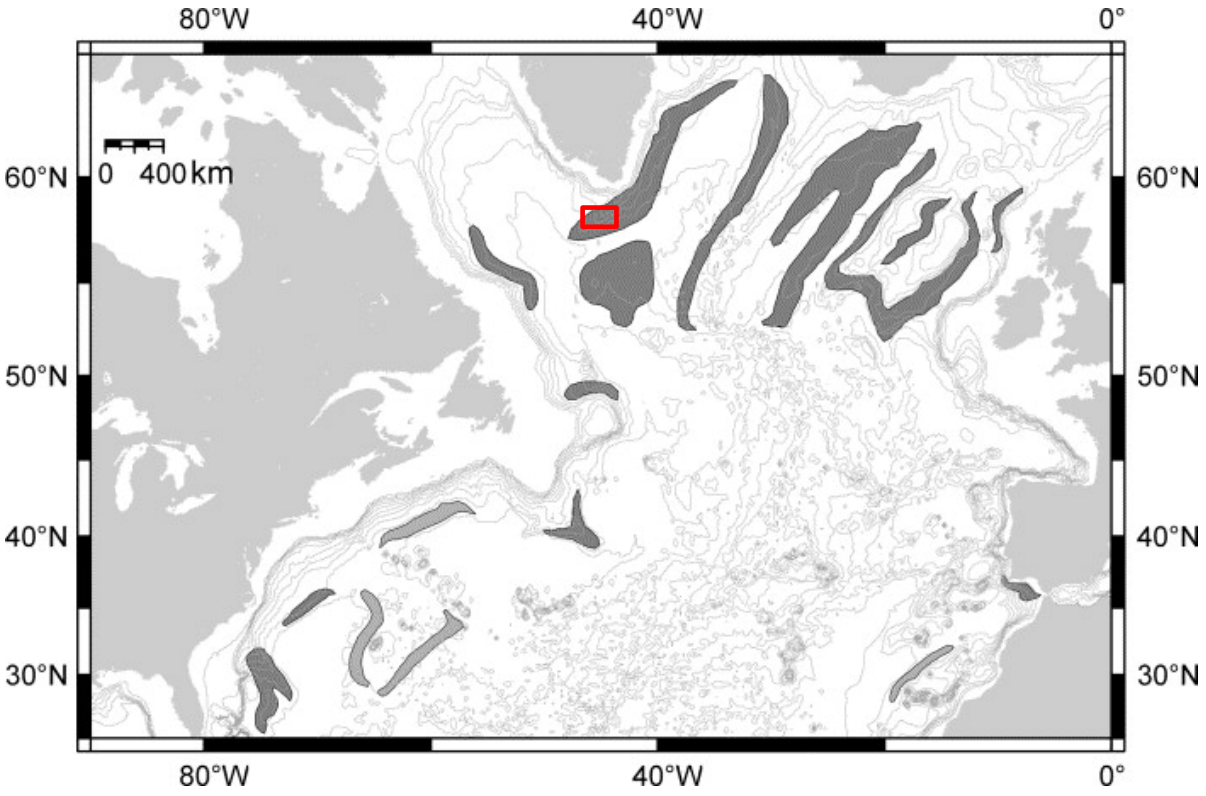

Figure 3.6: Distribution of sediment drifts in the North Atlantic. The Eirik Drift study area is marked with a red box. Modified from Faugères et al. (1999).

Ocean currents transport sediment in suspension, usually fine grained, and deposit them when the currents slow in what is called sediment drifts (Jones et al., 1970). Sediment drifts are defined as accumulation of sediment influenced by currents with no distinct geometry. The water masses high in sediment that are responsible for deposition of drifts is termed the

nepheloid layer (Wold, 1994). If a deposit is mainly influenced by bottom currents, it can be termed a contourite drift (Stow et al., 2002). As first demonstrated by Heezen et al. (1966), these contourites are controlled by deep geostrophic contour currents. Bottom currents are native to the deep-water, still it is possible to call deposits in shallow water a contourite. Therefore, Stow et al. (2002) suggested setting an upper limit of 300 m water depth for when to term a deposit a contourite drift, and rather use the term shallow contourite for depositions in shallower water. Since contourite drifts accumulate in areas where the strength in bottom currents decline, they can be used as paleoceanographic tracers for bottom currents (Jones et al., 1970).

Another good reason for studying sediment drifts are that coarser sediment, including foraminifera and ice-rafted debris, tend to remain in place as they are difficult for bottom currents to move, hence, climate fluctuations on several timescales are preserved under the rapidly deposited fine-grained sediment laden currents (Ruddiman, 2014, p. 298). Climate proxies are chemical and physical properties which is recorded in different climate archives, and they work as a replacement for direct temperature measurements.

3.3.1 The Eirik Drift

The Eirik Drift is a sediment drift south of Greenland (Figure 3.7) and is classified as an elongated mounded drift. This type of drift has a very distinct mounded and elongated shape. The size of an elongated mounded drift can vary in length from a few 10s of km to over 1 000 km. The thickness can be up to 2 km and the length-width ratio varies from 2:1 to 10:1. Elongated mounded drifts can be found in all ocean basins and are especially common in the North Atlantic. Further, the Eirik Drift is classified as a detached drift indicating current activity on both sides of the drift (Stow et al., 2002). The Eirik Drift covers an area of 10.3×10^4 km^2 and has a volume of 6.8×10^4 km^3 being one of the medium sized drifts in the northern North Atlantic (Wold, 1994).

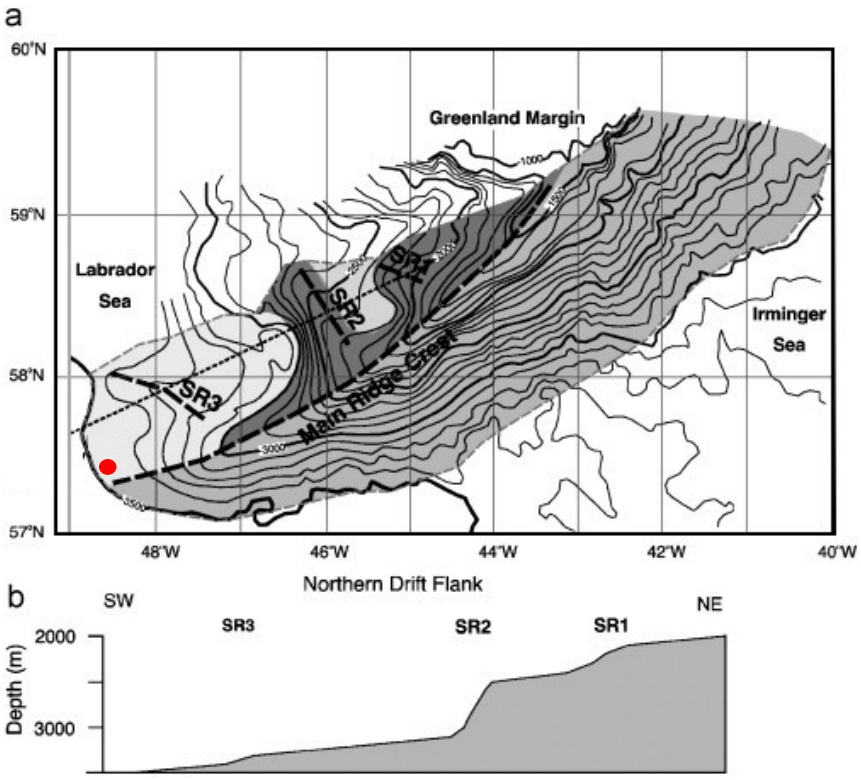

Figure 3.7: a) Bathymetric map of the Eirik Drift with ridge crests illustrated as dashed lines. Secondary ridge crests are marked as SR1-3. Darker shaded areas indicate steeper slopes on the drift. The core location is indicated by a red circle. b) Cross-section of the flank indicated by a dotted line. Modified from Hunter et al. (2007).

The accumulation on the Eirik Drift results from a combination of vertical deposition of biogenic, terrigenous and glaciomarine material, along slope transport of sediments by bottom currents, and lateral deposition from turbidity currents and processes that produce spillover from the continental shelf. Sediment deposited in the Holocene largely stems from the Nordic Basaltic Province close to the Denmark Strait and has been transported by the DSOW. Large volumes of ice-rafted debris can be found below 2500 m depth (Davies et al., 2021).

Sediment accumulation on the Eirik Drift started at 4.5 Ma in the Pliocene. Increased accumulation occurred after 3.2 Ma, possibly due to higher sediment flux and bottom current activity (Arthur et al., 1989). The high accumulation rates during interglacial periods such as the Holocene and Marine Isotope Stage (MIS) 5e (up to ~50 cm/kyr) are in contrast to the lower rates observed during glacial stages (e.g., 10-15 cm/kyr in MIS 2) (Hillaire-Marcel et al., 1994). Today, the Eirik Drift is no longer considered an active drift (Hunter et al., 2007) but Holocene sediments have been found on the drift toe (Hillaire-Marcel et al., 1994).

4 Material and Methods

4.1 Core MD03-2665

The core studied in this thesis, MD03-2665, is a 11.18 m long giant square core (CASQ) and covers the whole Holocene interglacial, the deglacial and the Last Glacial Maximum (LGM). The core was split onboard into eight sections of 155 cm and further into working halves and archive halves. Core photos (Appendix A) and description of the core were done onboard during the expedition. The core sediment consists of silt and clay with laminations in the top, middle and bottom part of the core (Figure 4.1). Core samples from the 400–700 cm interval is used in this study.

4.2 Laboratory work

4.2.1 Sampling

Core MD03-2665 was sampled every 1 cm from 0–700 cm prior to this study. Distilled water was added to the samples, and they were shaken for 12 hours to disperse the sediment. After this, the samples were wet sieved into >150 µm, >63 µm and <63 µm fractions. Both the >150 µm and >63 µm fractions were dried and moved to samples glasses, whereas the < 63 µm fraction was left to settle in a beaker, dried and put in a sample bag (Kleiven et al., 2008, Suppl.). Foraminifera and mineralogic grains from the >150 µm fraction were used for planktic foraminiferal assemblage counts, stable isotope analyses and lithic counts.

4.2.2 Stable isotope analyses

Prior to this study, stable isotope analyses of oxygen ($\delta^{18}O$) were performed every 1 cm of the core. The planktic foraminifera *Neogloboquadrina pachyderma* sinistral (*N. pachyderma*) from the 150–250 µm fraction was selected to reconstruct palaeoceanographic conditions. In preparation for the analyses, *N. pachyderma* shells were rinsed in methanol for 20 seconds to

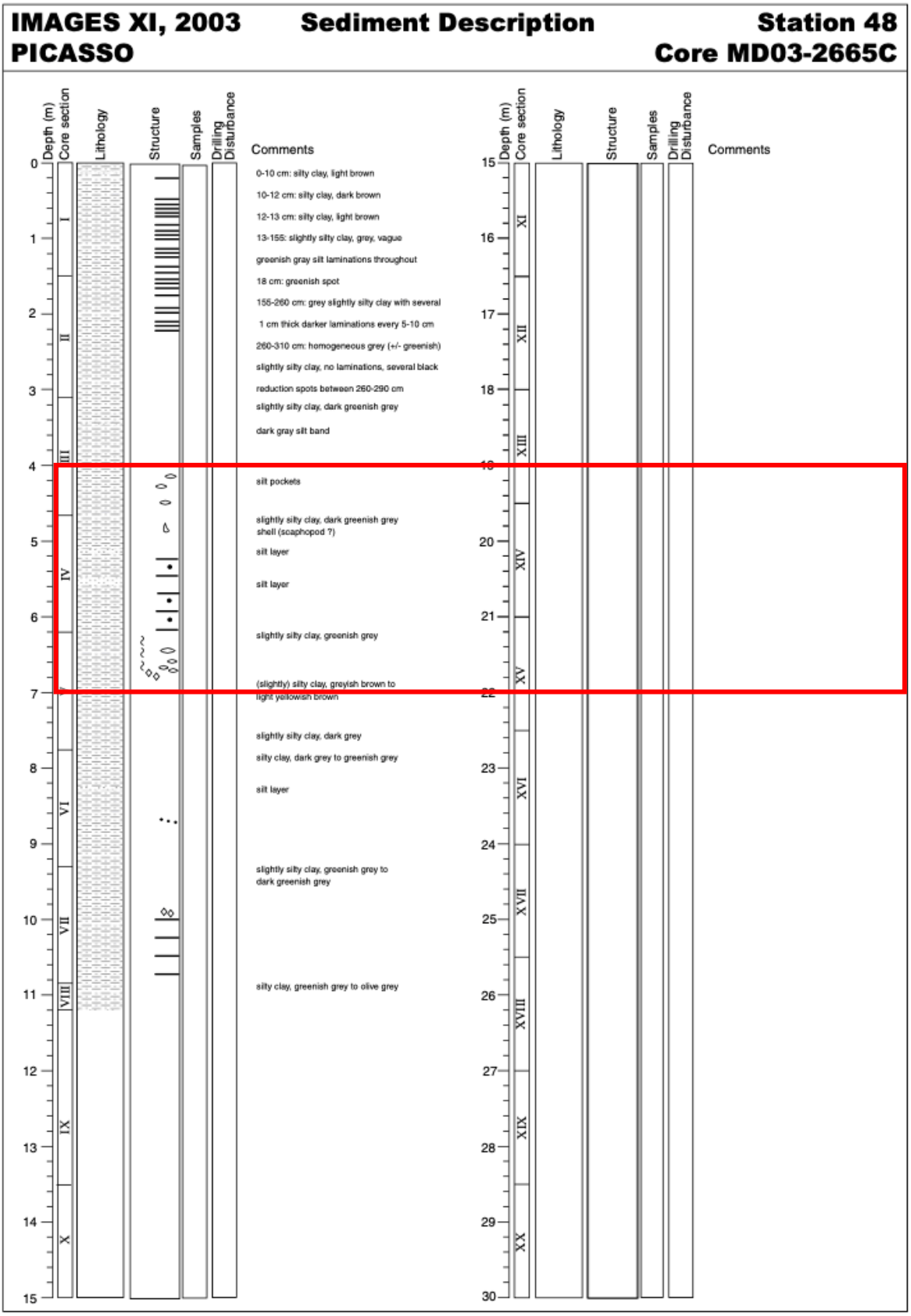

Figure 4.1: Log sheet for CASQ Core MD03-2665 with the study interval (400-700 cm) marked by a red box (Shipboard Scientific Party, 2003).

remove any particles. A syringe was used to remove the methanol from the samples before they were placed in a drying cabinet to dry. When the samples were dry, they were placed in reaction glasses were three drops of phosphoric acid (H_3PO_4) were added to create a reaction using an automated Kiel device preparation line. The stable isotope analyses were measured on a Finnigan MAT 253 mass spectrometer in the Facility for advanced isotopic research and monitoring of weather, climate, and biogeochemical cycling (FARLAB) at the Department of Earth Science and the Bjerknes Centre for Climate Research, University of Bergen. An average of three values for each sample was added in the dataset were this was possible (Appendix B). The samples were measured parallel with the standard Carrera Marble (CM03). The standards of the MAT 253 system have a long-term analytical precision (1σ) over several months for $\delta^{18}O$ and $\delta^{13}C$ of 0.1‰ and 0.04‰, respectively. The measured isotope values were calibrated to Vienna Pee Dee Belemnite (VPDB) using NBS-19 (Kleiven et al., 2008, Suppl.). NBS (National Bureau of Standards) is a global standard used to measure isotope values against.

4.2.3 Planktic foraminiferal assemblages and lithic counts

Planktic foraminiferal assemblages and lithic grains were counted every 4 cm spanning the 400–700 cm core interval. For planktic foraminiferal assemblages, samples were dry sieved at 150 μm and split into equal halves using a microsplitter, until approximately 250–300 planktic foraminifera were left to count. If unsplitted samples contained <250 planktic foraminifera, the next sample within 1–2 cm of the original sample that contained >250 was counted. For some samples, the number of planktic foraminifera was not sufficient, even samples 1–2 cm before and after, and in these cases, the whole sample was counted. The number of planktic foraminifera counted ranged from 247 to 649. Four samples contained less than 100 total number of planktic foraminifera: 500 cm (n=62), 503 cm (n=50), 512 cm (n=148) and 541 cm (n=78). The species *Neogloboquadrina pachyderma*, *Neogloboquadrina incompta*, *Turborotalita quinqueloba*, *Globigerina bulloides*, *Globigerinita glutinata* and *Globorotalia inflata* were most abundant in the samples. *Orbulina universa* were also found in three of the samples (Appendix C). Relative abundances of each species (in total planktic foraminifera) are calculated and reported in percent (%) form. The coiling ratio of *N. pachyderma* (i.e., the percentage of *N. pachyderma* in total *N. pachyderma* + *N. incompta*) is also calculated and used as a sea surface temperature proxy. Lithic grains (ice-rafted debris (IRD)) are also counted

using the >150 μm fraction. The number of IRD grains counted ranged from 0 to 1132. Results are expressed as the percentages (%) of IRD relative to total entities (i.e., planktic + benthic foraminifera) in each sample.

Identification and counting of the left coiling *N. pachyderma* and the right coiling *N. incompta* were done following Darling et al. (2006) (Figure 4.2). In samples that contained >97% left coiling specimens and <3% right coiling specimens, the right coiling specimens (aberrant forms) were counted as *N. pachyderma*. In samples that contained 3–97% right coiling specimens, the right coiling specimens were counted as *N. incompta*. No samples contained >97% right coiling specimens.

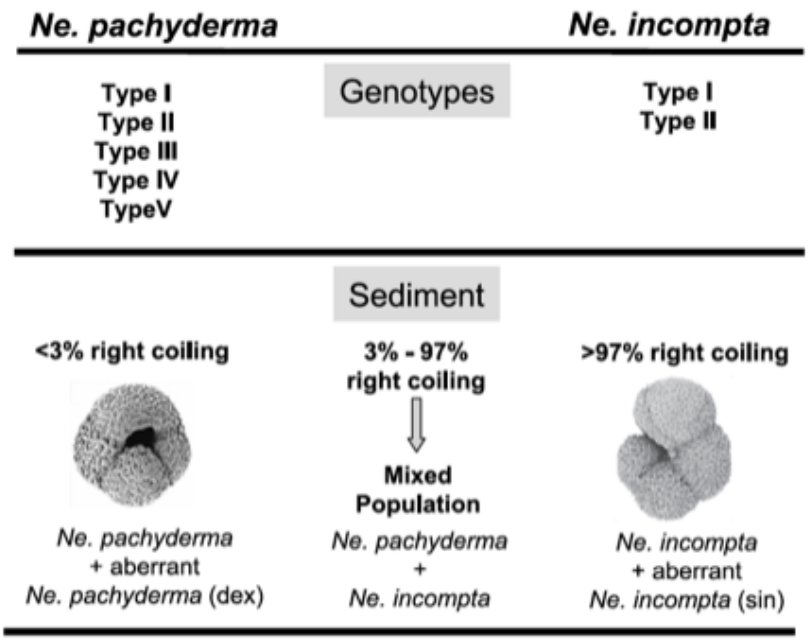

Figure 4.2: Classification of *Neogloboquadrina* in sediment samples from high latitudes. In sediment samples containing <3% right coiling specimens, all right coiled specimens should be identified as *N. pachyderma*. In sediment samples containing 3–97% right coiling specimens, the right coiled specimens should be identified as *N. incompta* and the left coiled specimens should be identified as *N. pachyderma*. In sediment samples containing >97% right coiling specimens, the right coiled specimens should be identified as *N. incompta*. From Darling et al. (2006).

4.3 Climate proxies

In studies that reconstruct past natural climate variability, scientists make use of proxy data. Something that represents something else indirectly is called a proxy. Proxies are recorded chemical and physical characteristics that stand in for direct temperature measurements. In paleoclimatology, scientists collect and use proxy data from natural recorders such as ice cores, corals, tree rings, marine and lake sediments. By analyzing records from these climate archives, we can extend our understanding of natural climate variability beyond the instrumental record that only robustly goes back to the 1880s (see https://www.metoffice.gov.uk/hadobs/hadcet/). Three of the proxies for climate reconstruction used in this study are stable isotope analysis, planktic foraminiferal assemblages and ice-rafted debris counts. These different proxies can tell a lot about how the climate has been in the past and are widely used for reconstructing surface ocean properties (temperature and salinity) and periods of ice-rafting. Below is a theoretical background about these proxies as well as some information on foraminifera and the planktic species important for determining climate variability in subpolar-polar regions.

4.3.1 Stable oxygen isotopes

In climate studies, isotope composition in climate archives serves as a measure for different properties. By measuring the ratio of stable isotopes in calcareous fossils it is possible to estimate how ocean circulation, nutrients, salinity and temperature has varied in the oceans (Lowe & Walker, 2015, p. 166). Since the first discovery of isotopes in the early 1900s (Boltwood, 1906) there has been many attempts to reconstruct past climate behavior (relevant examples from the study region are e.g., Kleiven et al. (2008); Knutz et al. (2011); Galaasen et al. (2014); Galaasen et al. (2020)).

The stable oxygen isotopes ^{16}O and ^{18}O have been essential in paleoenvironmental studies since Urey (1947) demonstrated that it is possible to derive ocean temperature from analysis of the ratio between these two. The ratio of these isotopes is measured in parts per mill (‰) relative to a standard (δ=0) (Equation 4.1). The standards are based on material the International Atomic Energy Agency are monitoring in Vienna (Lowe & Walker, 2015, p. 167).

$$\delta^{18}O = 1000\, x\, \frac{^{18}O/^{16}O\ sample - \ ^{18}O/^{16}O\ standard}{^{18}O/^{16}O\ standard}$$

Equation 4.1 (Lowe & Walker, 2015)

Epstein et al. (1953) calculated an equation for temperature derived from the δ value (Equation 4.2) by analyzing shells collected from sea water and shells in controlled tanks. *t* is temperature in ºC and δ is the difference between the ^{18}O in the sample and the reference gas.

$$t = 16.5 - 4.3\delta + 0.14\delta^2$$

Equation 4.2 (Epstein et al., 1953)

^{16}O is the most common oxygen isotope which contributes to 99.76 % of the naturally occurring oxygen, while the heavier ^{18}O isotope only contributes to 0.20 % of the total oxygen. A third oxygen isotope, not fundamental in environmental science, is ^{17}O, which contributes with the last 0.04 % of the oxygen (Cronin, 2010, p. 40). The lighter isotope (^{16}O) is favored in water vapor and will gather in clouds and later precipitate as rain or snow. If precipitation consolidates as ice in glaciers the ocean will be depleted of the lighter isotope as less addition of ^{16}O to the ocean occurs. The ocean is then enriched in the heavier (^{18}O) isotope and the $\delta^{18}O$ signal in the ocean increases (Bender, 2013, p. 31).

4.3.2 Ice-rafted debris

Ice-rafted debris (IRD) is a collective term for sediment transported by floating ice and deposited on the sea floor as the ice melt (Hemming, 2004) (Figure 4.3). IRD is usually present at a 1–3 m layer in the basal ice and is deposited during the first 10s to 100s km from the source (Dowdeswell, 1986; Andrews, 2000). IRD largely stems from calving ice and contains debris from basal erosion and processes transporting sediment onto the glacial surface including rockfall and avalanches (Dowdeswell, 1986). The minerology of IRD is largely dependent on the source material on land from which the glaciers have eroded and transported sediment in the basal ice. The presence of IRD in marine sediments is indicative of sediment-laden icebergs

stemming from calving glaciers. Previous studies have found distinct IRD peaks during the LGM, the deglaciation and Heinrich events (e.g., Ruddiman, 1977; Bond et al., 1992; Rørvik et al., 2010).

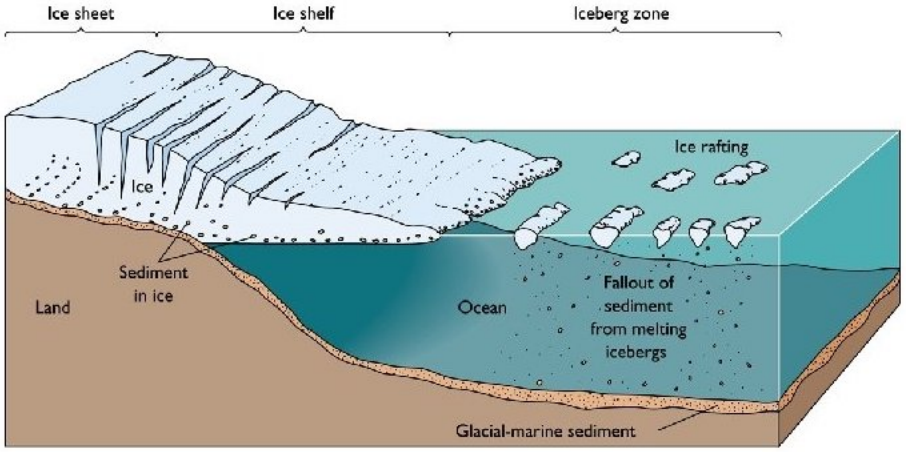

Figure 4.3: Schematic showing the process of ice-rafted debris deposition. Modified from Pinet (2016).

Heinrich events are periods of large outbursts of icebergs from glaciers that are transported through the North Atlantic and rapidly deposit IRD (Bond et al., 1992). These events deposit Heinrich layers, named after Heinrich (1988) who found six distinct layers in cores from the North Atlantic spanning the last glacial period, starting in last deglacial at 16 000 yr B.P until the Marine Isotope Stage (MIS) 5/4 boundary (~80 000 yr B.P.). Common for these layers are a low foraminiferal content largely represented by *N. pachyderma* and a high content of detrital carbonate (20–25%). The origin of Heinrich layers have been debated and the most accepted hypothesis remains the ice shelf buildup/collapse model of MacAyeal (1993) (e.g., Broecker et al., 1992; Bond & Lotti, 1995; Hemming, 2004). This hypothesis involves periods of large discharge of icebergs into the ocean from marine terminating glaciers, mainly from the Laurentide Ice Sheet into the Labrador Sea, that are transported south before turning northeastward with the North Atlantic Current following the boundary of the subpolar gyre. When the icebergs reach latitudes between 43ºN and 50ºN in the North Atlantic they melt and deposit IRD in a "belt" (Ruddiman, 1977; Bond et al., 1992; Broecker et al., 1992). Cores from these regions contain distinct Heinrich layers with high content of detrital carbonate. The layers have been identified in other parts of the North Atlantic, however, identification of all six layers have proven to be difficult outside of the IRD belt as some layers lack the large percentage of detrital carbonate associated with Heinrich layers (Bond et al., 1992).

Increased flux of IRD in the Northern Hemisphere is observed during two periods of the precessional cycle; when solar insolation is increased during winter and reduced during summer, and when insolation is increased during summer and reduced during winter. This is when the precessional angle is 90° and 270°, hence enhanced ice rafting occurs once every 11 000 ± 100 years (Heinrich, 1988).

4.4 Foraminifera

Foraminifera are marine single-celled protozoans (organisms) that live in the water column (planktic) or on the sea floor (benthic). They develop a calcareous skeleton (test) during their lifespan which range from under a year in tropical latitudes to two years or more in higher latitudes. The tests adopt the chemical signals from the water which later can be measured and used for paleoenvironmental reconstruction. The use of foraminifera in paleoclimate research, especially for stable isotope analyses and assemblage counts, are ideal as they are well preserved and make up a large portion of the ocean sediments, providing a close to continuous geological climate proxy records (Armstrong & Brasier, 2005, pp. 25, 142-144). In this study we only utilize the planktic foraminifera from the MD03-2665 samples and thus the next section will focus on the major planktic species selected in the Eirik Drift sediments.

4.4.1 Planktic foraminifera

Planktic foraminifera live in the water column where there is marine plankton (Armstrong & Brasier, 2005, p. 142). Most of the planktic foraminifera species are <100 μm in size and live only up to a month. The tests have numerous small holes resembling pores and their globular structure help increase buoyancy (Armstrong & Brasier, 2005, p. 157; Boudagher-Fadel, 2015, p. 12). Most species reproduce in the ocean surface layer monthly, and their reproductive cycle is believed to be closely linked to the lunar cycle (Bijma et al., 1990; Volkmann, 2000). When they die they sink down toward the bottom of the ocean where they generally become a part of a marine sediment layer representative of the temperature and density during their time of living (Armstrong & Brasier, 2005, p. 157). The distribution of planktic foraminifera is largely dependent on sea-surface temperature (SST), and Morey et al. (2005) concluded that the annual mean SST was the most dominating variable for planktic foraminiferal assemblages. Studies show that species survive in varying SSTs but have a preferred temperature where they are most abundant (Bijma et al., 1990; Žarić et al., 2005). The ecological distribution of planktic foraminiferal abundance presented in Kučera (2007) will be used to present planktic foraminiferal species (Figure 4.4).

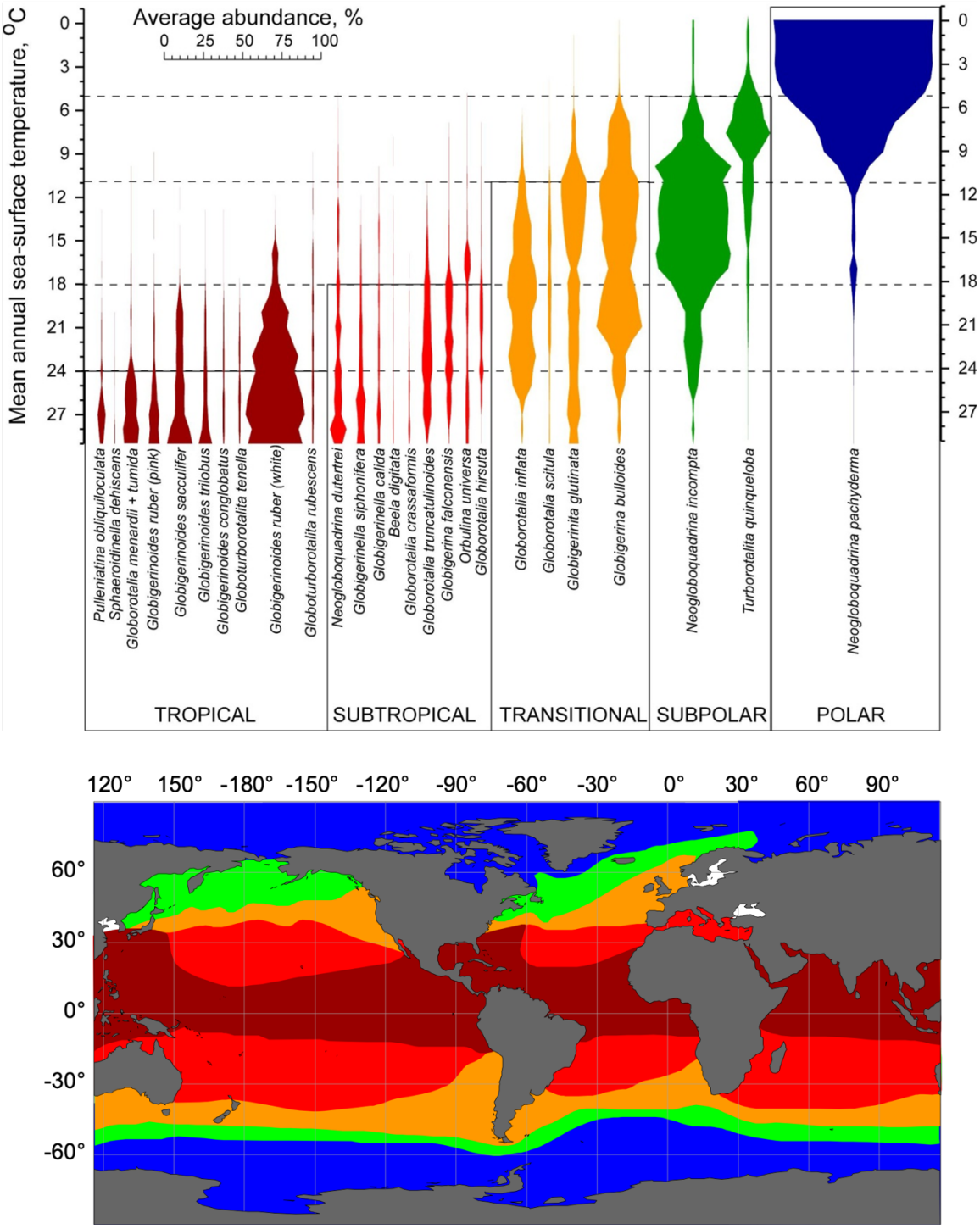

Figure 4.4: Abundance of foraminiferal species in different temperature zones. Map showing the five different foraminiferal provinces following temperature-gradients in the modern ocean. The abundance of foraminifera is greater in temperate regions compared to colder regions. The warmer (red colored) provinces have a large spectrum of species compared to the cold (blue) province where only one species, *N. pachyderma*, thrives. Modified from Kučera (2007).

4.4.1.1 Polar species

Neogloboquadrina pachyderma (Ehrenberg, 1861)

The only species thriving in the polar regions is *Neogloboquadrina pachyderma* (hereafter *N. pachyderma)* and thus its presence in sediment samples is a strong indicator for past polar conditions. The species dominates in cold, low saline waters between 0–9°C and are most abundant in temperatures below 4°C (Bé & Tolderlund, 1971; Sahoo et al., 2022). *N. pachyderma* avoids low-salinity waters though it has been observed to tolerate salinities up to 82‰ (Hemleben et al., 1989, p. 22). *N. pachyderma* inhabits depths of 5 to 50 m in ice-covered areas where the water is cold and fresh but dwells deeper, down to 100 m, in warmer, more saline water masses (Volkmann, 2000). The species is believed to calcify at all depths and secondary calcification occurs at depths between 50–200 m, primarily below the main pycnocline at 100–200 m depth (Kohfeld et al., 1996; Simstich et al., 2003). The highest abundance of *N. pachyderma* occurs below 100 m depth and reproduction primarily occurs at 100 m depth during full moon (Carstens et al., 1997; Volkmann, 2000). Reproduction peaks twice, one in spring and one in late summer (Tolderlund & Bé, 1971; Jonkers et al., 2010). *N. pachyderma* is the only species of foraminifera found living in sea ice but there is no indication that reproduction is occurring there (Spindler & Dieckmann, 1986).

The morphology of *N. pachyderma* is characterized by 4–4½ chambers in the last whorl exhibiting a quadrate test shape (Figure 4.5). The species is sinistral coiling (left), however, 2–3% within a population exhibit dextral coiling (right) specimens (Schiebel & Hemleben, 2017, p. 63).

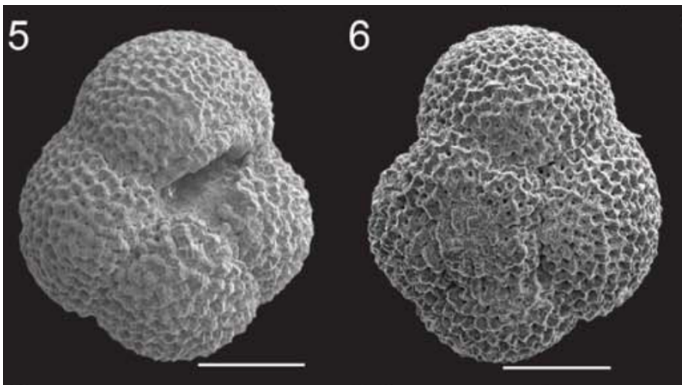

Figure 4.5: *Neogloboquadrina pachyderma*, 5: umbilical view, left-coling, 6: spiral view. Scale bars = 100 µm. Modified from Lam and Leckie (2020).

4.4.1.2 Subpolar species

Since subpolar species are dependent on light and food availability, small traces of subpolar foraminifera can be used to determine seasonally ice-free conditions (Kučera et al., 2005c).

Turborotalita quinqueloba (Natland, 1938)

Turborotalita quinqueloba (hereafter *T. quinqueloba*) is most abundant in subpolar surface waters where the water temperature is below 12°C, however it is also found in waters where temperature ranges from 1–21°C. The species is most common in the North Atlantic and the North Pacific, though it also has a high abundance in the Antarctic region at temperatures between 1–5°C (Bé & Tolderlund, 1971). The abundance of *T. quinqueloba* is reduced from higher to lower latitudes and it dwells in depths down to 200 m (Carstens et al., 1997; Schiebel & Hemleben, 2017, p. 50). *T. quinqueloba* appears to calcify at depths between 25–75 m and is not prone to secondary calcification (Simstich et al., 2003). It is usually abundant in open-water conditions but can also inhabit waters covered by sea-ice in smaller numbers and at a deeper depth (Carstens et al., 1997). The species reproduces monthly at a depth of 50–200 m, under the pycnocline, with a reproduction peak during late summer (Volkmann, 2000; Simstich et al., 2003; Jonkers et al., 2010). The morphology of *T. quinqueloba* is characterized by 4½–5½ rounded chambers where the final chamber has a lip almost covering the umbilicus in umbilical view (Figure 4.6). In some young specimens the characteristic lip is not present. The chambers increase in size towards the final whorl and the umbilicus is narrow (Bé & Tolderlund, 1971; Pearson & Kučera, 2018, p. 390).

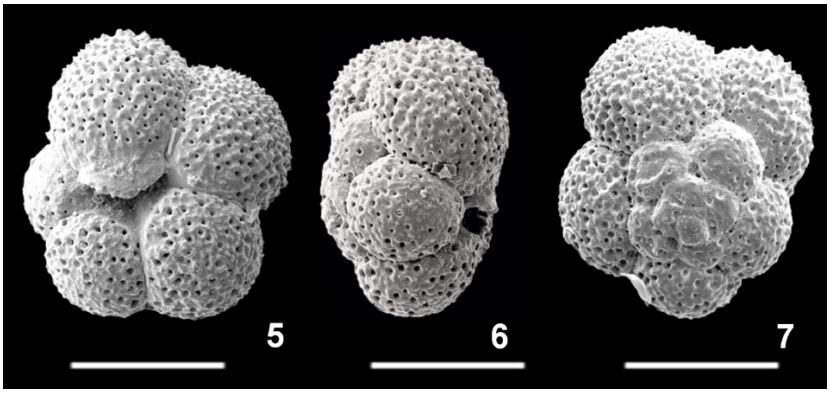

Figure 4.6: *Turborotalita quinqueloba*, **5**: umbilical view, lip covering umbilicus. **6**: side view, **7**: spiral view. Scale bars = 100 µm. Modified from Pearson and Kučera (2018).

T. quinqueloba is a known indicator species for changes in oceanic fronts. In the North Atlantic, a high abundance of this species combined with high abundances of the polar species *N. pachyderma* is a good indicator for the position of the Arctic Front. A smaller percentage of small specimens of *T. quinqueloba* can also be used as an indicator of the Polar Front (Johannessen et al., 1994).

Neogloboquadrina incompta (Cifelli, 1961)

Neogloboquadrina incompta (hereafter *N. incompta*) is a subpolar species residing in both hemispheres. It resides in temperate surface waters of 10–18°C (Bé & Tolderlund, 1971). The species have almost the same morphology as the polar species *N. pachyderma* but has a dextral coiling (right) direction as opposed to the sinistral (left) coiling direction of *N. pachyderma*. It has 4–5 chambers in the last whorl and exhibits, as its relative *N. pachyderma*, a quadrate shape (Figure 4.5). *N. incompta* produces less than 3% sinistral coiling specimens. Since both species inhabit <3% specimens of different coiling directions in a population they can be classified based on their coiling direction as either *N. pachyderma* (sinistral) or *N. incompta* (dextral) (Figure 4.7) without being bias (Schiebel & Hemleben, 2017, pp. 61-63).

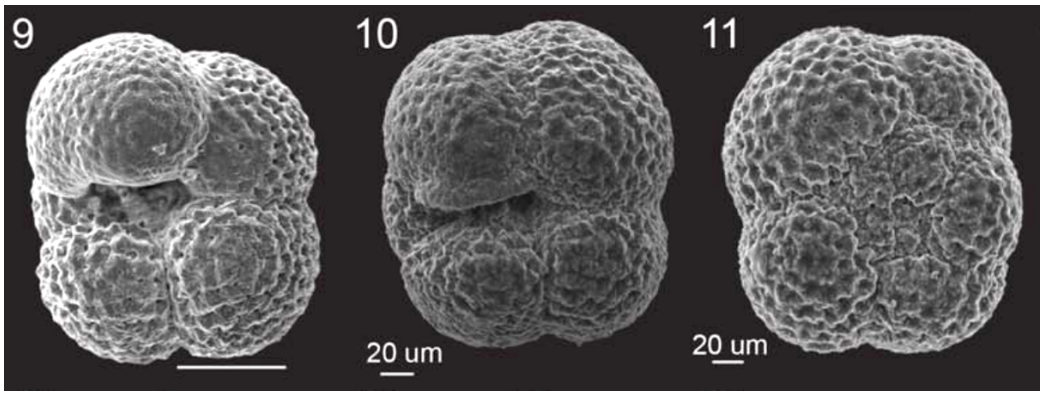

Figure 4.7: *Neogloboquadrina incompta*, **9-10**: umbilical view, **11**: spiral view. Scale bar: **9** = 100 µm. Modified from Lam and Leckie (2020).

N. pachyderma and *N. incompta* were previously thought to be the same species but have later been identified as separate species by genetic evidence (Darling et al., 2000, 2003, 2006). To avoid confusion between them, Darling et al. (2006) recommended to adopt *Neogloboquadrina*

incompta as the scientific name for the dextral coiling species. At ~9°C the abundance of *N. pachyderma* decreases and shifts to a dominance of *N. incompta* (Figure 4.8) (Žarić et al., 2005).

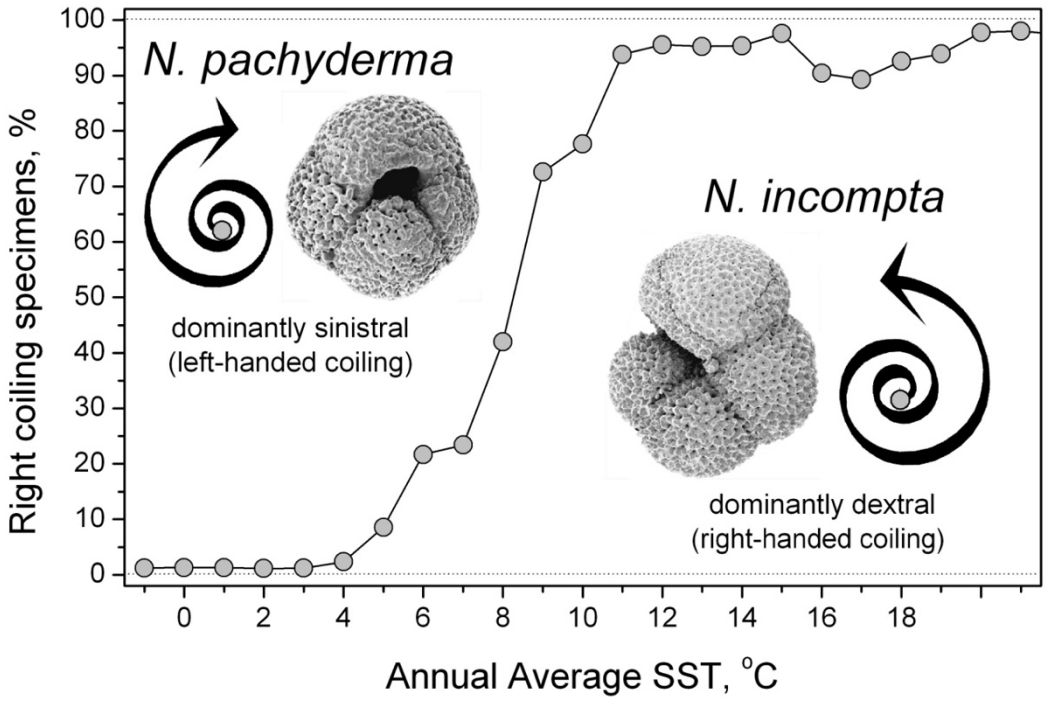

Figure 4.8: Percent abundance of *N. pachyderma* versus *N. incompta* plotted against annual average sea-surface temperature (°C). *N. pachyderma* dominates the low SST found in the polar regions, while *N. incompta* (right-coiling specimens) abundance increases rapidly from 6° - 8°C and dominates above 8°C. From Kučera (2007).

4.4.1.3 Transitional species

Transitional species thrive in a broad range of SSTs and are abundantly found in subpolar to subtropical waters (Kučera, 2007). Some transitional species seems to tolerate colder waters in the Southern Hemisphere than in the Northern Hemisphere. These include *Globorotalia inflata* and *Globigerinita glutinata* which are frequently observed in the subantarctic waters in the Southern Hemisphere but in subtropical to transitional waters in the Northern Hemisphere (Bé & Tolderlund, 1971). The transition between subpolar and transitional waters occurs at 18°C (Kučera, 2007). The most common transitional species found in MD03-2665 are *Globigerina bulloides*, *Globigerinita glutinata*, and *Globorotalia inflata*.

Globigerina bulloides (d'Orbigny, 1826)

Globigerina bulloides (hereafter *G. bulloides*) is a surface-dwelling species living in open water. This species is abundant throughout the first 300 m of the water column but are thought to be mostly residing in the upper 60 m (Schiebel et al., 1997). It is found in temperatures from 0–27°C and a peak abundance occurs in temperatures between 3–19°C (Bé & Tolderlund, 1971). The species is known to be an indicator of upwelling regions (Thiede, 1975; Kroon & Ganssen, 1989) and is abundant in subpolar to transitional waters (Tolderlund & Bé, 1971). Since the species inhabit both subpolar and tropical regions, it is suggested that food availability is the primary source of abundance rather than temperature (Reynolds & Thunell, 1985). The morphology of *G. bulloides* is characterized by four rounded chambers increasing in size (Figure 4.9). The aperture mostly faces forward with no significant incline to either the left or right side and is wide and open (Schiebel & Hemleben, 2017, p. 20).

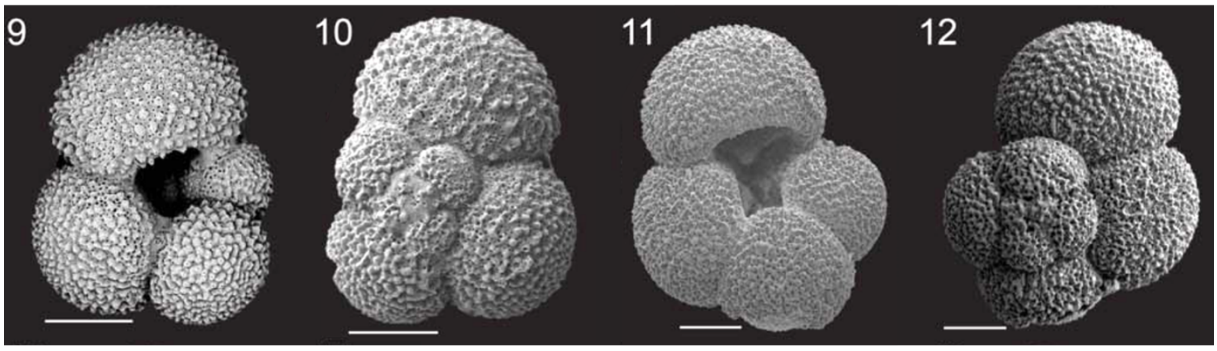

Figure 4.9: *Globigerina bulloides*. **9**, **11**: umbilical view, **10**, **12**: spiral view. Scale bars = 100 µm. Modified from Pearson and Kučera (2018).

Globigerinita glutinata (Egger, 1893)

Globigerinita glutinata (hereafter *G. glutinata*) is a surface-dwelling species found in subpolar waters to more temperate waters. It is found in temperatures ranging from 3–30°C and peaks between 24° and 27°C. The species has a relatively low abundance compared to other species and usually contributes to less than 5% of the total planktic foraminiferal assemblage. *G. glutinata* is equally abundant in the upper 10 m of the surface waters as it is down to 300 m depth (Bé & Tolderlund, 1971). The calcification depth is suggested to not be deeper than 130–150 m and thus happen within the surface mixed layer (Lončarić et al., 2006). The morphological features of *G. glutinata* is four rounded chambers with or without bulla covering the umbilicus. Bulla primarily occurs in adult specimens. The final chamber can sometimes be compressed (Figure 4.10) (Schiebel & Hemleben, 2017, p. 87).

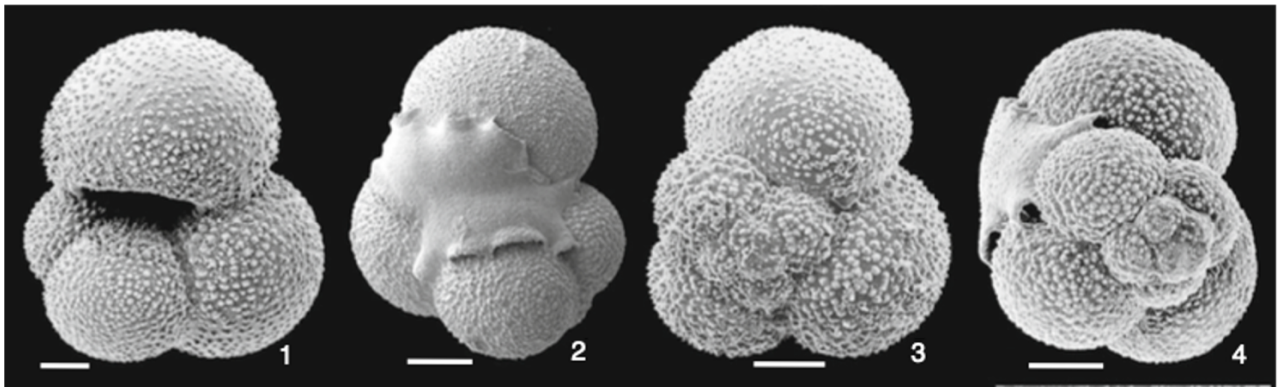

Figure 4.10: *Globigerinita glutinata*. 1: umbilical view, 2 umbilical view with bulla, 3: spiral view 4: lateral view with bulla. Scale bars = 50 µm. Modified from Schiebel and Hemleben (2017).

Globorotalia inflata (d'Orbigny, 1839)

Globorotalia inflata (hereafter *G. inflata*) is a deep-dwelling planktic foraminifera residing in surface waters down to 300 m depth. It lives in water temperatures between 1–27°C and thrives in temperatures between 13–19°C (Bé & Tolderlund, 1971). It is the only species that is native to the transitional waters in both the Northern and Southern Hemispheres and is therefore a good indicator of these waters (Tolderlund & Bé, 1971). Reproduction of *G. inflata* occurs during late spring and early summer (Chapman, 2010). Calcification occurs at 300 m depth

during summer and down to 400 m in winter where it stops below this depth (Lončarić et al., 2006). The species exhibit 3–4 chambers with a convex umbilicus and specimens are typically left coiled (Figure 4.11) (Schiebel & Hemleben, 2017, p. 20).

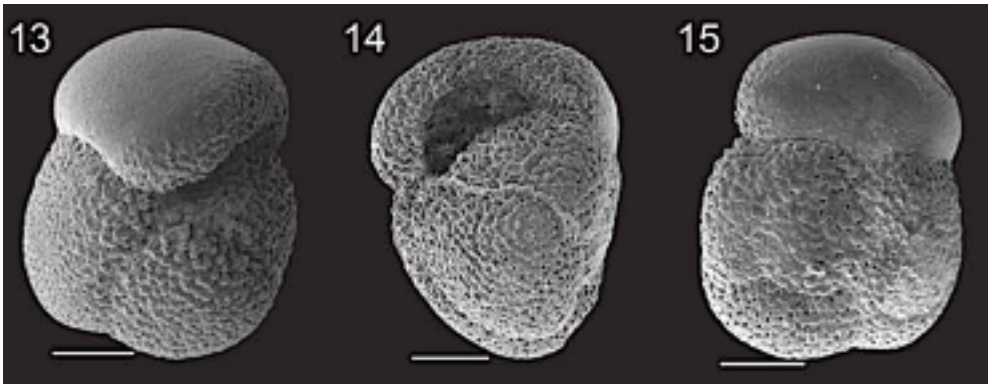

Figure 4.11: *Globorotalia inflata*, **13**: umbilical view, **14**: lateral view, **15**: spiral view. Scale bars = 100 µm. Modified from Pearson and Kučera (2018).

5 Chronology

Establishing accurate age-constraints are critically important in studies that reconstruct past climate. To know exactly when past climatic events occurred, if they occur synchronously, lead or lag is vital to better understand how the climate system works and determine the rate of change. Therefore, an age model was established for Core MD03-2665 (0–700 cm) based on dating of foraminiferal shells using Accelerator Mass Spectrometry (AMS) ^{14}C.

5.1 AMS ^{14}C dating

Accelerator Mass Spectrometry (AMS) dating measures the amount of ^{14}C atoms left in a material. This is accomplished through intensity measurements of ion beams using a mass spectrometer (Linick et al., 1989). There are three natural occurring isotopes of carbon; ^{12}C, ^{13}C and ^{14}C. The first two are stable isotopes that contributes to 98.9% and 1.1% of natural carbon, respectively. The third, ^{14}C, is unstable and exists as only 10^{-10}% (Lowe & Walker, 2015, p. 276). Despite its low content in carbon-bearing materials it is important in establishing the age of a material (Hajdas, 2008). ^{14}C has a half-life of 5730 ± 40 years (Godwin, 1962) which makes it eligible for dating back to approximately 45 000 years (Walker, 2005, p. 19).

^{14}C is produced by nuclear reaction on a nitrogen isotope (^{14}N) in the atmosphere. The carbon isotope attaches to molecules of CO_2 and becomes a part of the carbon cycle. All living organisms takes up carbon while still alive and after death the decay of ^{14}C begins (Linick et al., 1989). Since the atmospheric content of ^{14}C is well known for the last 13 900 yr cal. BP, a calibration curve spanning the last 55 000 yr cal. BP has been constructed (Reimer et al., 2020), making it possible to convert the AMS ^{14}C dates to calendar years.

In ^{14}C dating, an assumption is made that all living organisms have a uniform uptake of carbon globally. This is relatively true for the terrestrial organisms, with some correction for carbon fractionation through the food chain, whose uptake of carbon stems from the well-mixed atmosphere. However, for marine organisms the carbon uptake is not the same as the ocean is depleted in carbon compared to the atmosphere. This is due to the mixing of carbon from the atmosphere to the ocean which occurs more slowly than gas exchange on land (Ascough et al.,

2005). The surface layer of the ocean (upper 75 m) is well-mixed; however, the deep ocean is strongly depleted in ^{14}C as it moves slowly compared to the mixed layer. As the ocean is depleted in ^{14}C compared to the atmosphere it is necessary to correct ^{14}C ages for this effect, termed "reservoir effect". In the mixed layer between ~40–50º north and south of the equator, the global reservoir effect is calculated to be approximately 400 years while in the deep ocean this effect is more than 1 000 years (Mangerud, 1972; Stuiver et al., 1986). In higher latitudes the reservoir effect is greater because of upwelling of deep water depleted in ^{14}C (Bard et al., 1994). However, there are local variations due to differences in oceanic and climatic conditions. This also needs to be corrected for and is achieved by applying a local variation value, ΔR, which can be both positive and negative (Ascough et al., 2005). Positive ΔR values are applied in areas where deep water containing old carbon upwells and mixes with the surface layer depleting the layer of carbon. Negative ΔR values are applied in areas where there is significant inflow of water masses more in equilibrium with the atmosphere enriching the water with carbon (Ascough et al., 2004). A ΔR value can be retrieved from CALIB (http://calib.org/).

5.2 Age model

The age model for MD03-2665 was constructed (Figure 5.1) by calibrating AMS ^{14}C dates from the core using Bacon v2.3 (Blaauw & Christen, 2011) and the latest Marine20 calibration curve (Heaton et al., 2020). The age model was then fine-tuned based on the comparison to the North Greenland Ice Core Project (NGRIP) ice core (NGRIP members, 2004) (Figure 5.2). Bacon is a software using Bayesian statistics to generate an age model by reconstructing accumulation histories for deposits. This is done by combining the AMS ^{14}C dates from a core with other dates, and prior assumptions on the accumulation rate and the variability through time is considered (Blaauw & Christen, 2013). The Marine20 calibration dataset is an international marine calibration curve for non-polar regions with globally averaged radiocarbon ages from 0–55 kyr cal BP (Heaton et al., 2020).

AMS dating was performed at Leibniz Labor für Altersbestimmung und Isotopenforschung (KIA), Kiel, Germany, and at Laboratoire des Sciences du Climat et de l'Environnement (GifA), Gif-sur-Yvette, France. When measured, all the samples gave sufficient material of

approximately 1 mg carbon as well as producing sufficient ion beam yielding reliable results within 1σ (σ = standard deviation).

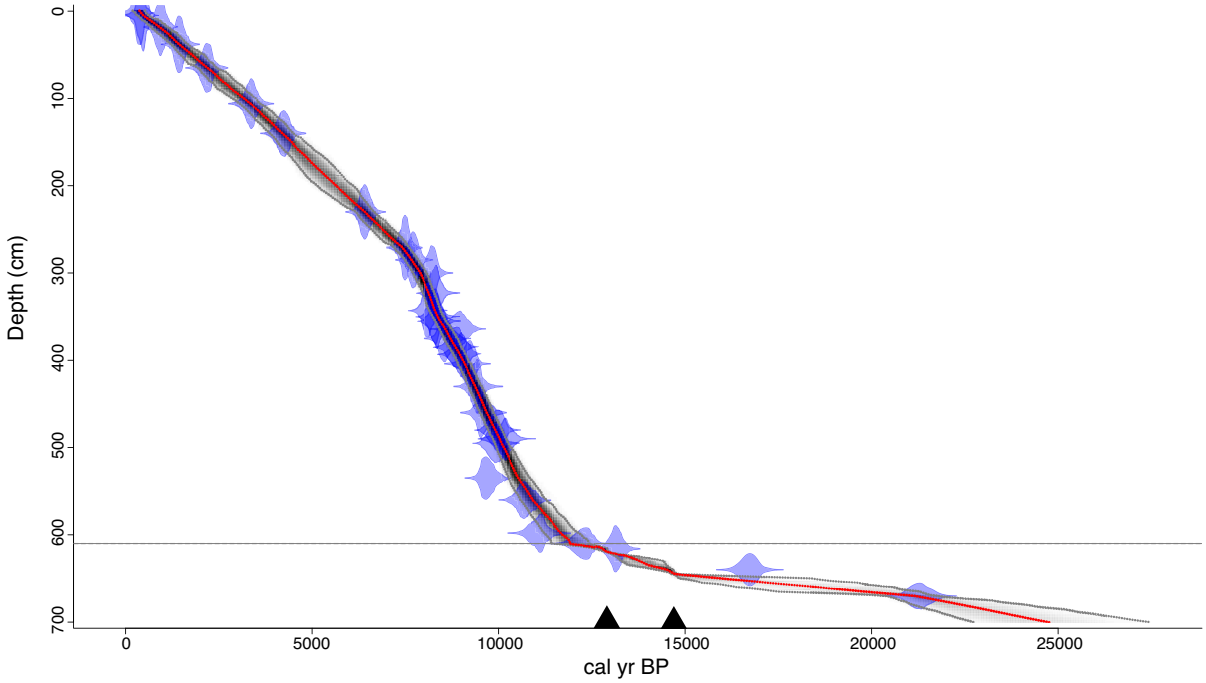

Figure 5.1: Age model for Core MD03-2665 from the Eirik Drift. The horizontal line indicates where a new mean accumulation rate has been selected. The two black triangles indicate the tie points chosen for correlation with NGRIP ice core from Rasmussen et al. (2014).

A total of 32 dates and two tie points were used to generate the age model. The two tie points were determined based on isotopic data from the MD03-2665 planktic $\delta^{18}O$ record. The tie points were placed at 620 cm and 644 cm depth, as the $\delta^{18}O$ variability at these intervals are assumed to be linked to the Younger Dryas (YD) and the Bølling-Allerød (B/A), respectively, based on the similarities in the $\delta^{18}O$ records for MD03-2665 and NGRIP. The correlation of $\delta^{18}O$ of MD03-2665 to the $\delta^{18}O$ of the NGRIP ice core was performed as it is a well-known, high-resolution, and undisturbed source in terms of age on climate fluctuations (NGRIP members, 2004) which is collected from Greenland in the vicinity of the core location on the Eirik Sediment Drift. The ages of the tie points (i.e., the start of the YD (GS-1) and the B/A (GI-1e)) were acquired from Rasmussen et al. (2014) and are available in Appendix D together with the AMS ^{14}C dates.

A mean accumulation rate of 20 yr/cm was set for depths above 610 cm, and 120 yr/cm was selected for depths below 610 cm corresponding to sedimentation rates of ~50 cm/kyr and ~8.3 cm/kyr, respectively. The average Holocene sedimentation rates at the Eirik Drift varies between 40–90 cm/kyr (Kleiven et al., 2008) while sedimentation rates for glacial periods are considerably lower, e.g., ~6.5 cm/kyr in MIS 5d (Irvali et al., 2012), making the selected sedimentation rates appropriate. The ΔR value for the depths which yields uncorrected ^{14}C ages below 10 000 years was set to –24 ± 76 years (Appendix E). The ΔR value for the Holocene interval is obtained from calib.org and is the weighted mean of the ten nearest points to the Eirik Drift core location. For the ages above 10 000 years a ΔR value of 800 ± 100 years was selected, setting this new ΔR at 598 cm depth and below. The change of ΔR is set as 800 ± 100 years roughly corresponding to the Holocene/deglacial boundary at 10 000 ^{14}C yr (Keigwin et al., 1991).

In high latitudes, marine reservoir ages can be highly variable, especially during the glacial periods, due to increased variability in ocean ventilation and air-sea gas exchanges (Butzin et al., 2005, 2020; Heaton et al., 2020). The new Marine20 calibration curve accounts for more realistic marine reservoir age estimates for the last glacial interval compared to the constant reservoir age (~405 ^{14}C yr) used in the previous Marine13 (Heaton et al., 2020). However, calibrating our dates using the Marine20 curve and using the same ΔR value (-24 ± 76 years) through the Holocene and last deglacial has shown the need for further adjustments beyond the Holocene. This might be due to the limitation of Marine20 in high latitude regions (i.e., from 40ºS–40/50ºN) as acknowledged by Heaton et al. (2020). Therefore, different reservoir ages were tested and a reservoir age of ~1 400 years was applied (ΔR=800 ± 100 years) for the 598–700 cm interval, which is within the range for the last deglacial reservoir age estimates for the NE Atlantic (Skinner et al., 2019).

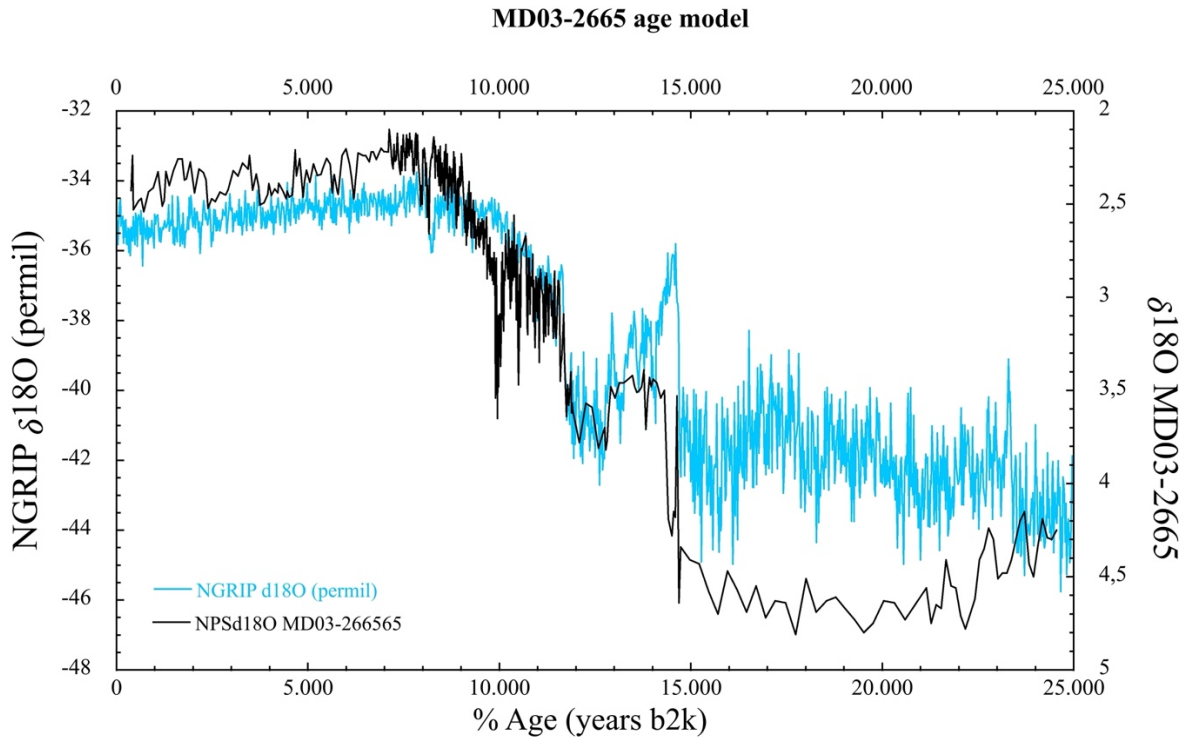

Figure 5.2: New age model for Core MD03-2665 from the Eirik Drift. $\delta^{18}O$ from MD03-2665 (black) are correlated to NGRIP $\delta^{18}O$ (blue) and plotted versus age. The age model fits well through the Holocene with less certainty through the deglaciation.

6 Results

In this chapter, the new results from the planktic foraminiferal assemblages and lithic counts are presented. Prior to the work in this master thesis project, stable isotopes on *N. pachyderma* were analyzed at almost every 1 cm throughout the core down to 700 cm with some exceptions where the number/weight of foraminifera shells were not sufficient (Table 6.1, Appendix B). The studied interval from Core MD03-2665 spans an interval from the LGM through the early Holocene (~25 000–9 000 yr BP) (Figure 6.1). The most abundant planktic foraminiferal species include *N. pachyderma*, *T. quinqueloba*, *N. incompta*, *G. inflata*, *G. glutinata* and *G. bulloides* and are presented as percentage (%) of total planktic foraminiferal assemblage. The coiling ratio of *N. pachyderma* (sinistral versus dextral, i.e., *N. incompta*) is calculated as the amount of *N. pachyderma* against *N. incompta*. The % of IRD is calculated as number of IRD grains against total entities (planktic + benthic foraminifera and IRD).

Table 6.1: Data produced in previous studies using the Eirik Drift core MD03-2665, spanning the last deglaciation and the Holocene. Data produced in this study is also included spanning the last deglaciation. [1]0–258 cm, [2]258–700 cm, [3]0–56 cm, [4]56–400 cm.

Proxy records from MD03-2665	**References**	**Sampling resolution**
N. pachyderma δ^{18}O (0–700 cm)	Kleiven et al. (2008) (0–460 cm) Kleiven (unpublished) (460–700 cm)	4 cm[1] 1 cm[2]
Planktic foraminiferal assemblage and ice-rafted debris counts (0–400 cm)	Irvali et al. (unpublished)	1 cm[3] 4 cm[4]
Planktic foraminiferal assemblage counts (400–700 cm)	This study	4 cm
Ice-rafted debris counts (400–700 cm)	This study	4 cm

6.1 Oxygen isotope analyses

Oxygen isotope ratios of planktic foraminifera represent changes in near-surface physical properties and provides information on sea surface temperature, salinity and the $\delta^{18}O$ of sea water in which the foraminifera calcify. In Figure 6.1, the $\delta^{18}O$ record of *N. pachyderma* spanning the study interval between 400–700 cm in Core MD03-2665 is plotted versus age (cal. yr BP). It is plotted versus age by using the age model described in Chapter 5. This is done in order to give insight on the temporal characteristics of observed changes in near-surface properties, their duration and rate. The *N. pachyderma* $\delta^{18}O$ record for the first 400 cm of the core is published in Kleiven et al. (2008) and are listed in Appendix B.

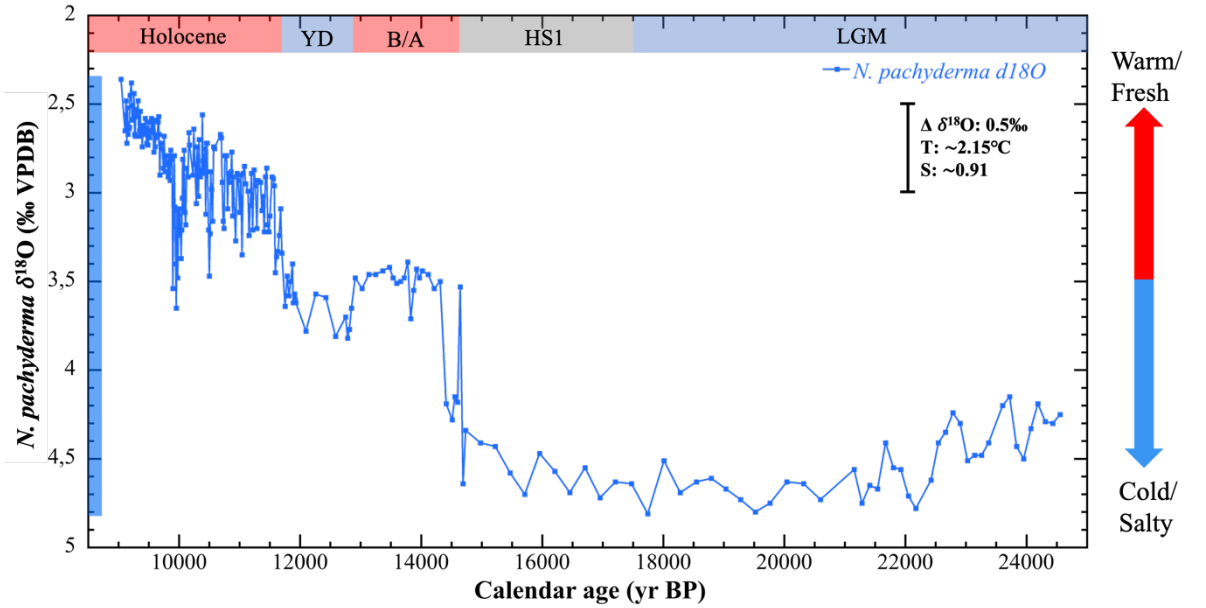

Figure 6.1: The *N. pachyderma* $\delta^{18}O$ record for core MD03-2665 from the Eirik Drift plotted versus age (8 500–25 000 yr BP corresponding to 400–700 cm in the core). The data points are presented by blue squares. The Holocene and the Bølling–Allerød (B/A) (warm periods) are marked by red horizontal bars. The Younger Dryas (YD) and the Last Glacial Maximum (LGM) (cold periods) are marked with blue horizontal bars. Heinrich Stadial 1 (HS1) is marked by a light grey horizontal bar.

The planktic $\delta^{18}O$ record exhibit a prolonged cold interval from ~25 000 to 16 000 yr BP with high and relatively stable $\delta^{18}O$ values varying between ~4.2–4.8‰. This interval spans the LGM interval of the core and the first part of HS1. The variability throughout this interval includes several millennial-scale oscillations that are superimposed on the long-term trends. These oscillations often exceed 0.5‰ and they are features comprised of several data points. A slight increase in $\delta^{18}O$ (cooling trend) is observed from ~25 000–22 000 yr BP, where the $\delta^{18}O$

values increase from ~4.2–4.4‰ and from ~22 000–20 000 yr BP with values as high as ~4.6–4.7‰ towards the peak of the LGM. These high values span the next ~4 000 years with $\delta^{18}O$ reaching its highest values at ~19 500 yr BP (~4.8‰). Following this, is a slight decrease (warming trend) from ~16 000–14 700 yr BP, towards the end of HS1, with $\delta^{18}O$ values fluctuating between ~4.6‰ and ~4.4‰. The onset of the B/A is very abrupt, occurring within a few cm's of core, with a rapid decrease to ~3.5‰ at ~14 700 yr BP. Thus, this warming was accomplished very rapidly, but lasted only ~45 years, before the $\delta^{18}O$ values very rapidly return to glacial values of ~4.2‰. Following this initial rapid temperature jump, the $\delta^{18}O$ values remain high for ~200 years until ~14 400 yr BP when a second rapid decrease to ~3.5‰ at ~14 300 yr BP occurs. Following this abrupt jump, the $\delta^{18}O$ signal remains relatively stable from ~14 300 yr BP to ~12 800 yr BP, across the B/A interval, with a mean value of ~3.5‰. The interval is interrupted by one short-term oscillation at ~13 800 yr BP with a rapid increase to ~3.7‰. After this, the $\delta^{18}O$ signal increases from ~3.5‰ to ~3.8‰, most likely corresponding to the Younger Dryas (YD) interval (12 800–11 700 yr BP). Following the end of this interval at ~11 700 yr BP, the $\delta^{18}O$ values gradually decreases to ~3.1‰ and further to ~2.9‰ at ~10 700 yr BP. Superimposed on this warming trend, is distinct sub-millennial oscillations. Following this is a gradual decrease (from ~2.9‰ to ~2.3‰) in planktic $\delta^{18}O$ towards the end of the study interval at ~9 000 yr BP. This trend is interrupted by an abrupt large deviation at ~10 000 yr BP. Both the onset and the end of this event is very rapid, with values increasing from ~2.8‰ to ~3.4‰ and back to ~2.8‰, the transition spanning just a few cm's of core.

6.1.1 Prominent temperature and salinity changes in the $\delta^{18}O$ record

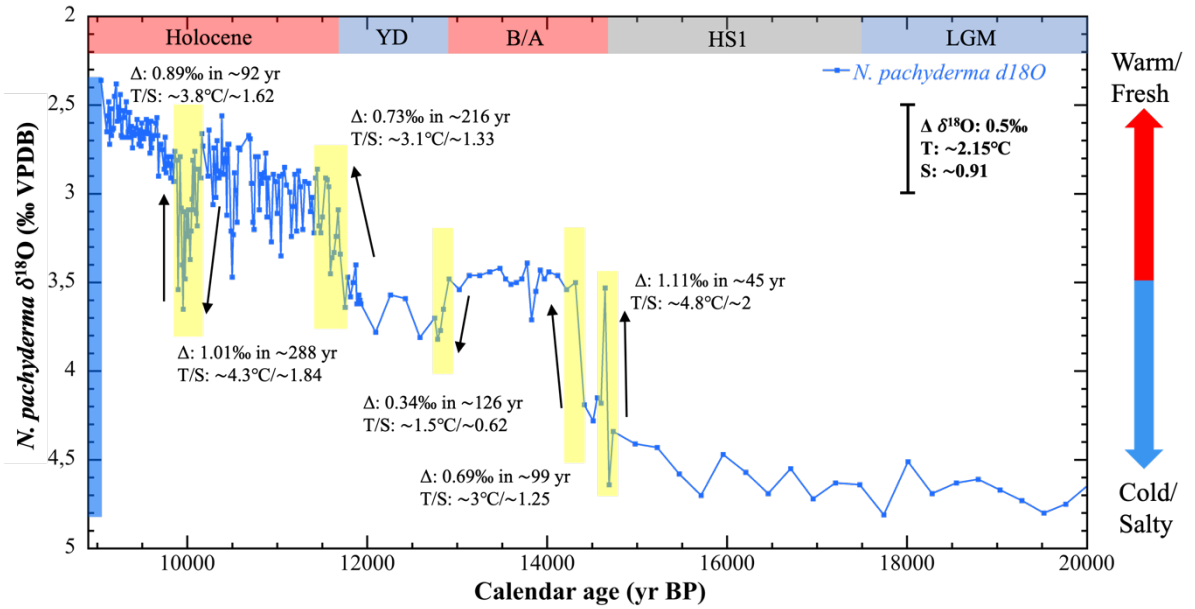

Figure 6.2: The *N. pachyderma* $\delta^{18}O$ record for MD03-2665 plotted versus age (yr BP), focused in on the 8 500–20 000 yr BP interval to emphasize the deglacial transition and variability at the Eirik Drift. The blue vertical bar indicates the total range of $\delta^{18}O$‰. The Holocene and B/A are marked by red horizontal bars indicating warmer periods, whereas the YD and LGM are marked by blue horizontal bars indicating colder periods. Heinrich Stadial 1 (HS1) is marked with a light grey horizontal bar. The red vertical arrow represents warm/fresh water, whereas the blue vertical arrow indicates cold/salty water. Temperature (T) and salinity (S) change corresponding to $\Delta\ \delta^{18}O = 0.5$‰ is presented by a black bar. Yellow highlighted intervals indicate periods of prominent change in the $\delta^{18}O$ record with the change of $\delta^{18}O$ and corresponding T/S indicated in the text below.

The most prominent and rapid changes in the *N. pachyderma* $\delta^{18}O$ record that spans the last deglaciation at the Eirik Drift site MD03-2665 are indicated with five yellow highlighted bars in Figure 6.2. The observed variability and trends in planktic foraminiferal $\delta^{18}O$ values are related to changes in the sea surface temperature and salinity. According to the paleotemperature equation (Equation 4.2; Epstein et al. (1953)) presented in Chapter 4, a 1‰ decrease in $\delta^{18}O$ corresponds to a 4.3ºC increase in temperature. Furthermore, following the modern $\delta^{18}O_{sw}$ – Salinity relationship in the region (Schmidt, 1999; Schmidt et al., 1999; Bigg & Rohling, 2000; Rutledal, 2017), a 1‰ decrease in $\delta^{18}O$ corresponds to a decrease in salinity of 1.81. However, it is important to note that the $\delta^{18}O_{sw}$ – Salinity relationship is not constant through time, and it is also affected by global ice volume changes – especially over the LGM and the last deglaciation. The calculated $\delta^{18}O$ values are based on the modern $\delta^{18}O$ – Salinity relationship of the North Atlantic seawater which is largely dominated by precipitation and evaporation. The $\delta^{18}O$ – Salinity relationship during the LGM and the last deglaciation was

largely dominated by freshwater by melting continental ice sheets which is depleted in $\delta^{18}O$ and could potentially yield higher $\delta^{18}O$ anomalies with a smaller salinity change. Therefore, the changes in salinity should be considered as maximum values as they could be overestimated.

The first prominent event, at ~14 700 yr BP, occurs over a period of ~45 years with an amplitude of ~1.11‰, representing an abrupt temperature increase of ~4.8ºC (or decrease in salinity of ~2). Following this is a rapid decrease in temperature that lasts until the second prominent millennial-scale oscillation is initiated at ~14 400 yr BP. The $\delta^{18}O$ values exhibit an amplitude of ~0.69‰, representing a rapid temperature increase in near-surface water of ~3ºC (or decrease in salinity of ~1.25) over a period of ~99 years. These two events can most likely be linked to the B/A interstadial. The third event is a rapid cooling trend that is initiated approximately at ~12 900 yr BP and lasts for ~126 years. The ~0.34‰ increase in $\delta^{18}O$ indicate a cooling of ~1.5 ºC (or an increase in salinity of ~0.62). Moving closer to the YD–Holocene transition, there is a fourth rapid temperature/salinity change at ~11 750 yr BP that is characterized by an increase in temperature of ~3.1ºC (or a salinity decrease of ~1.33). The last, notable perturbation in planktic $\delta^{18}O$ occurs in the early Holocene, exhibiting an abrupt cooling event (or increased salinity) centered at ~10 050 yr BP. $\delta^{18}O$ values increase sharply by ~1‰, from ~2.8‰ to ~3.8‰, suggesting a rapid cooling of ~4.3ºC (or salinity increase of 1.84). The event is initiated at ~10 240 yr BP and lasts ~288 years based on the proposed age model. This cooling is followed by a similar sharp recovery with $\delta^{18}O$ values decreasing to ~2.8‰ in ~92 years, starting at ~9 950 yr BP, suggesting a rapid warming of ~3.8ºC (or a decrease in salinity of ~1.62).

6.2 Planktic foraminiferal assemblages

The relative abundances of the most abundant planktic foraminiferal species are presented in this section.

6.2.1 Polar species

The polar species abundant in the core is *N. pachyderma*. This species is dominant in polar regions in both the Northern and Southern Hemisphere (Kučera, 2007).

6.2.1.1 Relative abundance of *N. pachyderma*

The relative abundance (%) of *N. pachyderma* is shown as a smoothed 3 point mean record and a non-smoothed record plotted versus age (yr BP) in Figure 6.3. To demonstrate how the relative abundance of species relates to the relative temperature change, the y-axis has been inverted.

In the non-smoothed record, the relative abundance of *N. pachyderma* varies between ~11% and 100%. The % *N. pachyderma* exhibits a relatively high and stable relative abundance close to ~100% between ~25 000 and ~17 500 yr BP. After this interval, there is a small and gradual decrease up to ~81% observed from ~17 500 yr BP to ~14 000 yr BP, most likely corresponding to the B/A warming. Following this, % *N. pachyderma* increases to almost 100% by ~13 500 yr BP and remains high throughout the YD interval (~95% at ~11 700 yr BP). Following the YD, from ~11 600 yr BP to ~11 400 yr BP the % *N. pachyderma* rapidly decreases to ~45%. From ~11 400–10 400 yr BP, there is a decrease of ~15% before a slight increase back to ~45% at ~10 300 yr BP. A decrease to ~11% is observed at ~10 200 yr BP. A rapid increase to ~65% at ~10 000 yr BP is followed by a second rapid decrease to ~30% at ~9 900 yr BP. From ~9 900 yr BP towards ~9 000 yr BP, the values vary between ~20–55%.

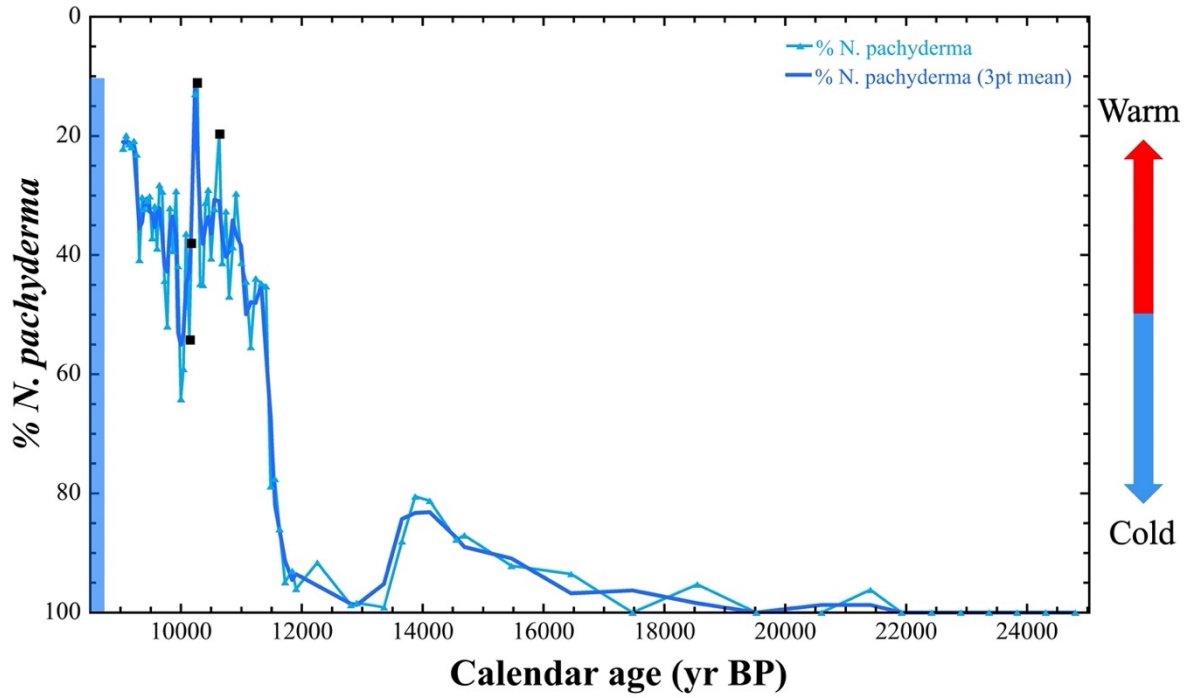

Figure 6.3: The relative abundance (%) of *N. pachyderma* at the Eirik Drift plotted against calendar age (yr BP). The % *N. pachyderma* is plotted as both a smoothed and a non-smoothed record. The light blue line depicts the non-smoothed record, and the blue line depicts the 3pt mean smoothed record. The black squares indicate samples where the planktic foraminiferal abundance was insufficient (<250). The blue vertical bar indicates total range of % *N. pachyderma*. Arrow indicates warmer (red) or colder (blue) temperatures.

6.2.2 Subpolar species

The subpolar species found to be abundant in the core is *T. quinqueloba* and *N. incompta*.

6.2.2.1 Relative abundance of *T. quinqueloba*

The relative abundance of *T. quinqueloba* is plotted as a smoothed 3 point mean record and a non-smoothed record plotted versus age (yr BP) in Figure 6.4.

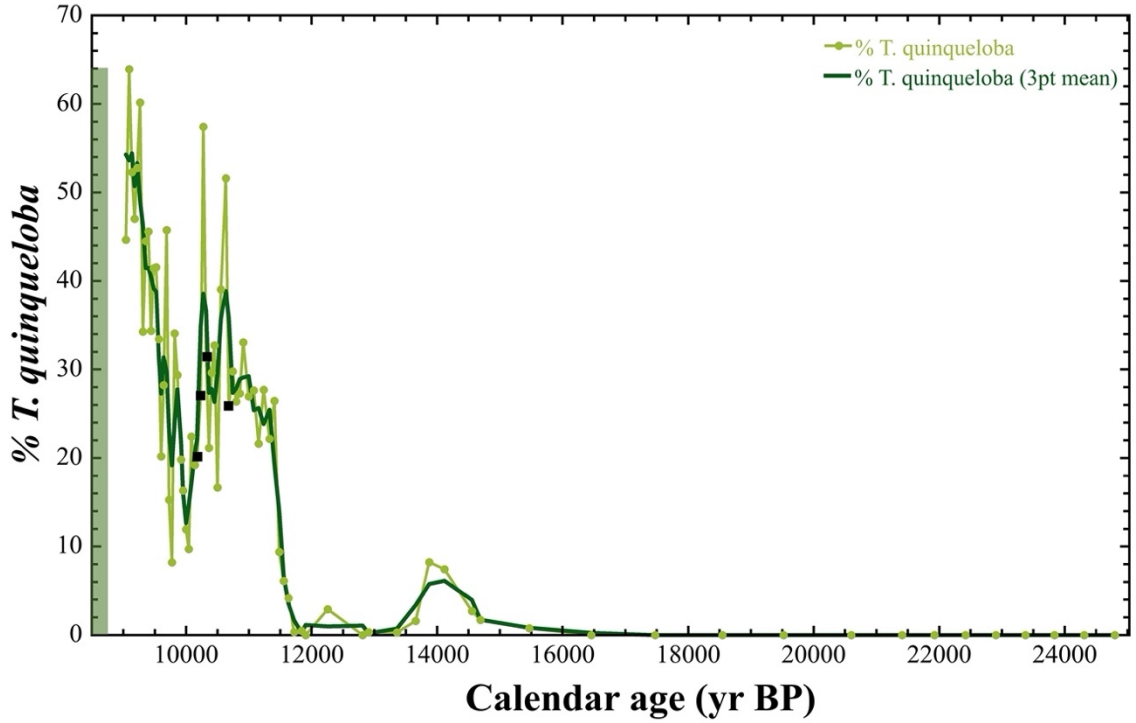

Figure 6.4: The relative abundance (%) of *T. quinqueloba* at the Eirik Drift plotted against calendar age (yr BP). The non-smoothed % *T. quinqueloba* record is indicated by the light green line, and the smoothed (3pt mean) record is indicated by the dark green line. The black squares indicate samples where the planktic foraminiferal abundance was insufficient (<250 planktic foraminifera). The total range of % *T. quinqueloba* is represented by a green vertical bar.

The % abundance of *T. quinqueloba* varies between ~0% and ~64% for the non-smoothed record. The highest relative abundance is observed at ~9 000 yr BP and the lowest between ~25 000 and ~15 000 yr BP. *T.quinqueloba* is absent during the coldest interval of the record, between ~25 000 and ~15 000 yr BP. An increase to ~8% followed by a decrease to 0% occurs between ~15 000 and ~13 000 yr BP, most likely marking the warming during the B/A interstadial. Near-zero percentages are observed over the YD, from ~13 000 to ~11 700 yr BP. A rapid increase to ~27% is observed at ~11 400 yr BP, followed by a more gradual increase to ~52% by ~10 600 yr BP. A short-lived rapid decrease to ~17% at ~10 500 yr BP is followed

by an equally rapid return to high abundances of ~57% by ~10 300 yr BP. A second rapid decrease with abundances as low as ~9% occurs at ~10 000 yr BP, followed by a relatively rapid and steady increase to ~64% by ~9 000 yr BP.

6.2.2.2 Relative abundance of *N. incompta*

The relative abundance of *N. incompta* is illustrated as a non-smoothed record and a smoothed (3pt mean) record plotted against age in Figure 6.5.

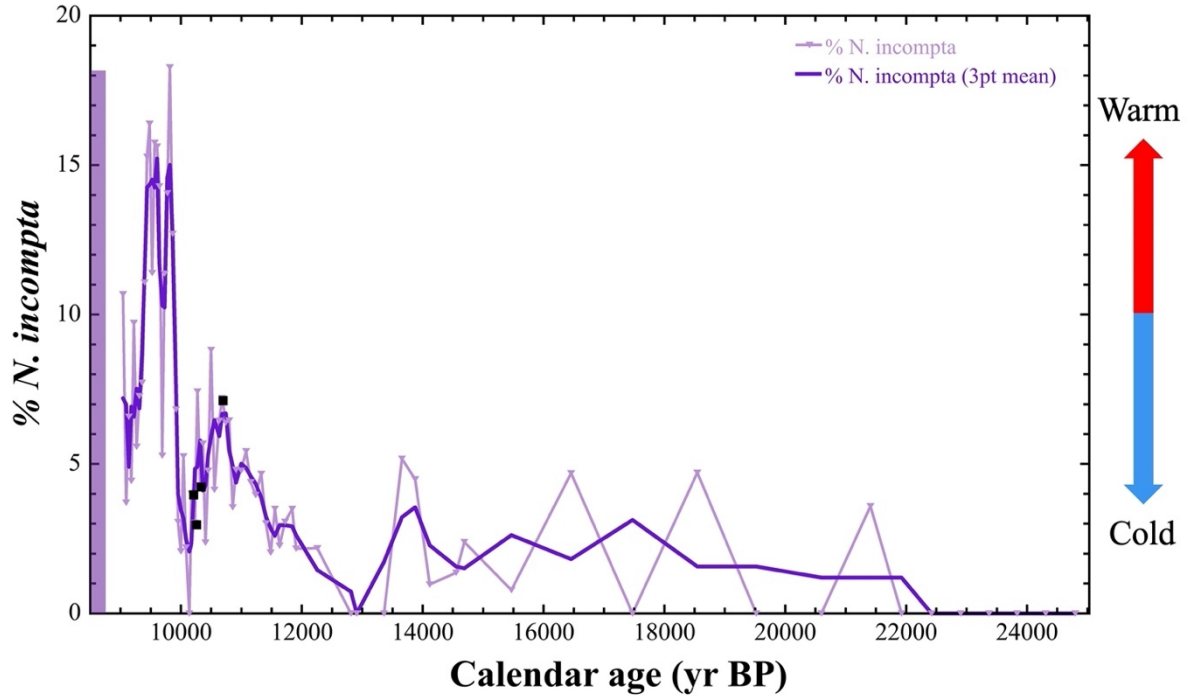

Figure 6.5: The relative abundance of *N. incompta* at the Eirik Drift plotted against calendar age (yr BP). The % *N. incompta* is plotted as both a non-smoothed (light purple) record and a 3pt mean smoothed (darker purple) record. The black squares indicate samples where the counted planktic foraminiferal abundance was less than 250. The purple vertical bar indicates the total range of % *N. incompta*. The red vertical arrow indicates warmer temperatures, whereas the blue vertical arrow indicates colder temperatures.

The range of the relative abundance of the non-smoothed *N. incompta* record is 0% at its lowest and ~18% at its highest. The % *N. incompta* is relatively stable at 0% from ~25 000–11 500 yr BP with only some minor peaks of ~4–5% centered at ~21 500, ~19 500, ~18 500 yr BP and one peak between ~14 000–13 500 yr BP. A slightly longer interval between ~11 500–10 000 yr BP exhibits values between ~3-8% superimposed on a steady increase in abundance to a maximum of ~8% at ~10 500 yr BP before a rapid decrease to 0% at ~10 000 yr BP. The most

notable feature in the *N. incompta* record is the rapid increase from 0% at ~10 000 yr BP to ~18% by ~9 800 yr BP and the subsequent rapid decrease. This interval is followed by abundances varying around 15% at ~ 9 400 yr BP, and thereafter values between ~5–10% from ~9 400 to ~9 000 yr BP.

6.2.3 Transitional species

The most abundant transitional species found at the Eirik Drift in Core MD03-2665 are *G. bulloides*, *G. glutinata* and *G. inflata*.

6.2.3.1 Relative abundance of *G. bulloides*

The relative abundance of *G. bulloides* is plotted against age with smoothed and non-smoothed records (Figure 6.6).

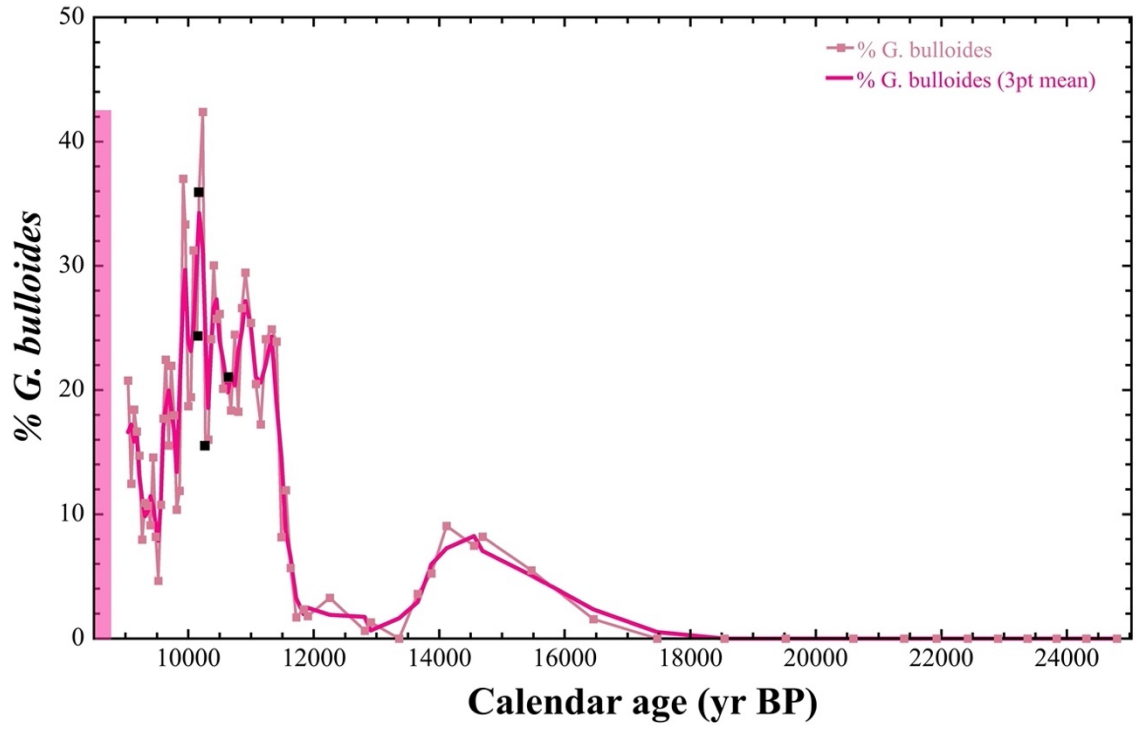

Figure 6.6: The relative abundance of G. *bulloides* at the Eirik Drift plotted against calendar age (yr BP). The light pink line indicates the non-smoothed record, and the pink line indicates the 3pt mean (smoothed) record. The black squares indicate the samples with <250 planktic foraminifera. The pink vertical bar represents the total range of % *G. bulloides*.

The range of the relative abundance for the non-smoothed record of *G. bulloides* varies between ~0–42%. The record shows two distinct peaks of increased abundance centered at ~14 000 yr BP (~9%) and ~10 200 yr BP (~42%). % *G. bulloides* is absent in the core samples from ~25 000 to ~16 500 yr BP, after which a gradual increase to ~9% is observed towards ~14 000 yr BP. A decrease to 0% at ~13 400 yr BP is followed by relatively minor fluctuations between 0–2% until ~11 700 yr BP. From ~11 700 yr BP to ~11 400 yr BP there is a notable and rapid increase in abundance of *G. bulloides* to ~25%, followed by an interval exhibiting high amplitude variability, varying between ~20 and 30% spanning the next 1 000 years until ~10 400 yr BP. A small decrease to ~16% (at ~10 300 yr BP) is observed prior to a rapid increase to ~42% (at ~10 200 yr BP). A gradual decreasing trend in abundance characterize the next 1 000 years. This is interrupted by an increasing trend initiated at ~9 300 yr BP that continues to ~9 000 yr BP with abundances close to 20% towards the end of the study interval.

6.2.3.2 Relative abundance of *G. glutinata*

The relative abundance (%) of *G. glutinata* is presented in Figure 6.7 plotted against age. In the non-smoothed record, there is one prominent peak centered around ~10 000 yr BP where the % *G. glutinata* abundance is almost ~6%. This is the highest value of % *G. glutinata* throughout the studied interval. *G. glutinata* is not present between ~25 000 and ~16 500 yr BP, and only small fluctuations between ~0–0.7% is observed during the time interval from ~16 500 to ~13 500 yr BP, with the highest (~0.7%) centered at ~13 800 yr BP. A general increasing trend is initiated at ~12 000 yr BP with superimposed decreasing-increasing fluctuations of ~3% most notable at ~10 700 yr BP and ~10 300 yr BP. After ~10 000 yr BP, there is a rapidly decreasing trend towards 0%. At ~9 300 yr BP, abundances remain close to 0% for 200 years until ~9 100 yr BP when the relative abundance increases to ~1%.

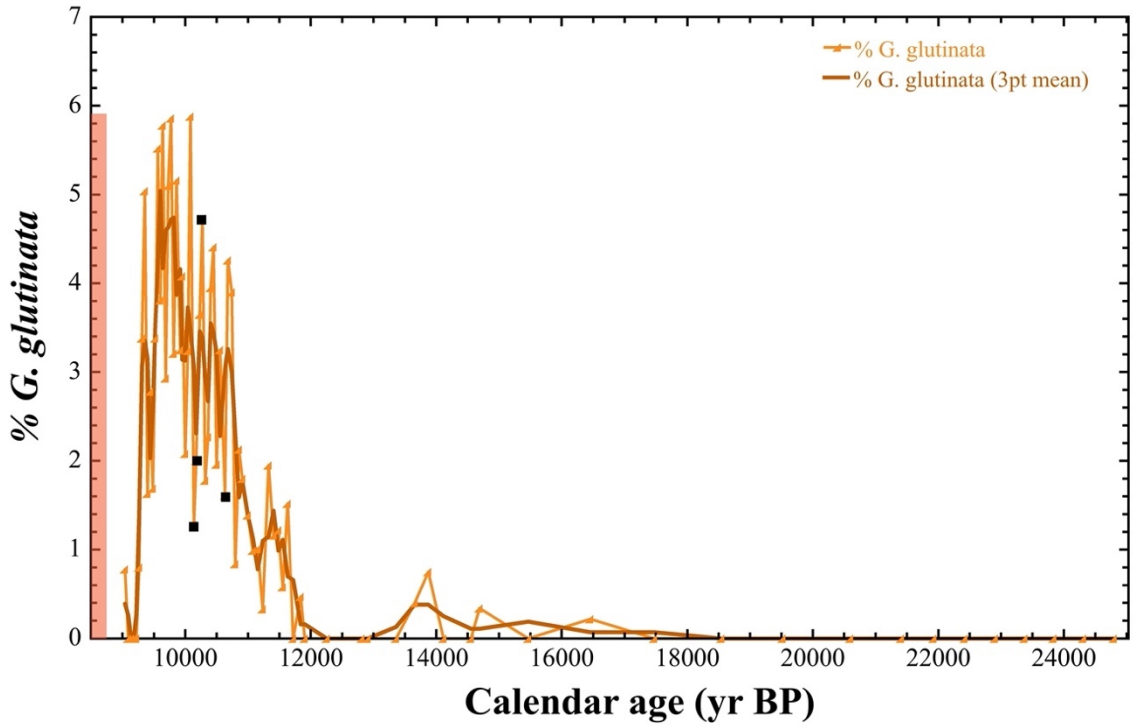

Figure 6.7: The relative abundance of *G. glutinata* plotted against age (yr BP). The orange line depicts the non-smoothed record, whereas the light brown line depicts the smoothed (3pt mean) record. The black squares indicate samples where the planktic foraminiferal abundance was <250 individuals. The orange vertical bar indicates the total range of % *G. glutinata*.

6.2.3.3 Relative abundance of *G. inflata*

The *G. inflata* relative abundance (%) is plotted versus age in Figure 6.8. The values are in the range of ~0–11%. *G. inflata* is more or less absent during the first ~10 500 years (~25 000 to ~14 500 yr BP) of the study interval, but after this, two distinct peaks and one minor peak can be observed between ~14 500 and ~9 000 yr BP in the non-smoothed record. A minor peak between ~14 500 and ~13 000 yr BP is observed with a maximum value of ~0.6% before abundances are reduced to 0% again. Following this minor peak, the % *G. inflata* starts to increase slightly to ~0.4% just after ~11 700 yr BP. This is followed by an increasing trend with amplitude variability of ~2% and ~6% towards ~10 300 yr BP, before a rapid increase to ~11% at ~10 200 yr BP. High and variable abundance fluctuations between ~1–3% characterizes the interval between ~10 200 and ~9 200 yr BP, after which a rapid increase to ~10% at ~9 100 yr BP is followed by a reduction to ~1% until ~9 000 yr BP.

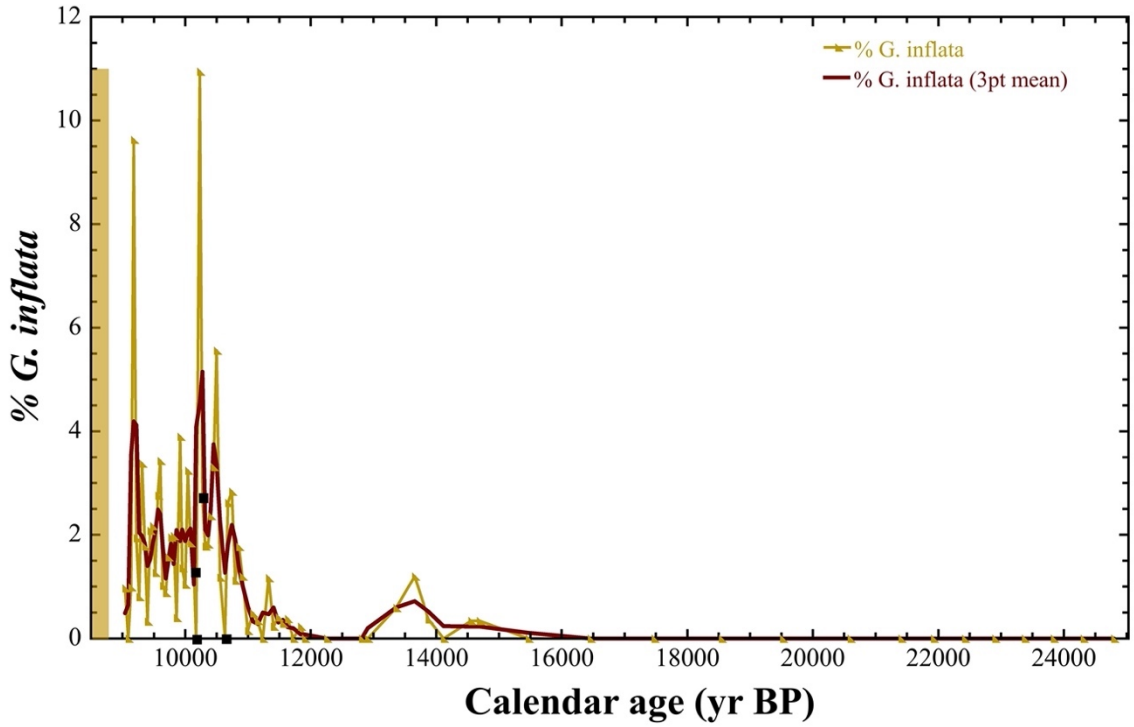

Figure 6.8: The relative abundance of *G. inflata* at the Eirik Drift plotted against age. The non-smoothed record is illustrated as a yellow line, and the smoothed (3pt mean) record as a dark brown line. The black squares represent samples containing less than 250 planktic foraminifera. The yellow vertical bar indicates the range of % *G. inflata*.

6.2.4 Coiling ratio of *N. pachyderma* (%)

The coiling ratio of *N. pachyderma* (% *N. pachyderma* in total of *N. pachyderma* + *N. incompta*) is plotted against calendar age (yr BP) and is shown in Figure 6.9. The inverted y-axis allows for better illustration of how the % *N. pachyderma* coiling ratio relates to temperature changes. A smoothed (3pt mean) record and a non-smoothed record are both plotted.

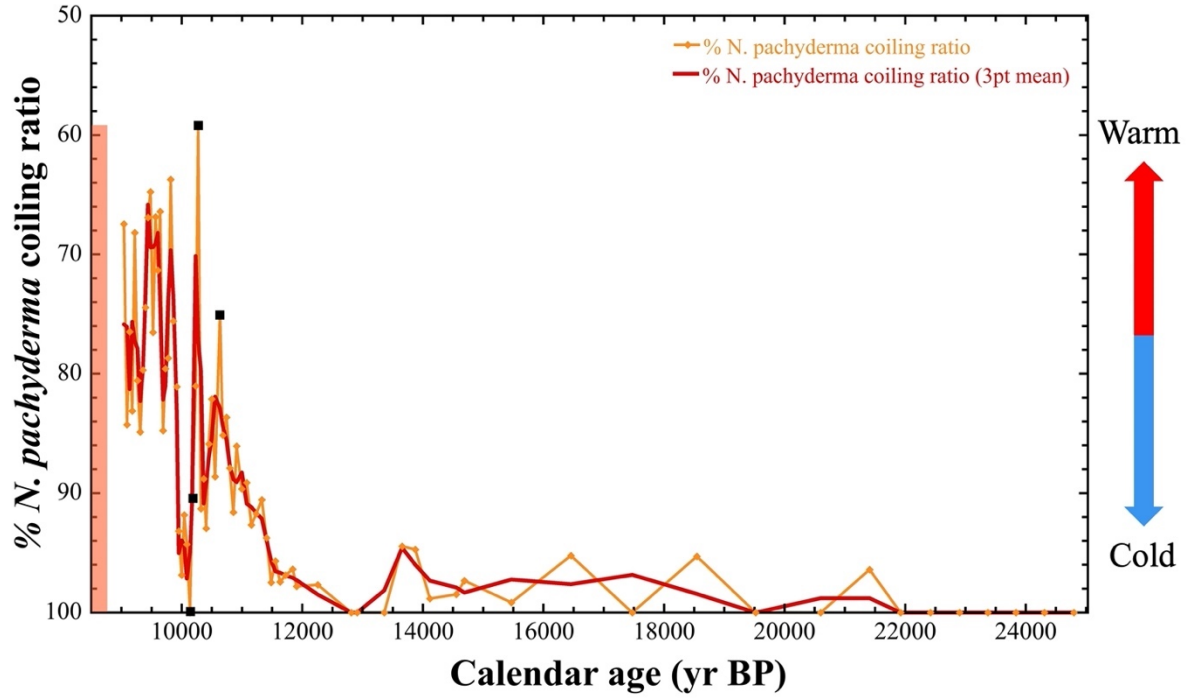

Figure 6.9: The % coiling ratio of *N. pachyderma* plotted versus calendar age (yr BP). The non-smoothed record is shown in orange, and the 3pt mean (smoothed) record is shown in red. The samples containing less than 250 planktic foraminifera are marked by black squares. The orange vertical bar represents the total range of the % *N. pachyderma* coiling ratio. The red vertical arrow depicts warmer temperature, whereas the blue vertical arrow depicts colder temperatures. The y-axis is inverted to show the change in % *N. pachyderma* coiling ratio relative to temperature changes.

The % *N. pachyderma* coiling ratio for the non-smoothed record exhibits two warmer peaks during the period leading up to ~11 700 yr BP. The values range from ~60–100% throughout the studied interval. The coiling ratio is observed to be high and relatively stable at 100% throughout the period ~25 000–11 700 yr BP with minor decreases to ~95% centered at ~21 500, ~18 500, ~16 500 and ~14 500–14 000 yr BP. A small decrease to ~85% characterizes the interval between ~11 700 and ~10 700 yr BP before a sudden decrease to ~75% is observed at ~10 600 yr BP. An increase to ~90% is followed by another sudden and rapid decrease to ~60% at ~10 300 yr BP. Here, the insufficient total entities of planktic foraminifera could possibly explain the large difference between the two values of ~75% and ~60% compared to the surrounding samples which has values of ~80–85%, and hence these results need to be interpreted carefully. By ~10 000 yr BP, the % *N. pachyderma* coiling ratio increases to 100%, also interpreted from a sample with insufficient total entities of planktic foraminifera, but in this case, high % coiling ratio of ~90–95% is observed in the samples before and after. At ~9 900 yr BP the coiling ratio decreases towards ~9 000 yr BP with rapid fluctuations that vary between ~65–85%.

6.3 Lithic counts

The relative abundance (%) of IRD at the core site is shown in Figure 6.10 plotted against calendar age (yr BP).

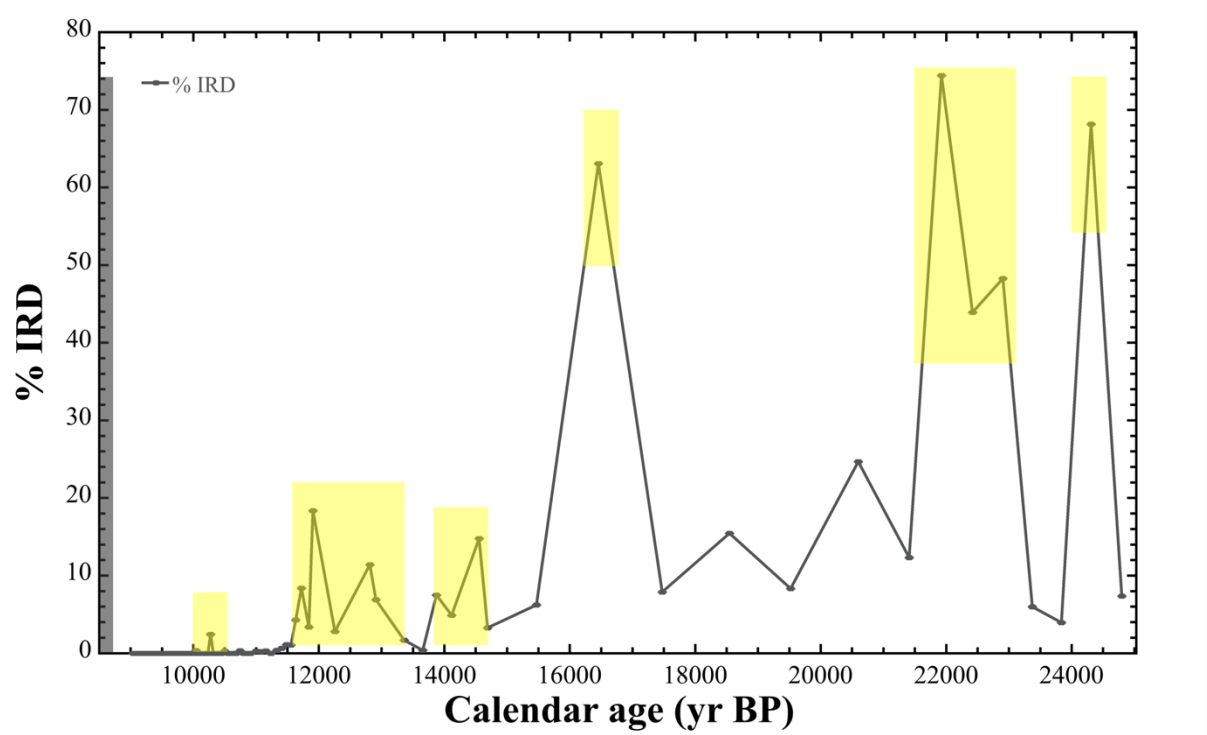

Figure 6.10: The % IRD plotted versus calendar age (yr BP) at the core site. The grey vertical bar denotes the range of % IRD. The yellow bars represent notable peaks with high IRD concentration.

The IRD percentages range from ~0 to ~75% throughout the studied interval. During the LGM, and the early parts of the deglaciation (~25 000–20 000 yr BP), there are two prominent peaks of high % IRD observed. At ~24 300 yr BP IRD % reaches ~68% followed by a rapid decrease to ~5% at ~23 500 yr BP. A second two-step increase of IRD to a peak of ~75% is centered at ~22 000 yr BP. The interval from ~21 500 yr BP to ~17 500 yr BP spans two smaller IRD peaks of ~25% and ~15% centered at ~18 500 yr BP and ~20 500 yr BP respectively. The latter part of the deglacial (~17 500–11 700 yr BP) at the Eirik Drift is characterized by one major peak, followed by four smaller peaks with variable IRD %. The major peak at ~16 500 yr BP exhibits IRD abundances of ~63%, followed by a decrease down to ~4% right before an increase to ~15% at ~14 500 yr BP with IRD present in the core samples until ~13 600 yr BP. The IRD abundance increase again in the ~600-year interval leading up to ~13 000 yr BP, and two small,

but significant IRD peaks of ~12% and ~18% are observed at ~12 800 yr BP and ~11 900 yr BP, respectively, separated by a short-lived interval exhibiting values of ~3%. Subsequent fluctuations in IRD, between ~4% and ~8%, lasts until ~11 500 yr BP after which there is a decrease to ~0–1% IRD with the onset of the Holocene period. A minor peak of ~2% is observed in the early Holocene at ~10 300 yr BP. After this, IRD is absent in the rest of the core samples towards the end of the studied interval (~9 000 yr BP).

6.4 Combined relative planktic foraminiferal abundances and ice-rafted debris

The combined planktic foraminiferal abundance and % IRD from Core MD03-2665 are plotted versus age (yr BP) in Figure 6.11. The planktic foraminifera abundances show similarities throughout the studied interval with peaks of all species, except for *N. pachyderma*, during warmer intervals. In the colder intervals, the polar planktic foraminifera (*N. pachyderma*) thrives.

The relative abundances of the planktic foraminiferal species show distinct similarities during three intervals: the B/A interstadial, the YD interval, and the early Holocene. During the LGM and the beginning of Heinrich Stadial 1 (~17 500–14 500 yr BP) all planktic foraminifer species are absent with the exception of *N. pachyderma* and *N. incompta*. The *N. incompta* species usually resides in warmer waters than *N. pachyderma*, and the presence of *N. incompta* could be a result of higher percentage of aberrant forms (~5%) than corrected for (3%, after Darling et al. (2006)). Leading up to the beginning of the B/A interstadial, the warmer species increase in small percentages before a prominent advance of a few percentages can be observed throughout the B/A. % *N. pachyderma* decreases simultaneously as the warmer species occupy more of the foraminiferal fauna. A decrease of all species, except for *N. pachyderma* that exhibits an increase, occurs towards the end of B/A and into the YD. Low planktic foraminifera abundances characterize the YD period except for *N. pachyderma* which increases, and this is consistent with colder temperatures. % *N. incompta* begins to slowly increase during the first part of the YD, much earlier than the other warmer species that only start to increase relatively late in the YD interval. As observed during the previous interglacial periods (e.g., Irvali et al., 2020), % *N. pachyderma* decreases towards the end of YD as the other species increase. Towards the start of the Holocene period, from ~11 700 yr BP, all warm species increase rapidly, except % *G. inflata* which increases initially slower and later more rapidly at ~11 000 yr BP. The relative abundance of *N. pachyderma* decreases rapidly around the same time. Similar trends for all the species are observed in the Holocene with a cooling around ~10 000 yr BP observed in all species except for *G. bulloides* which seems to decrease later. A warming trend characterize the period after ~10 000 yr BP with the exception of *G. bulloides* which starts to increase at ~9 300 yr BP. A reduction of *G. glutinata* and *G. inflata* occurs simultaneously to low values at ~9 300 yr BP before increasing slightly until ~9 000 yr BP.

The % IRD relative to the foraminiferal abundances are especially prominent at ~16 500 yr BP, ~14 500 yr BP, ~11 900 yr BP and ~10 300 yr BP with a decrease of temperate species and a ~100% presence of *N. pachyderma*. The first large peak of % IRD that corresponds to changes in the foraminiferal abundances can be observed at ~16 500 yr BP. Following this, is a gradual increase in foraminiferal abundance of temperate species which could correlate to what is observed after Heinrich events when an increase in temperature occurs (Max et al., 2022). The second prominent event occurs at ~14 500 yr BP showing an increase of all species except for *N. pachyderma* and *G. bulloides*. The increase in IRD % at ~11 900 yr BP is portrayed as a slightly delayed increase in all species by ~11 700 yr BP except for *N. pachyderma* which decreases. Following the ~10 300 yr BP event, which is small compared to the three previous events, there is a rapid cooling observed in almost all the species centered at ~10 000 yr BP.

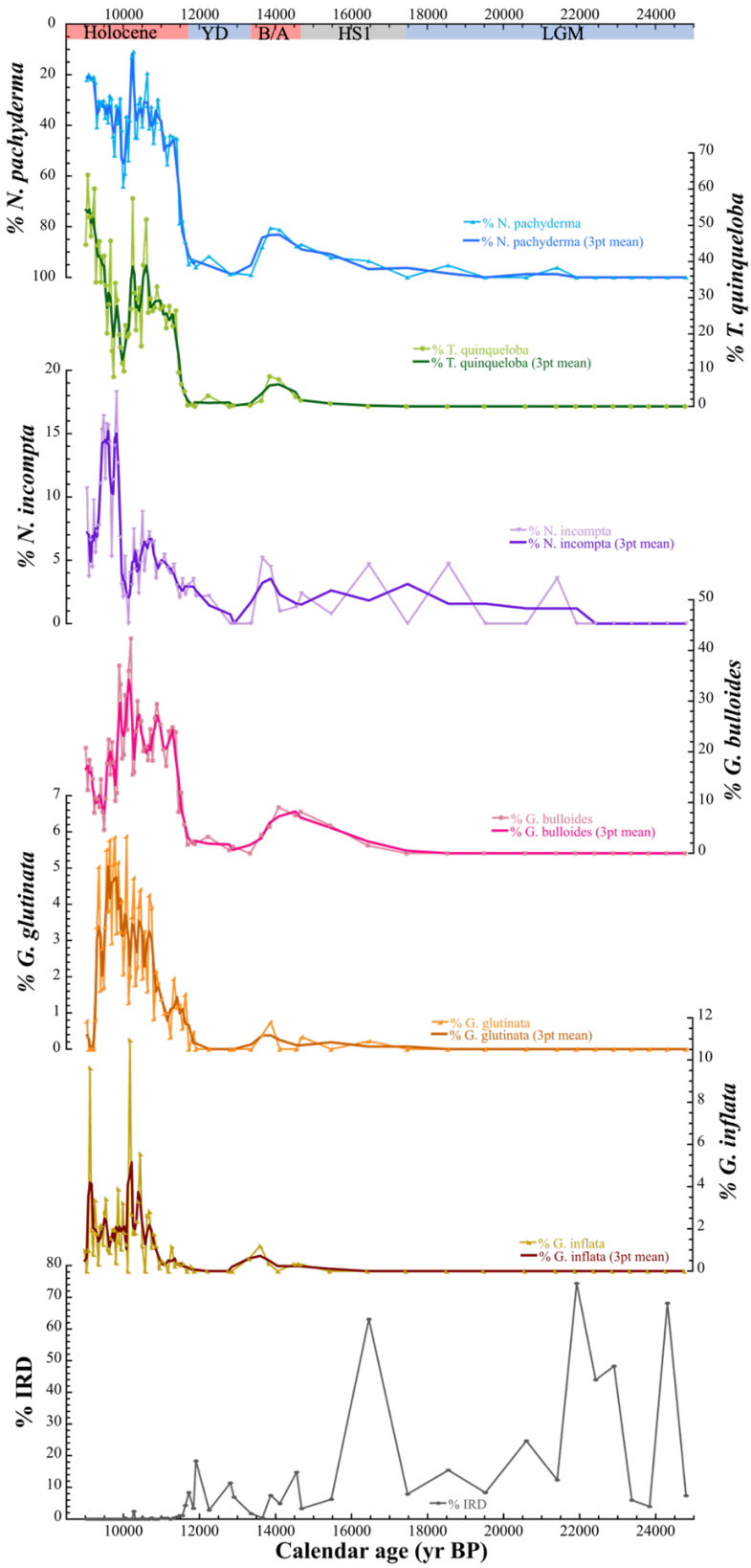

Figure 6.11: The relative abundance of the most common planktic foraminiferal species and IRD % at the core site are plotted together versus age (yr BP). Intervals for Holocene, YD, B/A and the LGM are marked in red and blue horizontal bars representing warm and cold periods. HS1 is marked by a light grey horizontal bar. % *N. pachyderma* are shown in blue, % *T. quinqueloba* in green, % *N. incompta* in purple, % *G. bulloides* in pink, % *G. glutinata* in orange, % *G. inflata* in brown and % IRD in grey. Lighter colors indicate the non-smoothed records.

7 Discussion

New high resolution planktic foraminiferal assemblages and IRD counts from Core MD03-2665, produced as part of this thesis, provide novel insights on the climate, ocean fronts and ice sheet variability over the last deglaciation. In this chapter, I will interpret the planktic oxygen isotope record, planktic foraminiferal assemblages, and IRD % data from Core MD03-2665 and discuss these in the context of previously published records from the Eirik Drift (Core MD99-2227) as well as the broader North Atlantic. Previous work from Core MD99-2227 has mainly focused on the GIS sediment discharge and retreat over the last ~450 000 yr BP (Carlson et al., 2008; Colville et al., 2011; Reyes et al., 2014; Hatfield et al., 2016). Comparing MD03-2665 *N. pachyderma* % and IRD % data to previously published GIS sediment discharge records from southern Greenland will provide important insight on GIS variability from LGM to early Holocene. On the other hand, a comparison of MD03-2665 planktic foraminiferal assemblages and IRD % to previously published records from the broader North Atlantic region (e.g., ODP Sites 980 and 983) will allow us to better understand the evolution of North Atlantic climate, ocean front positions and surface ocean hydrology over the last deglaciation.

7.1 Oxygen isotopes versus *N. pachyderma* coiling ratio

To assess whether the *N. pachyderma* $\delta^{18}O$ exhibits a temperature or salinity change during the Holocene it is necessary to compare it with other records, such as the *N. pachyderma* coiling ratio and IRD %. High *N. pachyderma* coiling ratio indicates cold and polar conditions and if the coiling ratio decreases this indicates warmer conditions. If the changes observed in *N. pachyderma* coiling ratio are accompanied by similar changes in *N. pachyderma* $\delta^{18}O$ (e.g., an increase in *N. pachyderma* coiling ratio coeval with a switch to higher $\delta^{18}O$ would suggest a cooling event; and vice versa), this might help us distinguish whether the $\delta^{18}O$ signal is influenced by freshwater or temperature. Hence, changes in both *N. pachyderma* coiling ratio and *N. pachyderma* $\delta^{18}O$ indicate changes in temperature. Adding IRD % to the comparison could also clarify whether both temperature and salinity changes have influenced the *N. pachyderma* $\delta^{18}O$ record. However, for the LGM and deglacial period it is not as straight forward. The $\delta^{18}O$ record is influenced by both large ice volume and sea level changes which

also affects the $\delta^{18}O$. According to Fairbanks (1989), a 0.011‰ increase in $\delta^{18}O$ corresponds to a sea level decrease of 1 m. During the last deglacial, large volumes of continental ice melted and was added to the ocean influencing the sea level, salinity, and temperature of the surface ocean in the North Atlantic. The sea level during the LGM was ~120 m lower than the modern sea level and rose rapidly at different rates during the last deglacial (Fleming et al., 1998; Peltier & Fairbanks, 2006; Stanford et al., 2011a).

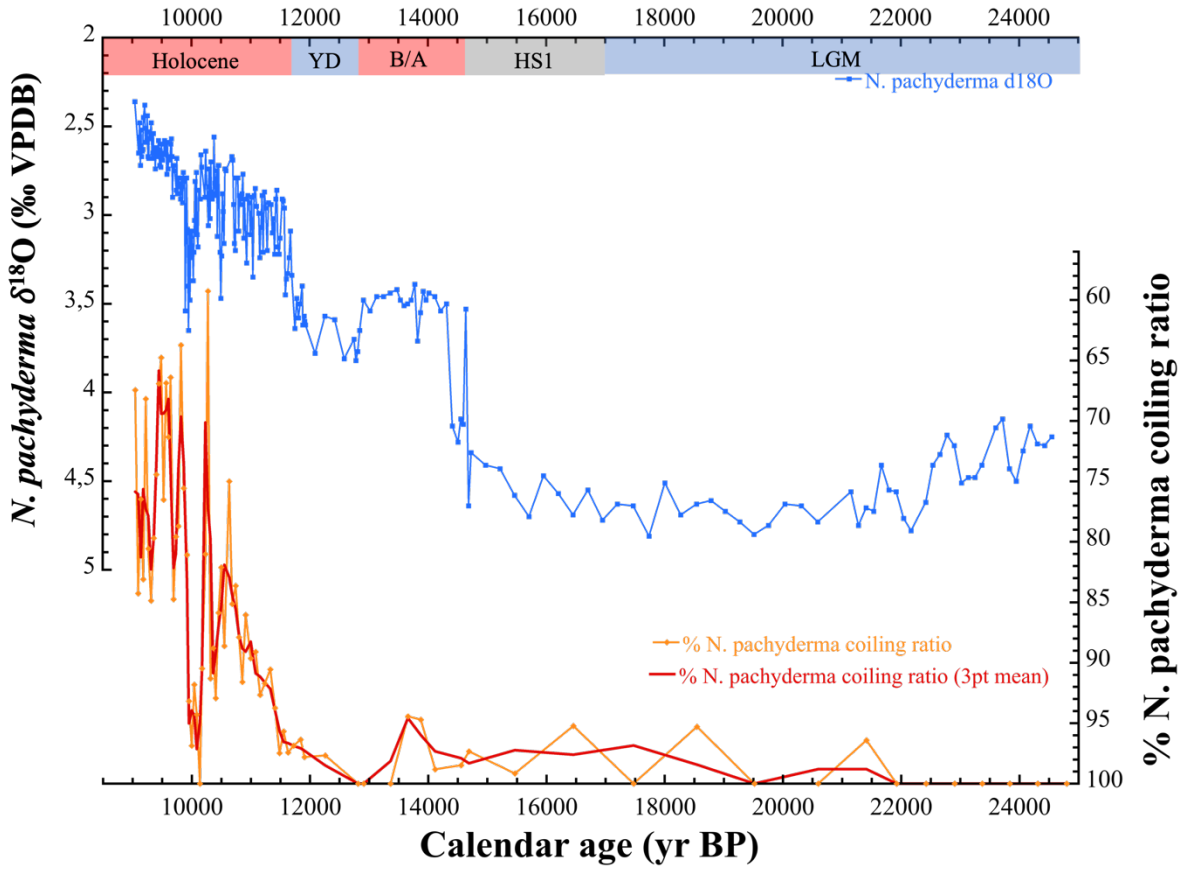

Figure 7.1: *N. pachyderma* $\delta^{18}O$ and *N. pachyderma* coiling ratio (%) versus age (calendar yr BP) for the studied period (~25 000–9 000 yr BP). Holocene, YD, B/A, HS1 and LGM are marked in red, blue and grey bars.

The $\delta^{18}O$ record and the *N. pachyderma* coiling ratio can together be used to infer SST variability. The records, shown in Figure 7.1, show small fluctuations during the LGM and into the last deglaciation. During the LGM period the $\delta^{18}O$ record seems to illustrate increasing values from ~25 000 yr BP to ~22 000 yr BP when the *N. pachyderma* coiling ratio is at 100%. Stable $\delta^{18}O$ records together with small fluctuations of *N. pachyderma* coiling ratio (between

~95 to ~100%) during the LGM and the last deglaciation until ~14 700 yr BP, indicates that the climate was still cold.

During the B/A period, a warming (and/or freshening) seems to have occurred based on the decreased planktic $\delta^{18}O$ beginning at ~14 700 yr BP. However, the coiling ratio only decreases to ~94% during the B/A. A relatively high % IRD in the last deglaciation leading up to the B/A period could explain why the planktic $\delta^{18}O$ decreases significantly (~1.11‰) while the *N. pachyderma* coiling ratio is still high as more freshwater might have been added to the region, potentially decreasing the $\delta^{18}O$ signal. The sea level also rose rapidly during the first ~500 years (~20 m) as a result of a meltwater pulse (Lambeck et al., 2014), probably accounting for some (~0.22‰) of the ~1.11‰ $\delta^{18}O$ decrease observed. Looking at the other planktic foraminiferal abundances during this period (Figure 6.11), an increase occurs in more temperate (subpolar to transitional) species, whereas the polar *N. pachyderma* decreases. This indicates that there also was an increase in surface ocean temperatures. Hence, the rapid ~1.11‰ decrease in $\delta^{18}O$ in the early part of the deglacial was likely not only influenced by temperature (1.11‰ = 4.8ºC), but also by changes in freshwater and sea level.

During the YD, both the planktic $\delta^{18}O$ record and the *N. pachyderma* coiling ratio increases. The $\delta^{18}O$ increases by ~0.3‰ while the coiling ratio increases up to 100% in the beginning of the YD (~12 800 yr BP). The $\delta^{18}O$ decreases by ~0.5‰ towards the end of the YD (~11 700 yr BP) while the *N. pachyderma* coiling ratio also decreases by ~5%, marking the end of the cold period. These coeval changes in foraminiferal assemblage and geochemistry suggest a clear cooling at the onset of YD with an even larger warming terminating the YD and marking the onset of the Holocene.

Following the YD, both the *N. pachyderma* $\delta^{18}O$ and coiling ratio continue to decrease indicating a warming (or freshening) of the near-surface waters. During the early Holocene, both *N. pachyderma* $\delta^{18}O$ and the *N. pachyderma* coiling ratio show a high frequency variability. The most pronounced event over the early Holocene seems to be an abrupt cooling event centered at 10 000 yr BP, recorded by a 1‰ increase (~4.3ºC cooling) in *N. pachyderma* $\delta^{18}O$ and a ~55% increase in the *N. pachyderma* coiling ratio marking a return to cold conditions. Similarly, a small anomaly, but relatively high increase in $\delta^{18}O$ of ~1‰ centered around ~10 000 yr BP, has also been found in a mean $\delta^{18}O$ curve from the Greenland ice cores

(DYE-3, GRIP and NGRIP) where it is linked to temperature change (Rasmussen et al., 2007). The timing also closely corresponds in time to Bond event number 7 at 10 300 yr BP (ice rafting events from the Laurentide Ice Sheet in the North Atlantic) (Bond et al., 2001). Bond events have been found to correspond to periods of drying and cooling conditions in the U.S. and Asia (Parker et al., 2006). Therefore, it is probably a decrease in temperature that is responsible for the $\delta^{18}O$ change observed. Only a minor peak (~2%) of % IRD at ~10 000 yr BP is observed during this period (Figure 6.11) which could be a last purge from the GIS which retreated off the continental shelf and on land around this time (Bennike & Björck, 2002). This would not influence the $\delta^{18}O$ significantly which is probably why it is not observed in the record. Following the cooling event at ~10 000 yr BP, the *N. pachyderma* $\delta^{18}O$ record follows a gradual decreasing trend for the remainder of the study interval (to ~9 000 yr BP), indicating warming within the early Holocene.

7.2 Changes in ocean fronts and hydrology

Planktic foraminiferal abundances are an important tool in tracing surface ocean conditions and the positions of oceanic fronts. In the North Atlantic, the main water masses are the Polar water, the Arctic water and the Atlantic water. The Polar water is a low-saline, cold water mass mostly influenced by the EGC at the study site. The Arctic water is also cold but has higher salinity. These water masses are separated by the Polar Front (PF) which during summer lies close to the sea ice edge, following the Greenland and eastern Canadian continental margins (Figure 7.2). It acts as a barrier in the North Atlantic Ocean, constraining sea ice and icebergs (Eynaud et al., 2009). The Atlantic water is a warm and high-saline water mass which is separated from the Arctic water by the Arctic Front (AF) (Swift & Aagaard, 1981; Johannessen et al., 1994; Alonso-Garcia et al., 2011).

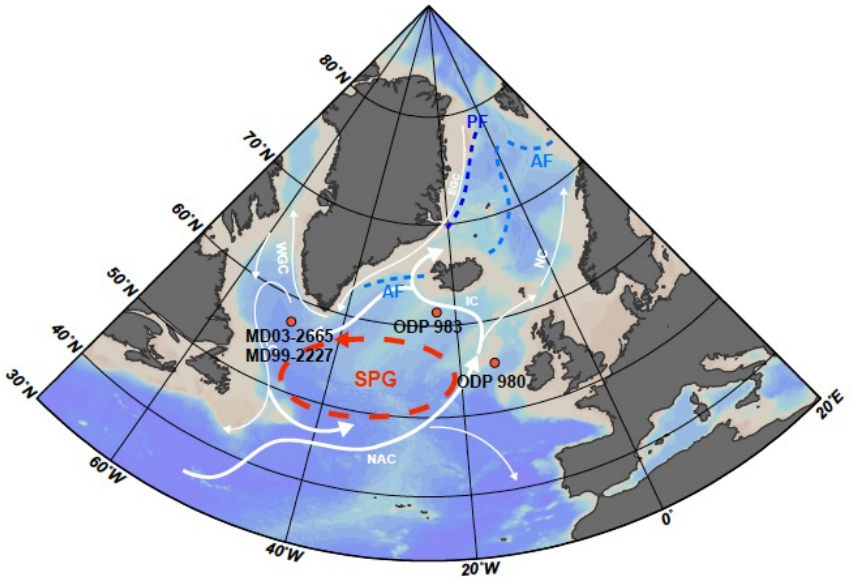

Figure 7.2: Map of the modern positions of the Polar and Arctic fronts. Surface currents displayed in white (NAC: North Atlantic Current, NC: Norwegian Current, IC: Irminger Current, EGC: East Greenland Current, WGC: West Greenland Current, LC: Labrador Current). The Subpolar Gyre (SPG) is marked in red. Core sites mentioned in the discussion (MD03–2665, MD99-2227, ODP 983, ODP 980) are marked in red circles. Modified from Irvali et al. (2016).

Planktic foraminifera, such as *N. pachyderma*, *N. incompta*, *T. quinqueloba* and *G. bulloides*, can be used to trace the past positions of the PF and the AF (e.g., Alonso-Garcia et al., 2011; Mokeddem et al., 2014; Irvali et al., 2016). *N. pachyderma* is an indicator species for cold polar water masses and low foraminifera flux with high abundances of *N. pachyderma* indicate Polar waters. In the Arctic water, the foraminifera flux is high, and the most abundant species is *N. pachyderma*. In Atlantic water, high foraminifera flux with high abundances of temperate species such as *N. incompta*, *T. quinqueloba* and *G. bulloides* are observed. *T. quinqueloba* is normally very abundant in areas with high foraminifera flux, east of the AF. A combination of high *N. pachyderma* and high *T. quinqueloba* can therefore be used to trace the position of the AF (Johannessen et al., 1994; Alonso-Garcia et al., 2011). Figure 7.3 shows the positions of the PF and AF during different climatic phases. During glacial terminations, the PF and AF are both positioned further south starting to retreat northwards, while during early interglacial phases the fronts are to the north – closer to their modern locations (Alonso-Garcia et al., 2011). *N. pachyderma* occurrences of 96–99% are generally associated with Polar and Arctic waters while areas influenced by warmer Atlantic water typically decreases the *N. pachyderma* abundance to 50% while the abundance of more temperate species increases (Husum & Hald, 2012).

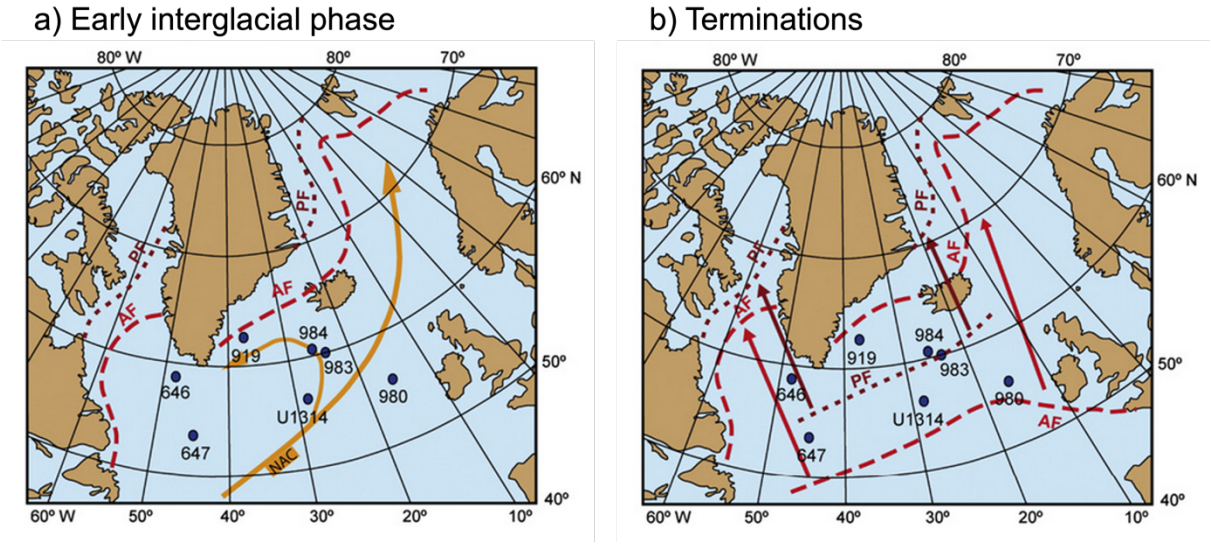

Figure 7.3: Possible positions of the Polar Front (PF) and the Arctic Front (AF) in the North Atlantic during (a) early interglacial periods and during (b) terminations. Modified from Alonso-Garcia et al. (2011).

Figure 7.4 shows the distribution of *N. pachyderma* abundance (%) in the North Atlantic during modern versus LGM, based on the MARGO project planktic foraminifera census data for the Atlantic Ocean (Kučera et al., 2005c). Near ~100% *N. pachyderma* abundance at approximately ~50ºN during the LGM suggests that the PF was most likely in its southernmost location at this time, although it has been documented to move as far south as 40ºN during the late Pleistocene cold events (Eynaud et al., 2009).

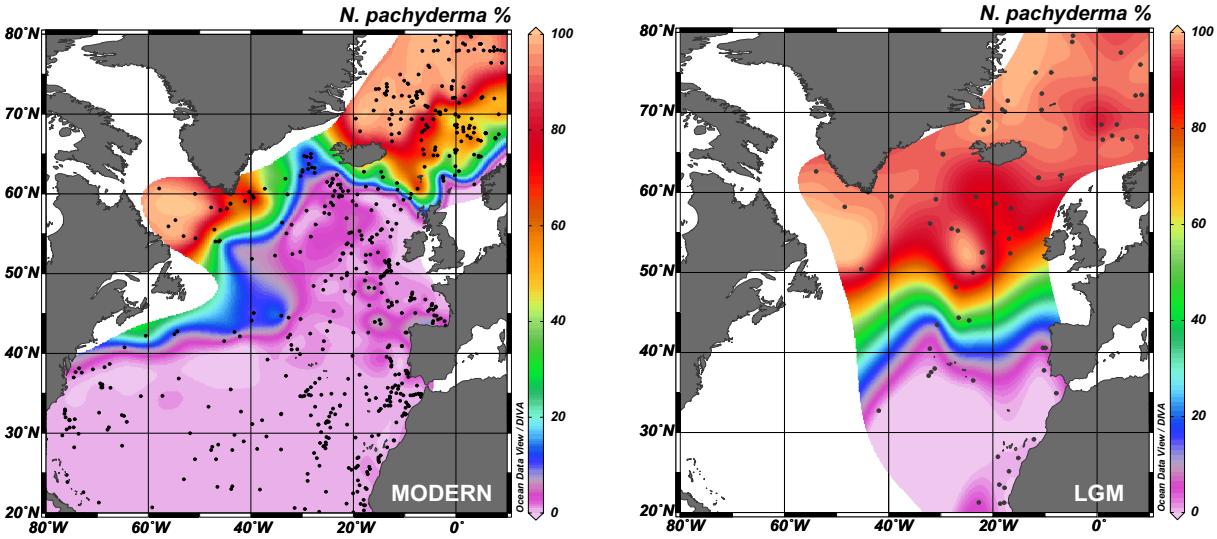

Figure 7.4: Distribution of *N. pachyderma* abundance (%) in the North Atlantic during modern and LGM, based on the MARGO project planktic foraminifera census data for the Atlantic Ocean (Kučera et al., 2005c), plotted using the Ocean Data View (version 5.6.3). Black dots represent the locations of modern core tops (Kučera et al., 2005a) and sediment cores with LGM samples (Kučera et al., 2005b) in the North Atlantic.

In the Eirik Drift records, a ~100% abundance of the polar species *N. pachyderma* over the LGM also confirms that the PF was south of this site. No variations in the planktic foraminiferal assemblages are observed until HS1 when a small increase in *G. bulloides* % is observed. There are also no abundances of the AF indicator, *T. quinqueloba*, during the HS1. Moreover, the *N. pachyderma* % starts to slightly decrease but still exhibits a high percentage (~90–94%). The *N. incompta* % exhibits relatively stable values (~0–4 %) but should be interpreted carefully as explained in Chapter 6.4 by a possible coiling failure of >3%. The planktic foraminiferal abundance during HS1 indicates that the Eirik Drift was still within the PF.

During terminations, the PF and AF retreat northwestwards (e.g., Alonso-Garcia et al., 2011; Mokeddem et al., 2014; Irvali et al., 2016). During the early Holocene, the fronts migrated north of the Eirik Drift which can be observed in the planktic foraminifera assemblages consisting of the temperate species associated with the warm Atlantic water mass (e.g., *T. quinqueloba*, *N. incompta*, *G. bulloides*) at the Eirik Drift (Figure 7.5). At sites 980 (Feni Drift) and 983 (Gardar Drift) (Figure 7.3) in the subpolar North Atlantic, the abundance of *N. pachyderma* starts to decrease earlier than at the Eirik Drift. However, it is important to note that high age offsets might also be due to different age model approaches used, as both ODP Site 980 (Benway et al., 2010) and 983 (Barker et al., 2015) data is discussed based on their original age scales. At Site 980, Atlantic water was present by ~17 000 yr BP indicated by a decrease of *N. pachyderma* abundance from near-100% to ~50% (Benway et al., 2010). At the Eirik Drift site, the area was still occupied by Polar waters as the *N. pachyderma* % was close to 100%. This indicates that the oceanic fronts had started to migrate northwest of Site 980 at ~17 000 yr BP. At Site 983, Atlantic water masses seems to have been close to the site twice during the deglacial, during HS1 and the end of B/A based on the assumption that ~50% *N. pachyderma* is representative of the AF (Figure 7.6, panel B), before occupying the site in the early Holocene (Barker et al., 2015) indicating that the AF was fluctuating between Site 980 and 983 through the last deglaciation. At the Eirik Drift, the AF most likely reached and moved past the site in the early Holocene, as indicated by a decrease to ~50% of *N. pachyderma* and an increase to ~30% of *T. quinqueloba*.

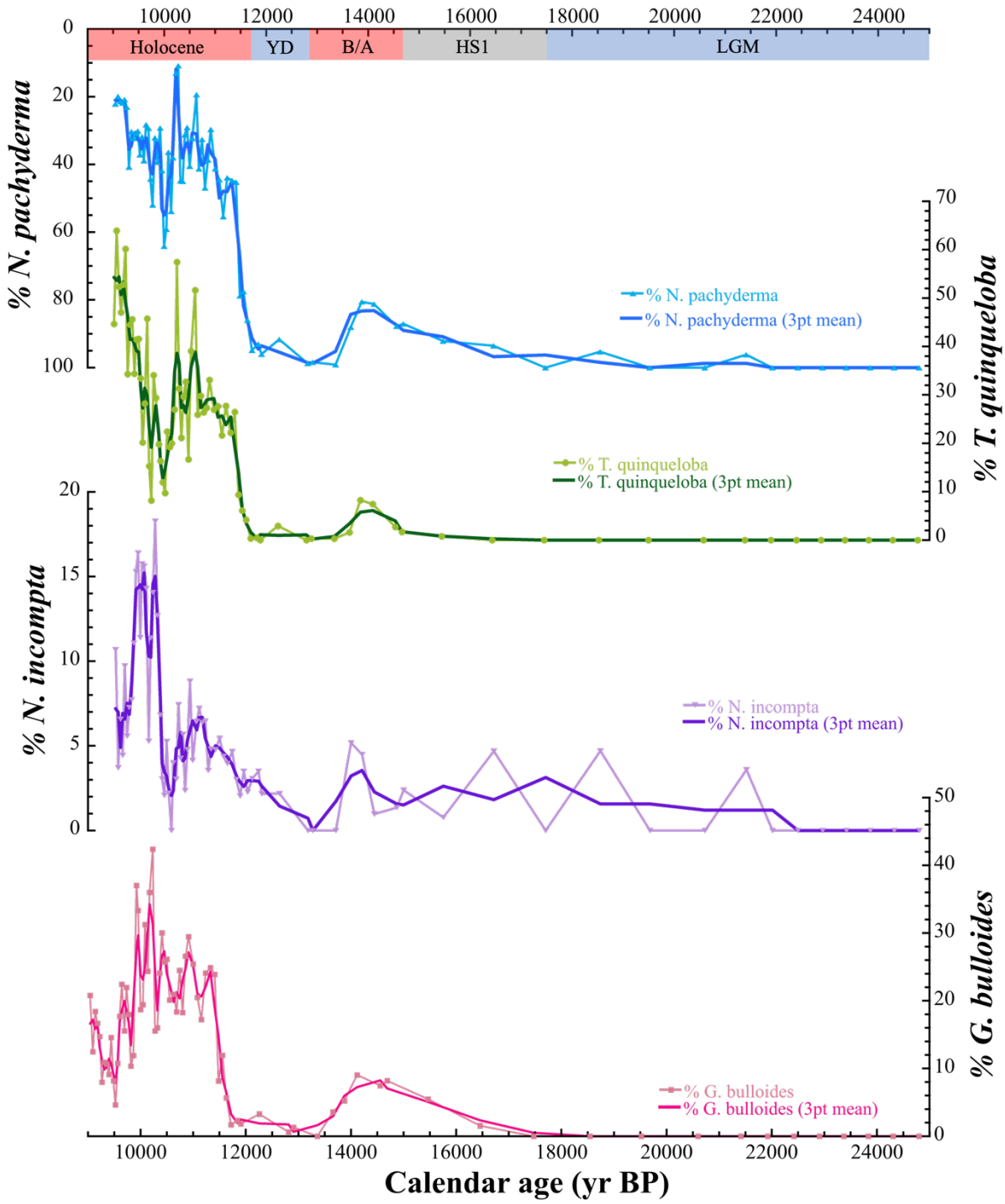

Figure 7.5: Planktic foraminiferal abundances from the Eirik Drift versus age (yr BP). *N. pachyderma* (blue), *T. quinqueloba* (green), *N. incompta* (purple) and *G. bulloides* (pink) are the most abundant species at the Eirik Drift and can be associated with the movement of oceanic fronts.

During the early Holocene, the abundance of *N. pachyderma* fluctuates between ~30–40% before a decrease to ~15% at ~10 300 yr BP. Following this decrease, an increase in *N. pachyderma* % of ~50% to ~65% occurs at ~10 000 yr BP indicating a rapid cooling event. Some of the samples in this time interval contained less than 250 planktic foraminifera and

therefore needs to be interpreted carefully. However, the other samples in the same time interval contained sufficient planktic foraminifera and confirm the same decreasing trend. Furthermore, a decrease in both the subpolar species, *T. quinqueloba* and *N. incompta*, from ~57% to ~9% and ~8% to 0%, respectively, occurs at the same time supporting the rapid cooling event. *G. bulloides* % exhibit a decrease from ~40% right before ~10 000 yr BP to ~10% during the ~10 000 yr BP event. The $\delta^{18}O$ also increases significantly by 1‰ in ~290 years – corresponding to a cooling of ~4.3ºC (or freshening of 1.84) at ~10 000 yr BP. No significant IRD % is observed in this period which could exclude iceberg transport to the site. Therefore, it is most likely that a rapid cooling event occurred, and possibly oceanic frontal positions shifted southward.

Following this rapid cooling there is an equally rapid transition back to warmer conditions. This transition occurs over a period of ~90 years, as inferred from the *N. pachyderma* $\delta^{18}O$ record. Following this cooling event during the early Holocene, *N. pachyderma* % decreases and fluctuates between ~30–40%. The subpolar and transitional planktic foraminiferal species increases during this period. *T. quinqueloba* % increases to ~64% by ~9 000 yr BP and *N. incompta* % fluctuates between ~5–15% until ~9 000 yr BP. The *G. bulloides* % increases steadily to ~20% during this period. No IRD is present in the samples indicating that the surface waters were too warm for icebergs to survive. Therefore, it is likely that the $\delta^{18}O$ decrease of ~0.89‰ (~3.8ºC) is representative of a warming rather than a freshening.

During modern times, the *N. pachyderma* abundance is around ~80% at the Eirik Drift (Figure 7.5) which is higher than during the early Holocene. This indicates that the AF was most likely further north than today and that the surface waters were warmer as Atlantic waters likely occupied the area. This is supported by a high abundance of the subpolar and transitional species during the early Holocene (Figure 7.5) as well as no IRD occurrences (Figure 7.6, Panel C).

The last deglaciation at the Eirik Drift, is thus characterized by an additional outstanding temperature anomaly at ~10 000 yr BP in addition to Heinrich Stadial 1 (HS1) and the Younger Dryas (YD) cold event. In structure and abruptness, it is similar to the 8.2 kyr BP event also resolved in the same core (Kleiven et al., 2008). What could drive such a rapid near-surface cooling event so late in the deglacial, when most major ice sheets (Laurentide and Fennoscandia) had retreated?

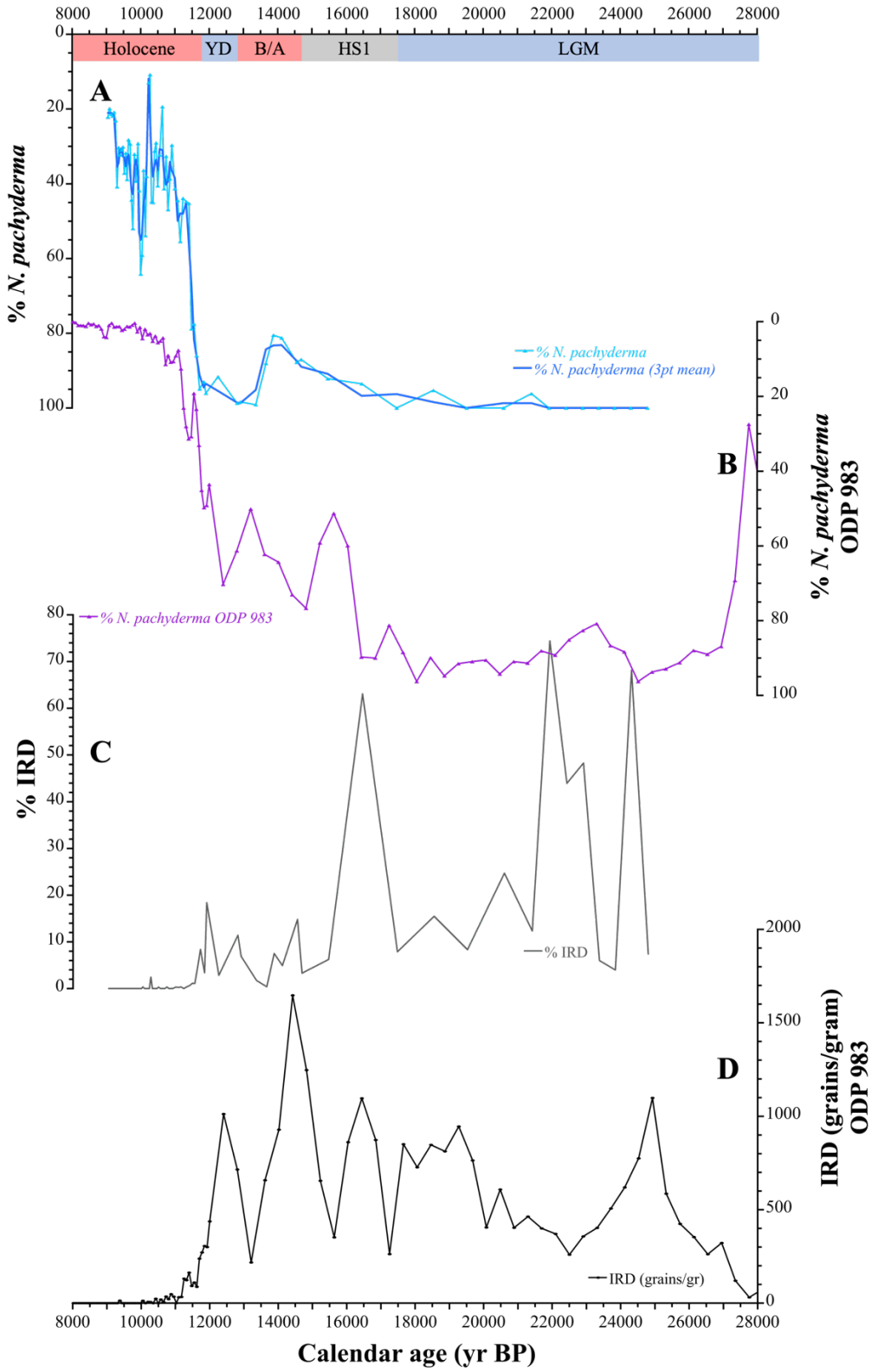

Figure 7.6: The % *N. pachyderma* for MD03-2665 (blue line, Panel A) and ODP Site 983 (Barker, 2021) (purple line, Panel B), % IRD for MD03-2665 (grey line, Panel C) and IRD grains/gram for ODP Site 983 (Barker, 2021) (black line, Panel D) versus calendar age (yr BP) from 8 000–28 000 yr BP. Each record is plotted with their respective age model. The Holocene, YD, B/A, HS1 and the LGM are shown by red, blue, and grey horizontal bars.

There is evidence that this might be more than a local signal, since it is also observed in the GRIP, NGRIP and DYE-3 ice cores (Rasmussen et al., 2007), pointing to yet another similarity with the 8.2 event. Both the YD and the 8.2 event are postulated to be driven by a catastrophic freshwater drainage in the North Atlantic (Clark et al., 2001; Clarke et al., 2003; Broecker, 2006). In addition to the lake releases during these two well-documented climate events, Teller et al. (2002) also found evidence for freshwater outbursts from North American proglacial lakes at 10 600, 10 400, 10 300 and 10 000 yr BP. Thus, meltwater releases from these lakes could also be the cause or mechanism behind the rapid oscillation at ~10 000 yr BP. To verify this, more detailed studies of the magnetic grain sizes, XRF (X-Ray Fluorescence) records and provenance studies of the sediment grains at the Eirik Drift core site is needed. It is interesting to note however, that the early last interglacial period at this site also exhibits a rapid cooling (the 126 kyr BP cooling event) (Irvali et al., 2012) which also has been tied to reductions in deep water ventilation (Galaasen et al., 2014).

7.3 IRD and ice sheet variability

7.3.1 Comparison to GIS discharge records

Irvali and co-workers' study on the Greenland Ice Sheet demise during the late Pleistocene demonstrate that changes in the SST south of Greenland correlate with temperature and changes in the GIS (Irvali et al., 2020). Over the deglacial there is also evidence for changes in Greenland melt, for example during the YD period (Jennings et al., 2006). Given this potential relationship, the following section will explore how the subpolar gyre changes at MD03-2665 relates to evidence for GIS variability over the last deglacial.

The Sr-Nd-Pb isotope composition of the silt size fraction in the Eirik Drift core MD99-2227 have previously been used to document changes in the sourcing of sediment from south Greenland's three Precambrian bedrock terranes and has been used to infer changes in the ablation and magnitude of the southern GIS retreat over the last ~450 000 years (Colville et al., 2011; Reyes et al., 2014; Hatfield et al., 2016). The location of Core MD99-2227 and the three southern Greenland terranes (Nagssugtoqidian Mobile Belt (NMB), Archean Block (AB) and Ketilidian Mobile Belt (KMB)) are shown in Figure 7.7.

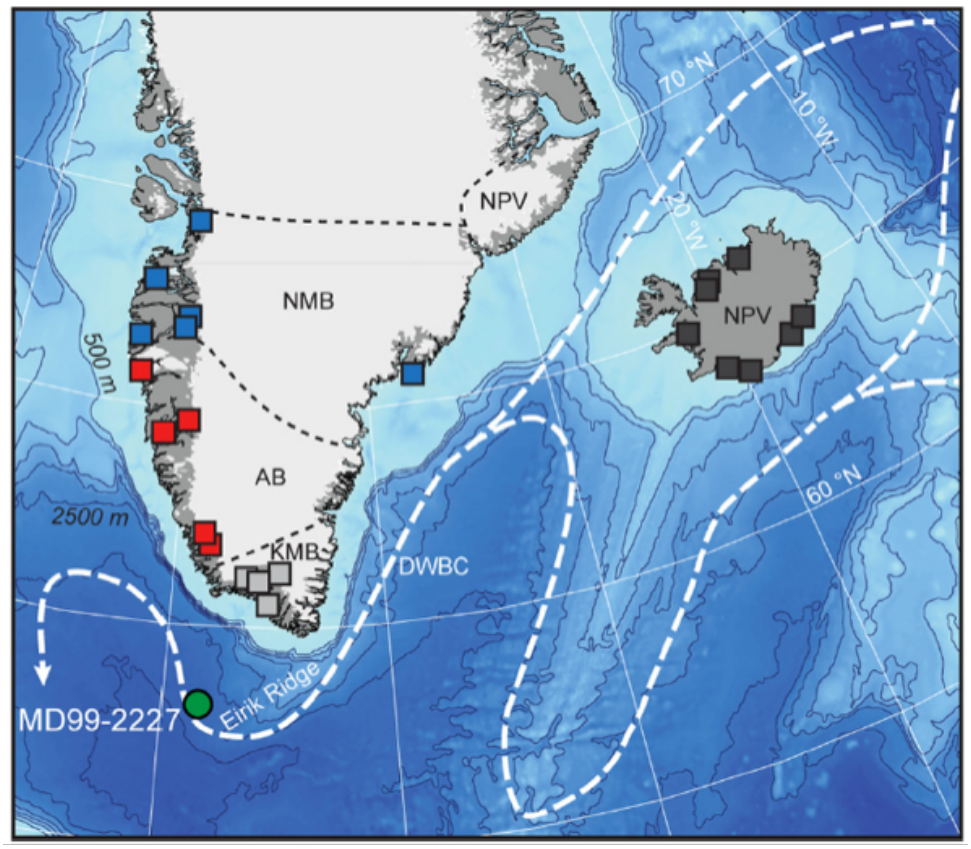

Figure 7.7: Greenland and Icelandic provenances. Core location for MD99-2227 is marked in a green circle. The DWBC is marked by white dashed lines. Squares represent sampled sites of terrestrial source terranes. NMB: Nagssugtoqidian Mobile Belt (blue squares), AB: Archean Block (red squares), KMB: Ketilidian Mobile Belt (grey squares), NPV: Neogene and Paleogene Volcanics (black squares). From Hatfield et al. (2016).

Comparison of MD03-2665 surface climate records to GIS sediment discharge and retreat (Colville et al., 2011; Hatfield et al., 2016) provides insights on GIS variability over the last deglaciation. Figure 7.8 shows the comparison between GIS discharge records (PG % and the fraction of total sediment composed of southern Precambrian Greenland silt for the NMB, AB and KMB terranes) from Core MD99-2227 and *N. pachyderma* % and IRD % from Core MD03-2665. The ages of Core MD99-2227 is tuned to the same age model as Core MD03-2665 using the approach presented in Chapter 5.

During the LGM and the early Termination 1 (T1), Core MD99-2227 records show large amounts of IRD transported to the site, as well as reduced transport of PG silt to the site, which is indicative of a calving of the southern GIS which reached out on the continental shelf (Hatfield et al., 2016). This is consistent with the high IRD % in Core MD03-2665 during this interval. High and stable *N. pachyderma* $\delta^{18}O$ in both cores as well as high *N. pachyderma* % in Core MD03-2665 indicates that the climate was cold.

In the B/A, a warming seems to have occurred based on the lower *N. pachyderma* % (~80%) in Core MD03-2665 and a rapid decrease in the *N. pachyderma* δ^{18}O signal at both sites of ~1‰. An increase in the PG % of ~15% (from ~48% to ~63%) occurs during the B/A, followed by a decrease to ~47% at the onset of the YD (~12 800 yr BP). The PG % rapidly increases back to ~67% at ~12 400 yr BP before decreasing to ~50% at the end of the YD. The high PG silt % indicates increased ablation and a retreat of the southern GIS. The total sediment shows a similar trend with increased total sediment during the peaks of elevated PG % and a decrease of ~30% at the onset of the YD when PG % decreases. This could imply that the southern GIS re-advanced or experienced a still-stand during the beginning of the YD, but continued to deliver sediment to the Eirik Drift as the discharge records still show sediment transportation. The *N. pachyderma* % is high (~95%) during the YD indicating colder surface conditions. The *N. pachyderma* δ^{18}O signal at both core sites exhibit a slight increase of ~0.3‰ from the B/A to the YD, supporting a temperature decrease. At the end of the YD, PG % and total sediment decreases and stabilize until ~10 000 yr BP. However, the *N. pachyderma* δ^{18}O records and the *N. pachyderma* % show a decrease indicating a possible warming (or freshening).

Rapid and sustained increases in PG % characterize the early Holocene (~10 200–8 600 yr BP). This is indicative of increased ablation and supports a retreat of the GIS (Hatfield et al., 2016). The same can be inferred from the ~30% increase in the silt provenance record (Colville et al., 2011) during the same period. The increased ablation and retreat seem to stabilize after ~8 000 yr BP. It is likely that although the southern GIS had retreated off the continental shelf during T1, ice still persisted on southern Greenland during the early Holocene as evidenced by the presence of silt derived from all three terranes.

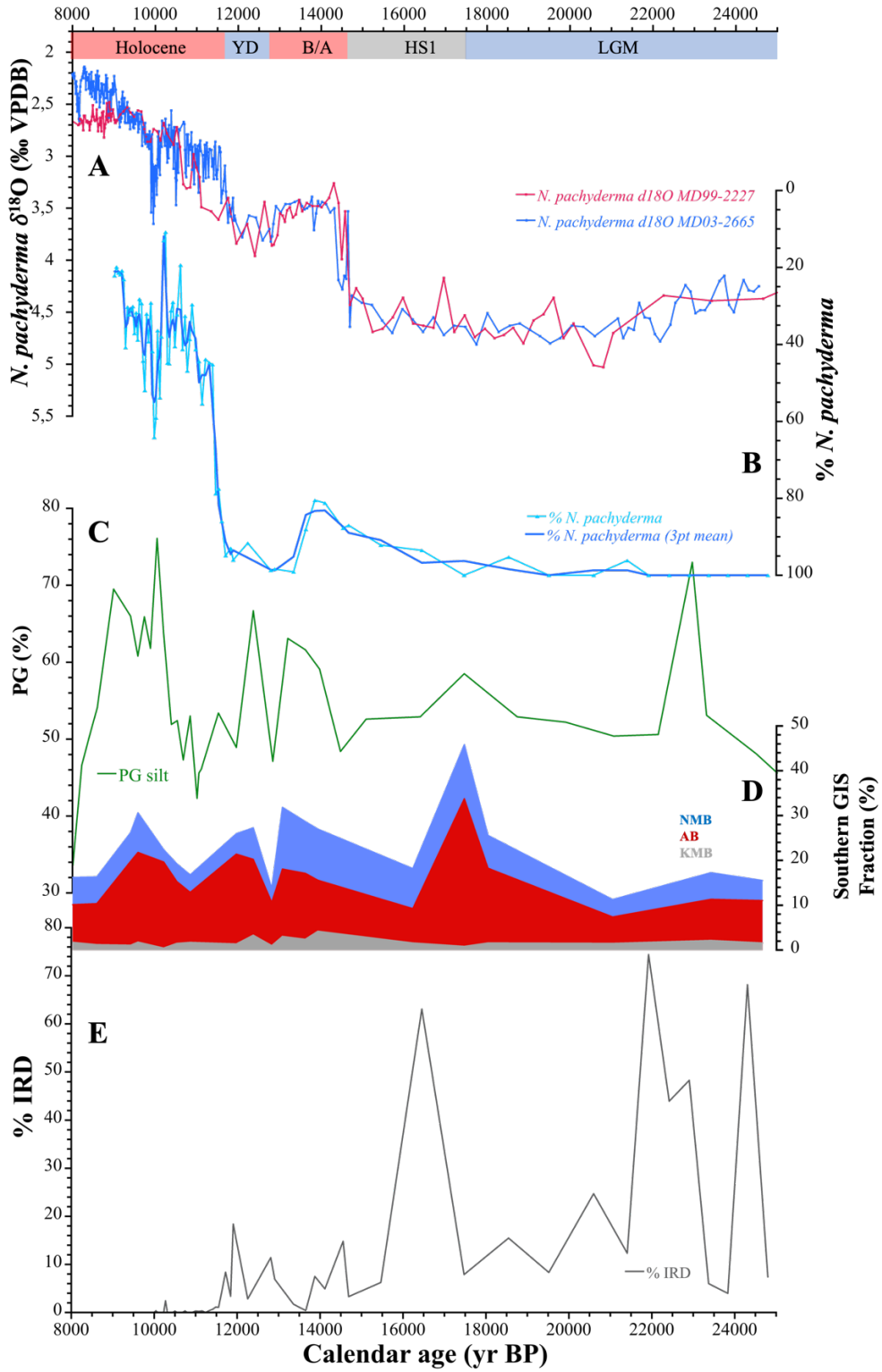

Figure 7.8: GIS discharge records from cores MD03-2665 (this study) and MD99-2227 (Colville et al., 2011; Hatfield et al., 2016) plotted against age (calendar yr BP). Panel A: *N. pachyderma* δ^{18}O from MD99-2227 (pink) and MD03-2665 (blue), Panel B: % *N. pachyderma* from MD03-2665, Panel C: Precambrian Greenland (PG) silt (%) from Hatfield et al. (2016), Panel D: Silt provenance (% of total sediment) from Colville et al. (2011), Panel E: % IRD from MD03-2665. NMB: Nagssugtoqidian Mobile Belt, AB: Archean Block, KMB: Ketilidian Mobile Belt. The records from Core MD99-2227 (*N. pachyderma* δ^{18}O, PG silt and silt provenance) are plotted using the same age model approach as for Core MD03-2665. Holocene, YD, B/A, HS1 and LGM are shown in red, blue, and grey horizontal bars.

7.3.2 IRD variability at the Eirik Drift

Distinct periods of high IRD deposition can be observed in many North Atlantic sediment cores during the last glacial-interglacial period. During these periods, short events of elevated IRD deposition, that are termed Heinrich (H) events, occur. These events are most prominent in the IRD belt located between 40º–55ºN in the North Atlantic (Ruddiman, 1977). The sources of the carbonate-rich Heinrich layers mainly stem from the Laurentide Ice Sheet (LIS) with icebergs following the LC and melting along the southern border of the SPG. At the Eirik Drift, sedimentation mainly stems from the DSOW transporting and depositing sediment from the Greenland Ice Sheet (GIS) (Davies et al., 2021). Therefore, tracing H-events on the Eirik Drift can be difficult as it is located outside of the main IRD belt. IRD deposited on the Eirik Drift mainly originates from the Greenland and Icelandic ice sheets (e.g., Bond & Lotti, 1995; Elliot et al., 1998) and yields different geochemical signals than the typical Heinrich layers. However, the core site is well situated to monitor GIS activity and iceberg calving events during the last interglacial period as documented by Irvali et al. (2016). In the following, new constraints on the co-evolution of North Atlantic climate and ice sheet changes during the last deglacial will be discussed.

In Figure 7.9 the *N. pachyderma* δ^{18}O signal is plotted with % *N. pachyderma* and % IRD versus age spanning the LGM through the early Holocene (25 000–8 000 yr BP). High and stable *N. pachyderma* δ^{18}O and *N. pachyderma* % characterize the LGM interval at the Eirik Drift. High and variable IRD % are present during this period with two distinct peaks occurring at ~24 300 yr BP (~70%) and ~22 000 yr BP (~75%). Hence, the various proxy records indicate that the climate was cold and that ice sheets were present discharging sediment-laden icebergs into the ocean that survived transport to the Eirik Drift site, possibly from the GIS. This is consistent with reconstructions showing the GIS reaching the continental shelf during the LGM (e.g., Carlson et al., 2008). Smaller peaks of IRD (~20%) are observed in the latter part of the LGM (~21 500–17 500 yr BP). This could potentially be explained by the ice sheet(s) delivering IRD to the Eirik Drift has started to retreat from its LGM maximum position. Planktic isotopes and IRD records from east Greenland also document a GIS retreat between 20 000–18 000 yr BP providing a consistent picture of a retreating GIS (Andrews et al., 1997). The *N. pachyderma* % record suggests polar conditions continued as there are high abundances (~100%) during this time and the δ^{18}O record exhibits stable conditions throughout the LGM.

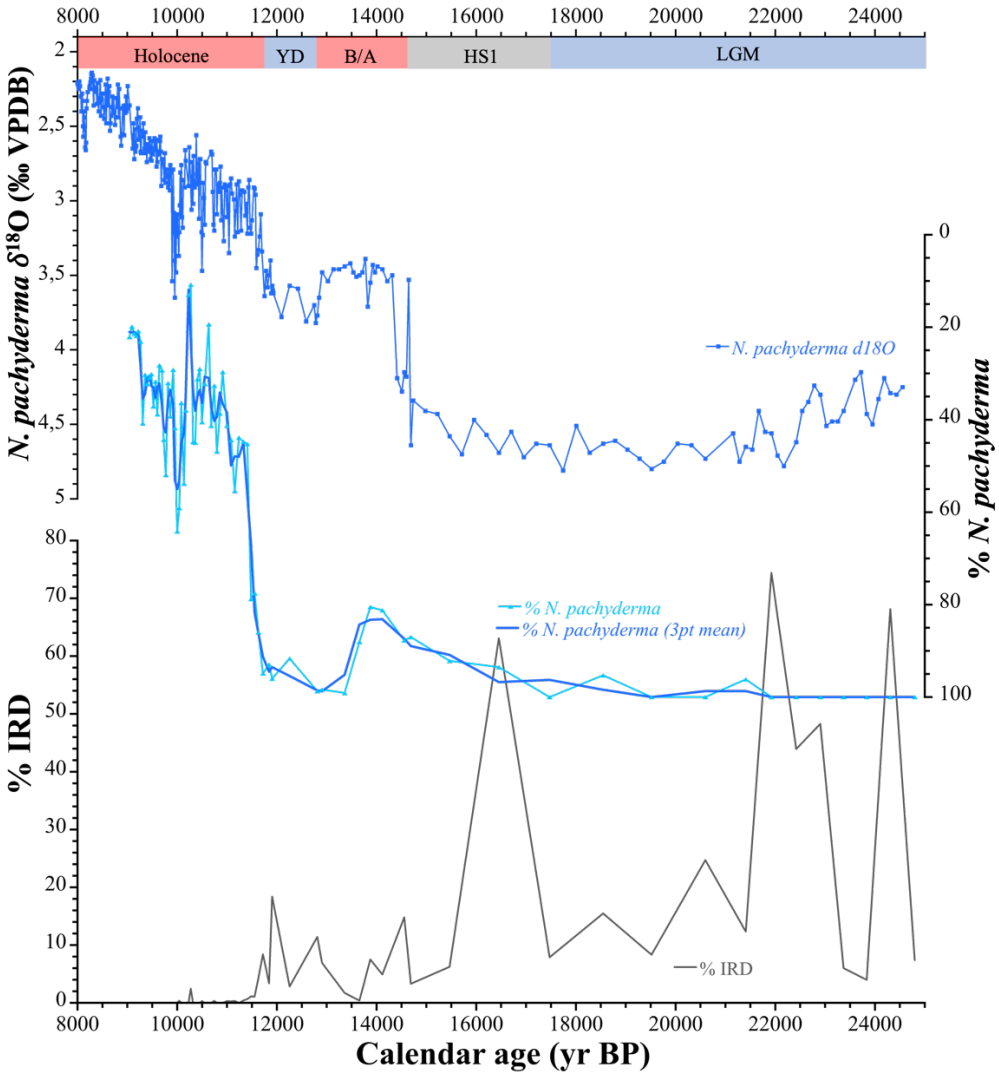

Figure 7.9: % *N. pachyderma* δ^{18}O, % *N. pachyderma* and % IRD from the Eirik Drift plotted versus calendar age (yr BP) from 8 000–25 000 yr BP. The warm periods, Holocene and B/A are marked in red bars, the cold periods YD and LGM are marked in blue bars and HS1 is marked in a grey bar.

At the start of the deglaciation, during HS1, the IRD record exhibits one major peak of ~65% centered at ~16 500 yr BP. This is also consistent with the IRD records from ODP Site 983 at the Gardar Sediment Drift (Barker et al., 2015), demonstrating a coherent signal south of Greenland and south of Iceland. A gradual decrease in the *N. pachyderma* % from ~100% to ~80% is observed between ~17 500 to ~14 000 yr BP suggesting a trend toward slightly less polar water conditions. A gradual warming trend of the surface water during HS1 has also been observed based on measurements of deep water corals in the western North Atlantic basin (Thiagarajan et al., 2014). The lack of a similarly clear decreasing trend in the δ^{18}O record prior to the sharp decrease at the onset of the B/A, suggests that there were only minor changes in temperature or salinity in the surface waters during this initial phase of declining polar species

conditions. However, the slight increase of both temperate species, *N. incompta* and *G. bulloides*, confirms that the polar conditions were breaking up gradually during the HS1 prior to the sudden B/A warming.

Following the large IRD peak during HS1, the IRD % decreases to ~15% during the B/A. The *N. pachyderma* % decreases to ~80% in this period whereas the $\delta^{18}O$ rapidly decreases by ~1.1‰ indicating a ~4.8ºC warming (or freshening of ~2). The IRD % decrease during the B/A to ~15% which might indicate that less icebergs survived transportation to the site. In combination with an increase in almost all the subpolar and transitional species displayed in Figure 7.5, the likely source of the observed $\delta^{18}O$ decrease is warmer surface waters or increased influence of the relatively warm IC at the site. As discussed in Chapter 7.2, the frontal positions had started to shift north during this period, which would allow increased ocean heat transport with the NAC/IC to the site.

The YD is characterized by low IRD %, similar to the B/A, but with *N. pachyderma* abundances of ~95–100%. A decrease in all the temperate foraminiferal species indicates cooler surface temperatures which can also be inferred from the slight increase in *N. pachyderma* $\delta^{18}O$ (~0.2‰) at the onset of YD. At ~12 000 yr BP (Figure 7.10) there is still high *N. pachyderma* % (~100%) and IRD % indicating that the climate was cold, and icebergs were present, transporting sediment to the core site. At ~11 600 yr BP the *N. pachyderma* decreases rapidly to ~45% by ~11 400 yr BP indicating a warming. The IRD % drops close to zero indicating that iceberg supply decreased and/or icebergs did not survive transport to the site. The $\delta^{18}O$ values drop in the same period by ~0.7‰ indicating a temperature increase of ~3ºC which corresponds to the interpretation of a temperature increase reflected in the reduced *N. pachyderma* % and the IRD %. Data from the eastern GIS suggest a retreat at the latter part of the YD interval (Jennings et al., 2006). Following the transition towards a warm interglacial climate, there are significant oscillations observed in several of the climate proxies from ~11 200 yr BP to ~9 000 yr BP. One prominent increase in the $\delta^{18}O$ occur around ~10 000 yr BP and is accompanied by an increase in *N. pachyderma* % and decrease in the more temperate planktic foraminifera species, indicating a rapid cooling event. Between ~10 300 to ~10 000 yr BP, small increases in IRD % indicates that it was again cold enough for icebergs to reach the core site, although the peak IRD % is still very low (~3%). This supports the interpretation of a rapid cooling event. After this event, the climate seems to stabilize towards the onset of the Holocene period, with lower $\delta^{18}O$ values and lower *N. pachyderma* % and no IRD transport to the site.

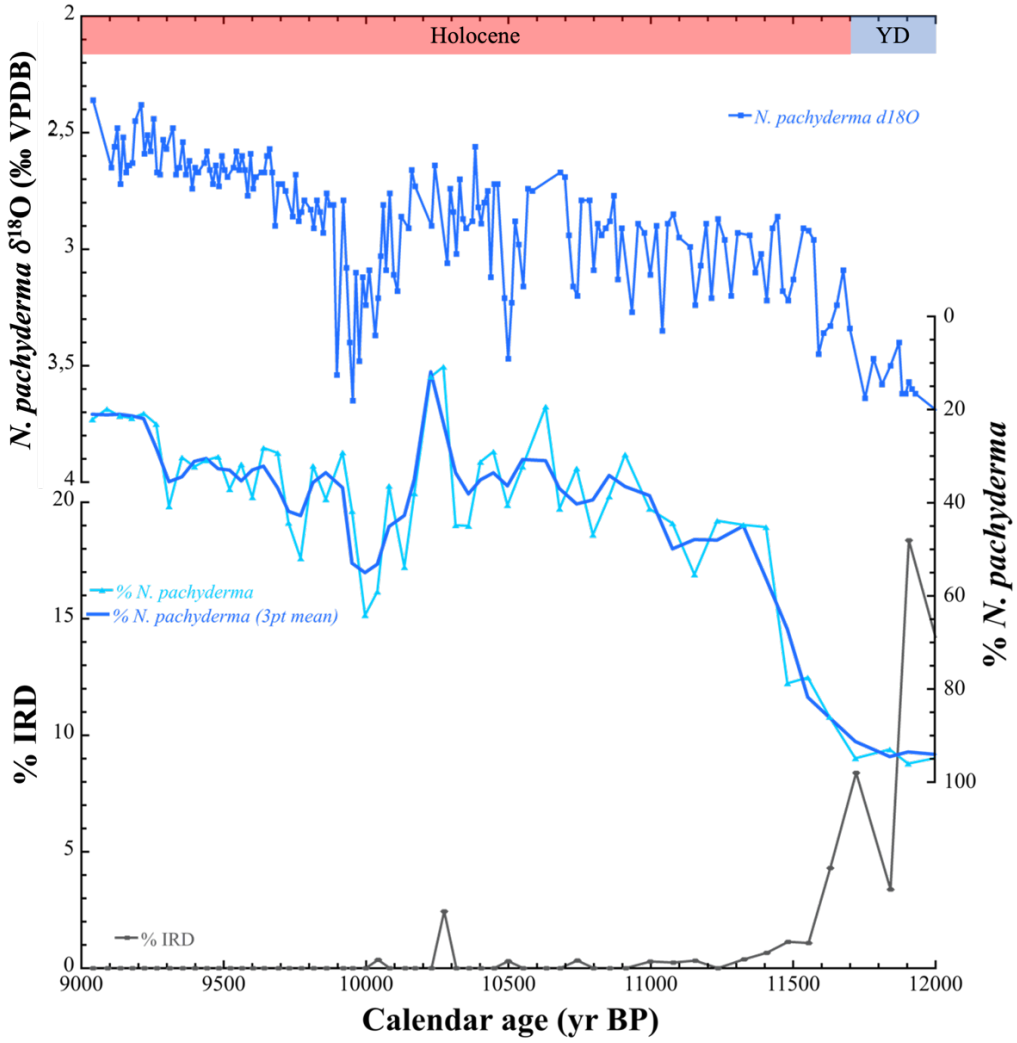

Figure 7.10: *N. pachyderma* δ^{18}O, *N. pachyderma* % and IRD % from the Eirik Drift site plotted against age zoomed in to the early Holocene (12 000–9 000 yr BP). The Holocene is marked in a red bar and the YD is marked in a blue bar.

Some of the IRD peaks in the Eirik Drift record fall within the same periods as H1 (~17 500–16 500 yr BP) (Hemming, 2004) and H2 (~26 000–24 000 yr BP) (Hemming, 2004) (Figure 7.9). These are the peaks that fall between ~17 500–15 500 yr BP (peak at ~16 500 yr BP) and between ~25 000–24 000 yr BP (peak at ~24 300 yr BP). As the sedimentation rate during the LGM and the deglaciation is significantly lower than during the early Holocene, the samples counted with 4 cm spacing has a resolution of ~1 000 years, according to the age model. This could account for why the IRD peaks appear to be so long in duration, and it would thus be preferable to increase the resolution during these intervals (H1 and H2) to better assess the duration of these events.

7.3.3 Spatial pattern of IRD changes in the subpolar North Atlantic

The IRD record off southern Greenland provides new evidence for glacial activity in Greenland during the LGM and exhibits a stepwise decrease in the flux of IRD towards the Holocene. The IRD record most likely reflect waxing and waning of the GIS (Carlson et al., 2008), and we assume that there is a high degree of correlation between the advance of the GIS to the coast and the continental shelf, and the magnitude of IRD peaks in the open ocean sediments at the Eirik Sediment Drift. To explore the relationship between local changes and broader changes in the basin, the IRD record is compared to that of ODP Site 983 from the Gardar Sediment Drift in the subpolar North Atlantic south of Iceland (Figure 7.6). This site is chosen because it provides a comparable high-resolution depiction of the deglacial period (Barker et al., 2015).

The Eirik Drift IRD % follows the same overall trend as the subpolar North Atlantic IRD record at Site 983: High and variable IRD input characterizes the LGM and T1, following by decreasing IRD through the deglacial paralleling the northward movement of the PF. During the LGM, an IRD peak at Site 983 occurs at ~25 000 yr BP. At the Eirik Drift site, two large peaks occur approximately during the same time interval; centered at ~24 300 (and ~22 000) yr BP. The differences in timings of these events might be due to the different age model approaches used for MD03-2665 and ODP Site 983 (Barker et al., 2015). The ~24 300 yr BP peak at the Eirik Drift and the ~25 000 yr BP peak at ODP Site 983 could represent the same calving event, although the independent age models make this difficult to confirm. The ~24 300 yr BP event at the Eirik Drift is similar in timing as the H2 (Hemming, 2004), but no significant amount of detrital carbonate was found in the samples, similar to other sites north of the main IRD belt (Hodell et al., 2010). During the end of the LGM, both core sites receive high IRD input. At Site 983, there appears to be higher amounts of IRD grains/gram during the time interval ~20 000 to ~17 500 yr BP, versus the Eirik Drift IRD %, but this can be an artefact of the 4 cm sample spacing as indicated above. Also, keep in mind that both IRD % and IRD/gram are indexes of lithic grains from melting icebergs that are transported with the prevailing surface ocean currents. And that the availability of icebergs that carry sediments determines the amount of IRD deposition and might vary from core site to core site. Also, the main source region for IRD at the Eirik Drift is Greenland provinces (Carlson et al., 2008; Colville et al., 2011; Hatfield et al., 2016; Griem, 2021) while the IRD grains at the Gardar Drift is a combination of basaltic-rich Icelandic sediments with additional sedimentary rock fragments from Fennoscandia, Laurentide and Greenland (Hodell et al., 2010). Hence, several ice sheets are contributing to

iceberg flux, but not necessarily simultaneous nor with equal amounts of grains. Moving into HS1, both drift records show a peak of IRD centered at ~16 500 yr BP corresponding to the timing of the H1 event (Hemming, 2004).

Into the B/A, both sites still exhibit some IRD input that gradually tapers off towards the transition into the early Holocene period. The *N. pachyderma* % at Site 983 during the B/A decreases from ~75% to ~50% towards the end of the period, indicating a temperature increase in the surface waters in central subpolar North Atlantic, while the Eirik Drift *N. pachyderma* % only decreases down to ~95%, indicating prevailing cold conditions in the northwestern North Atlantic. However, the different age models should be taken into consideration when correlating the timing of the *N. pachyderma* % decreases.

During the early Holocene, the IRD records for Site 983 and the Eirik Drift exhibit similar patterns. In both records, IRD is drastically reduced after the end of the YD to near-zero by ~11 000 yr BP. Into the early Holocene, only minor IRD is observed, most prominently the minor peak at ~10 300 yr BP in the Eirik Drift record and small occurrences of IRD between ~11 000 yr BP and ~10 000 yr BP at Site 983.

The similarity between large IRD events in the Eirik Drift and Gardar Drift cores and H-events 1 and 2 suggests a possible connection. Both sites lie outside the main IRD belt and lack significant detrital carbonate suggesting that both Laurentide (main IRD belt) and other ice sheets (e.g., GIS, Icelandic, Fennoscandia) may all be increasing iceberg calving during the H-events 1 and 2. However, at these sites north of the main IRD belt, non-Heinrich timed IRD peaks also occur suggesting major episodes of ice rafting are not restricted to H-events. Hemming (2004) noted previously that IRD peaks are more common in the northern North Atlantic than in the IRD belt further south, but we show here that many of these events are approximately coeval between the Labrador Sea and south of Iceland. This points to coherent widespread cooling events allowing greater iceberg survival and transport south and/or a coherent increase in calving from multiple sources (different ice sheets). It is notable that there is no decrease in SST locally to support the transport mechanism, at least at the Eirik Drift, pointing toward multiple ice sheets calving during some of the largest IRD events. Changes in the overturning circulation in the North Atlantic (AMOC) have been proposed by Marcott et al. (2011) as one possible process that might both drive and explain the observed synchronic occurrence of IRD in the North Atlantic region. According to Marcott et al. (2011), reduced

AMOC prior to H-events both increased sea level and subsurface ocean warming, which again increased the basal melt rate under the ice shelfs resulting in widespread ice-shelf loss and hence widespread coherent events since AMOC would act as a common forcing mechanism.

8 Summary of Conclusions

New high-resolution multiproxy records from Core MD03-2665 south off Greenland, document the progression and variability in climate, surface ocean hydrology and Greenland Ice Sheet activity during the last deglacial interval and into the early Holocene interglacial (25 000–9 000 yr BP).

- The gradual warming trend through the last deglaciation is interrupted by abrupt and brief warming and cooling episodes associated with the B/A warming and the Younger Dryas (YD) cold event, respectively. All proxy records exhibit high frequency variability spanning the early Holocene part of the record, with a particularly prominent and abrupt cooling event centered at 10 000 yr BP.

- During the early part of the deglacial period there is evidence for temperature, meltwater, and sea level influencing the planktic $\delta^{18}O$ signal, while coeval changes in foraminiferal assemblage and geochemistry register the YD cooling. Following the YD, changes in foraminiferal assemblage and geochemistry continue to decrease indicating a warming (or freshening) of the near-surface waters. Superimposed on late deglacial-Holocene warming are rapid oscillations in near surface conditions.

- Foraminiferal assemblage counts trace the surface ocean conditions and the positions of oceanic fronts over the deglacial. The abundance of polar species *N. pachyderma* indicates that the PF remained south of the core site during the LGM and H1. Comparison with foraminiferal assemblage data from the Feni Drift and the Gardar Drift in the eastern and central North Atlantic, indicate that the AF was fluctuating between Site 980 and 983, respectively, through the last deglaciation, whereas temperate species associated with warm Atlantic water document that the AF finally moved north of the Eirik Drift in the early Holocene. Distinct oscillations in assemblages document that the notable cooling at 10 000 yr BP led to rapid southward movement of oceanic fronts. High abundance of subpolar and transitional species during the early Holocene indicate that the AF was most likely further north than today, and that the Eirik Drift was bathed by Atlantic water.

- Comparison of the subpolar gyre changes and GIS activity at the Eirik Drift with records of GIS ablation and discharge (Precambrian Greenland silt % and Silt provenance %) exhibits a similar trend over the last deglacial, documenting waxing and waning of the GIS.

- The IRD record covering the last deglacial reveals large fluctuations of iceberg calving from the northern North Atlantic ice sheets (Greenland, Icelandic, Fennoscandia). Major IRD events at the Eirik Drift occur approximately coevally with H-events 1 and 2, but large IRD peaks also occur during the deglacial, demonstrating that transport of lithic grains to the site was not restricted only to intervals corresponding to Heinrich events. The record indicates that the Greenland Ice Sheet was continuously calving during the deglacial, and only ceased calving once the ice sheet had retreated off the continental shelf in the beginning of the early Holocene.

- The *N. pachyderma* $\delta^{18}O$ record follows similar trends as other isotopic records from the North Atlantic (NGRIP, GRIP, DYE-3 ice cores and MD99-2227 sediment core) indicating that the local climate was like the broader North Atlantic climate. The rapid cooling event seen at 10 000 yr BP during the early Holocene could be a result of freshwater outbursts reducing deep water ventilation as for the 8.2 event, but more detailed analyses would be necessary to confirm the exact cause.

Bibliography

Alonso-Garcia, M., Sierro, F. J., & Flores, J. A. (2011). Arctic front shifts in the subpolar North Atlantic during the Mid-Pleistocene (800–400 ka) and their implications for ocean circulation. *Palaeogeography, Palaeoclimatology, Palaeoecology*, *311*(3-4), 268-280.

Andrews, J. T., Smith, L. M., Preston, R., Cooper, T., & Jennings, A. E. (1997). Spatial and temporal patterns of iceberg rafting (IRD) along the East Greenland margin, ca. 68°N, over the last 14 cal.ka. *Journal of Quaternary Science*, *12*(1), 1-13.

Andrews, J. T. (2000). Icebergs and iceberg rafted detrius (IRD) in the North Atlantic: facts and assumptions. *Oceanography*, *13*(3), 100-108.

Armstrong, H., & Brasier, M. (2005). *Microfossils* (Second ed.). John Wiley & Sons, Incorporated.

Arthur, M. A., Srivastava, S. P., Kaminski, M., Jarrad, R., & Osler, J. (1989). Seismic stratigraphy and history of deep circulation and sediment drift development in Baffin Bay and the Labrador Sea. *Proceedings of the Ocean Drilling Program, Scientific Results*, *105*, 957-988.

Ascough, P. L., Cook, G. T., Dugmore, A. J., Barber, J., Higney, E., & Scott, E. M. (2004). Holocene Variations in the Scottish Marine Radiocarbon Reservoir Effect. *Radiocarbon*, *46*(2), 611-620.

Ascough, P. L., Cook, G. T., & Dugmore, A. J. (2005). Methodological approaches to determining the marine radiocarbon reservoir effect. *Progress in Physical Geography*, *29*(4), 532-547.

Bard, E., Arnold, M., Mangerud, J., Paterne, M., Labeyrie, L., Duprat, J., Mélières, M.-A., Sønstegaard, E., & Duplessy, J.-C. (1994). The North Atlantic atmosphere-sea surface 14C gradient during the Younger Dryas climatic event. *Earth and Planetary Science Letters*, *126*, 275-287.

Barker, S., Chen, J., Gong, X., Jonkers, L., Knorr, G., & Thornalley, D. (2015). Icebergs not the trigger for North Atlantic cold events. *Nature*, *520*(7547), 333-336.

Barker, S. (2021). *Planktic foraminiferal and Ice Rafted Debris (IRD) counts from ODP Site 983* PANGAEA. https://doi.org/10.1594/PANGAEA.929721

Bé, A. H. W., & Tolderlund, D. S. (1971). Distribution and ecology of living planktonic foraminifera in surface waters of the Atlantic and Indian Oceans. In B. M. Funnell & W. R. Riedel (Eds.), *The Micropalaeontology of Oceans* (pp. 105-150). Cambridge University Press.

Bender, M. L. (2013). *Paleoclimate*. Princeton University Press.

Bennike, O. (2002). Late Quaternary history of Washington Land, North Greenland. *Boreas*, *31*(3), 260-272.

Bennike, O., & Björck, S. (2002). Chronology of the last recession of the Greenland Ice Sheet. *Journal of Quaternary Science*, *17*(3), 211-219.

Benway, H. M., McManus, J. F., Oppo, D. W., & Cullen, J. L. (2010). Hydrographic changes in the eastern subpolar North Atlantic during the last deglaciation. *Quaternary Science Reviews*, *29*(23-24), 3336-3345.

Bigg, G. R., & Rohling, E. J. (2000). An oxygen isotope data set for marine waters. *Journal of Geophysical Research: Oceans*, *105*(C4), 8527-8535.

Bijma, J., Faber, W. W., & Hemleben, C. (1990). Temperature and salinity limits for growth and survival of some planktonic foraminifers in laboratory cultures. *Journal of Foraminiferal Reasearch*, *20*(2), 95-116.

Blaauw, M., & Christen, J. A. (2011). Flexible paleoclimate age-depth models using an autoregressive gamma process. *Bayesian Analysis*, *6*(3).

Blaauw, M., & Christen, J. A. (2013). *Bacon manual - v2.3.9.1*. Retrieved 06.09.2022 from http://www.chrono.qub.ac.uk/blaauw/bacon.html

Boltwood, B. B. (1906). Note on the Production of Radium by Actinium. *American Journal of Science*, *22*(132), 537-538.

Bond, G. C., Heinrich, H., Broecker, W., Labeyrie, L., McManus, J. F., Andrews, J., Huon, S., Jantschik, R., Clasen, S., Simet, C., Tedesco, K., Klas, M., Bonani, G., & Ivy, S. (1992). Evidence for massive discharges of icebergs into the North Atlantic ocean during the last glacial period. *Nature*, *360*(6401), 245-249.

Bond, G. C., & Lotti, R. (1995). Iceberg discharges into the North Atlantic on millennial time scales during the last glaciation. *Science*, *267*(5200), 1005-1010.

Bond, G. C., Kromer, B., Beer, J., Muscheler, R., Evans, M. N., Showers, W., Hoffmann, S., Lotti-Bond, R., Hajdas, I., & Bonani, G. (2001). Persistent Solar Influence on North Atlantic Climate During the Holocene. *Science*, *294*(5549), 2130-2136.

Boudagher-Fadel, M. K. (2015). *Biostratigraphic and Geological Significance of Planktonic Foraminifera* (Updated 2n ed.). UCL Press.

Broecker, W., Andree, M., Wolfli, W., Oeschger, H., Bonani, G., Kennett, J., & Peteet, D. (1988). The chronology of the last Deglaciation: Implications to the cause of the Younger Dryas Event. *Paleoceanography*, *3*(1), 1-19.

Broecker, W., & Denton, G. H. (1990). The role of ocean-atmosphere reorganizations in glacial cycles. *Quaternary Science Reviews*, *9*(4), 305-341.

Broecker, W., Bond, G. C., Klas, M., Clark, E., & McManus, J. (1992). Origin of the northern Atlantic's Heinrich events. *Climate Dynamics*, *6*(3), 265-273.

Broecker, W. S. (2006). Was the Younger Dryas Triggered by a Flood? *Science*, *312*(5777), 1146-1148.

Butzin, M., Prange, M., & Lohmann, G. (2005). Radiocarbon simulations for the glacial ocean: The effects of wind stress, Southern Ocean sea ice and Heinrich events. *Earth and Planetary Science Letters*, *235*(1-2), 45-61.

Butzin, M., Heaton, T. J., Köhler, P., & Lohmann, G. (2020). A Short Note on Marine Reservoir Age Simulations Used in IntCal20. *Radiocarbon*, *62*(4), 865-871.

Carlson, A. E., Clark, P. U., Haley, B. A., Klinkhammer, G. P., Simmons, K., Brook, E. J., & Meissner, K. J. (2007). Geochemical proxies of North American freshwater routing during the Younger Dryas cold event. *Proceedings of the National Academy of Sciences of the United States of America*, *104*(16), 6556-6561.

Carlson, A. E., Stoner, J. S., Donnelly, J. P., & Hillaire-Marcel, C. (2008). Response of the southern Greenland Ice Sheet during the last two deglaciations. *Geology*, *36*(5).

Carlson, A. E., & Winsor, K. (2012). Northern Hemisphere ice-sheet responses to past climate warming. *Nature Geoscience*, *5*(9), 607-613.

Carstens, J., Hebbeln, D., & Wefer, G. (1997). Distribution of planktic foraminifera at the ice margin in the Arctic (Fram Strait). *Marine Micropaleontology*, *29*(3-4), 257-269.

Chapman, M. R. (2010). Seasonal production patterns of planktonic foraminifera in the NE Atlantic Ocean: Implications for paleotemperature and hydrographic reconstructions. *Paleoceanography*, *25*(1).

Clark, P. U., Marshall, S. J., Clarke, G. K. C., Hostetler, S. W., Licciardi, J. M., & Teller, J. T. (2001). Freshwater Forcing of Abrupt Climate Change During the Last Glaciation. *Science*, *293*(5528), 283-287.

Clark, P. U., Pisias, N. G., Stocker, T. F., & Weaver, A. J. (2002). The role of the thermohaline circulation in abrupt climate change. *Nature*, *415*, 863-869.

Clarke, G. K. C., Leverington, D., Teller, J. T., & Dyke, A. (2003). Superlakes, Megafloods, and Abrupt Climate Change. *Science*, *301*(5635), 922-923.

Colville, E. J., Carlson, A. E., Beard, B. L., Hatfield, R. G., Stoner, J. S., Reyes, A. V., & Ullman, D. J. (2011). Sr-Nd-Pb isotope evidence for ice-sheet presence on southern Greenland during the Last Interglacial. *Science*, *333*(6042), 620-623.

Cronin, T. M. (2010). *Paleoclimates: understanding climate change past and present*. Columbia University Press.

Darling, K. F., Wade, C. M., Stewart, I. A., Kroon, D., Dingle, R., & Leigh Brown, A. J. (2000). Molecular evidence for genetic mixing of Arctic and Antarctic subpolar populations of planktonic foraminifers. *Nature*, *405*(6782), 43-47.

Darling, K. F., Kučera, M., Wade, C. M., von Langen, P., & Pak, D. (2003). Seasonal distribution of genetic types of planktonic foraminifer morphospecies in the Santa

Barbara Channel and its paleoceanographic implications. *Paleoceanography*, *18*(2), 1-11.

Darling, K. F., Kučera, M., Kroon, D., & Wade, C. M. (2006). A resolution for the coiling direction paradox in Neogloboquadrina pachyderma. *Paleoceanography*, *21*(2), 1-14.

Davies, S., Stow, D. A. V., & Nicholson, U. (2021). Late glacial to holocene sedimentary facies of the Eirik Drift, southern Greenland margin: Spatial and temporal variability and paleoceanographic implications. *Marine Geology*, *440*.

Deschamps, P., Durand, N., Bard, E., Hamelin, B., Camoin, G., Thomas, A. L., Henderson, G. M., Okuno, J., & Yokoyama, Y. (2012). Ice-sheet collapse and sea-level rise at the Bolling warming 14,600 years ago. *Nature*, *483*(7391), 559-564.

Dickson, R. R., & Brown, J. (1994). The production of North Atlantic Deep Water: Sources, rates, and pathways. *Journal of Geophysical Research*, *99*(C6).

Dickson, R. R. (1995). The Natural History of Time Series. In T. M. Powell & J. H. Steele (Eds.), *Ecological Time Series* (pp. 70-98). Springer US.

Dowdeswell, J. A. (1986). The Distribution and Character of Sediments in a Tidewater Glacier, Southern Baffin Island, N.W.T., Canada. *Arctic and Alpine Research*, *18*(1), 45-56.

Elliot, M., Labeyrie, L., Bond, G. C., Cortijo, E., Turon, J.-L., Tisnerat, N., & Duplessy, J.-C. (1998). Millennial-scale iceberg discharges in the Irminger Basin during the Last Glacial Period: Relationship with the Heinrich events and environmental settings. *Paleoceanography*, *13*(5), 433-446.

Epstein, S. A., Buchsbaum, R. M., Lowenstam, H. A., & Urey, H. C. (1953). Revised Carbonate-water Isotopic Temperature Scale. *Geological Society of America Bulletin*, *64*(11), 1315-1326.

Eynaud, F., de Abreu, L., Voelker, A., Schönfeld, J., Salgueiro, E., Turon, J.-L., Penaud, A., Toucanne, S., Naughton, F., Sánchez Goñi, M. F., Malaizé, B., & Cacho, I. (2009). Position of the Polar Front along the western Iberian margin during key cold episodes of the last 45 ka. *Geochemistry, Geophysics, Geosystems*, *10*(7), 1-21.

Fairbanks, R. G. (1989). A 17,000-year glacio-eustatic sea level record: influence of glacial melting rates on the Younger Dryas event and deep-ocean circulation. *Nature*, *342*.

Faugères, J.-C., Stow, D. A. V., Imbert, P., & Viana, A. R. (1999). Seismic features diagnostic of contourite drifts. *Marine Geology*, *162*, 1-38.

Fleming, K., Johnston, P., Zwartz, D., Yokoyama, Y., Lambeck, K., & Chappell, J. (1998). Refining the eustatic sea-level curve since the Last Glacial Maximum using far- and intermediate-field sites. *Earth and Planetary Science Letters*, *163*, 327-342.

Galaasen, E. V., Ninnemann, U. S., Irvali, N., Kleiven, H. F., Rosenthal, Y., Kissel, C., & Hodell, D. A. (2014). Rapid Reductions in North Atlantic Deep Water During the Peak of the Last Interglacial Period. *343*(March), 1129-1132.

Galaasen, E. V., Ninnemann, U. S., Kessler, A., Irvali, N., Rosenthal, Y., Tjiputra, J., Bouttes, N., Roche, D. M., Kleiven, H. F., & Hodell, D. A. (2020). Interglacial instability of North Atlantic Deep Water ventilation. *Science*, *367*(6485), 1485-1489.

Godwin, H. (1962). Half-life of Radiocarbon. *Nature*, *195*(4845), 984-984.

Griem, L. (2021). *Ocean circulation changes off southern Greenland during the abrupt climate events of mid-to-late MIS3* [Doctoral dissertation, University of Bergen].

Hajdas, I. (2008). Radiocarbon dating and its applications in Quaternary studies. *Quaternary Science Journal*, *57*(1-2), 2-24.

Hansen, B., & Østerhus, S. (2000). North Atlantic-Nordic Seas exchanges. *Progress in Oceanography*, *45*(2), 109-208.

Hatfield, R. G., Reyes, A. V., Stoner, J. S., Carlson, A. E., Beard, B. L., Winsor, K., & Welke, B. (2016). Interglacial responses of the southern Greenland ice sheet over the last 430,000 years determined using particle-size specific magnetic and isotopic tracers. *Earth and Planetary Science Letters*, *454*, 225-236.

Heaton, T. J., Köhler, P., Butzin, M., Bard, E., Reimer, R. W., Austin, W. E. N., Bronk Ramsey, C., Grootes, P. M., Hughen, K. A., Kromer, B., Reimer, P. J., Adkins, J., Burke, A., Cook, M. S., Olsen, J., & Skinner, L. C. (2020). Marine20—The Marine Radiocarbon Age Calibration Curve (0–55,000 cal BP). *Radiocarbon*, *62*(4), 779-820.

Heezen, B. C., Hollister, C. D., & Ruddiman, W. F. (1966). Shaping of the Continental Rise by Deep Geostrophic Contour Currents. *Science*, *152*, 502-508.

Heinrich, H. (1988). Origin and consequences of cyclic ice rafting in the Northeast Atlantic Ocean during the past 130,000 years. *Quaternary Research*, *29*(2), 142-152.

Hemleben, C., Spindler, M., & Anderson, O. R. (1989). Taxonomy and Species Features. In *Modern Planktonic Foraminifera* (pp. 8-32). Springer New York.

Hemming, S. R. (2004). Heinrich events: Massive late Pleistocene detritus layers of the North Atlantic and their global climate imprint. *Reviews of Geophysics*, *42*(1).

Hillaire-Marcel, C., de Vernal, A., Bilodeau, G., & Wu, G. (1994). Isotope stratigraphy, sedimentation rates, deep circulation, and carbonate events in the Labrador Sea during the last ~200 ka. *Canadian Journal of Earth Sciences*, *31*, 63-89.

Hodell, D. A., Evans, H. F., Channell, J. E. T., & Curtis, J. H. (2010). Phase relationships of North Atlantic ice-rafted debris and surface-deep climate proxies during the last glacial period. *Quaternary Science Reviews*, *29*(27-28), 3875-3886.

Hunter, S., Wilkinson, D., Louarn, E., Nick McCave, I., Rohling, E., Stow, D. A. V., & Bacon, S. (2007). Deep western boundary current dynamics and associated sedimentation on the Eirik Drift, Southern Greenland Margin. *Deep Sea Research Part I: Oceanographic Research Papers*, *54*(12), 2036-2066.

Husum, K., & Hald, M. (2012). Arctic planktic foraminiferal assemblages: Implications for subsurface temperature reconstructions. *Marine Micropaleontology*, *96-97*, 38-47.

Irvali, N., Ninnemann, U. S., Galaasen, E. V., Rosenthal, Y., Kroon, D., Oppo, D. W., Kleiven, H. F., Darling, K. F., & Kissel, C. (2012). Rapid switches in subpolar North Atlantic hydrography and climate during the Last Interglacial (MIS 5e). *Paleoceanography*, *27*(2), 1-16.

Irvali, N., Ninnemann, U. S., Kleiven, H. K. F., Galaasen, E. V., Morley, A., & Rosenthal, Y. (2016). Evidence for regional cooling, frontal advances, and East Greenland Ice Sheet changes during the demise of the last interglacial. *Quaternary Science Reviews*, *150*, 184-199.

Irvali, N., Galaasen, E. V., Ninnemann, U. S., Rosenthal, Y., Born, A., & Kleiven, H. K. F. (2020). A low climate threshold for south Greenland Ice Sheet demise during the Late Pleistocene. *Proceedings of the National Academy of Sciences of the United States of America*, *117*(1), 190-195.

Iselin, C. O. D. (1936). A study of the circulation of the western North Atlantic. *Papers in Physical Oceanography and Meteorology*, *4*(4), 1-101.

Jennings, A. E., Hald, M., Smith, M., & Andrews, J. T. (2006). Freshwater forcing from the Greenland Ice Sheet during the Younger Dryas: evidence from southeastern Greenland shelf cores. *Quaternary Science Reviews*, *25*(3-4), 282-298.

Johannessen, T., Jansen, E., Flatøy, A., & Ravelo, A. C. (1994). The Relationship between Surface Water Masses, Oceanographic Fronts and Paleoclimatic Proxies in Surface Sediments of the Greenland, Iceland, Norwegian Seas. In R. Zahn, T. F. Pedersen, M. A. Kaminski, & L. Labeyrie (Eds.), *Carbon Cycling in the Glacial Ocean: Constraints on the Ocean's Role in Global Change* (Vol. 17, pp. 61-85). Springer Berlin Heidelberg.

Jones, E. J. W., Ewing, M., Ewing, J. I., & Eittreim, S. L. (1970). Influences of Norwegian Sea overflow water on sedimentation in the northern North Atlantic and Labrador Sea. *Journal of Geophysical Research*, *75*(9), 1655-1680.

Jonkers, L., Brummer, G. J. A., Peeters, F. J. C., Van Aken, H. M., & De Jong, M. F. (2010). Seasonal stratification, shell flux, and oxygen isotope dynamics of leftcoiling N. pachyderma and T. quinqueloba in the western subpolar North Atlantic. *Paleoceanography*, *25*(2), 1-13.

Keigwin, L. D., Jones, G. A., Lehman, S. J., & Boyle, E. A. (1991). Deglacial Meltwater Discharge, North Atlantic Deep Circulation, and Abrupt Climate Change. *Journal of Geophysical Research*, *96*(C9), 16811-16826.

Kleiven, H. F., Kissel, C., Laj, C., Ninnemann, U. S., Richter, T. O., & Cortijo, E. (2008). Reduced North Atlantic deep water coeval with the glacial lake agassiz freshwater outburst. *Science*, *319*(5859), 60-64.

Knutz, P. C., Sicre, M. A., Ebbesen, H., Christiansen, S., & Kuijpers, A. (2011). Multiple-stage deglacial retreat of the southern Greenland Ice Sheet linked with Irminger Current warm water transport. *Paleoceanography*, *26*(3), 1-18.

Kohfeld, K. E., Fairbanks, R. G., Smith, S. L., & Walsh, I. D. (1996). Neogloboquadrina pachyderma (sinistral coiling) as paleoceanographic tracers in polar oceans: Evidence

from Northeast Water Polynya plankton tows, sediment traps, and surface sediments. *Paleoceanography*, *11*(6), 679-699.

Kroon, D., & Ganssen, G. (1989). Northern Indian Ocean upwelling cells and the stable isotope composition of living planktonic foraminifers. *Deep-Sea Research*, *36*(8), 1219-1236.

Kučera, M., Weinelt, M., Kiefer, T., Pflaumann, U., Hayes, A., Weinelt, M., Chen, M.-T., Mix, A. C., Barrows, T. T., Cortijo, E., Duprat, J. M., Juggins, S., & Waelbroeck, C. (2005a). *Compilation of planktic foraminifera census data, modern from the Atlantic Ocean* [Dataset]. PANGAEA. https://doi.org/10.1594/PANGAEA.227322

Kučera, M., Weinelt, M., Kiefer, T., Pflaumann, U., Hayes, A., Weinelt, M., Chen, M.-T., Mix, A. C., Barrows, T. T., Cortijo, E., Duprat, J. M., Juggins, S., & Waelbroeck, C. (2005b). *Compilation of planktic Foraminifera census data, LGM from the Atlantic Ocean* [Dataset]. PANGAEA. https://doi.org/10.1594/PANGAEA.227329

Kučera, M., Weinelt, M., Kiefer, T., Pflaumann, U., Hayes, A., Weinelt, M., Chen, M. T., Mix, A. C., Barrows, T. T., Cortijo, E., Duprat, J., Juggins, S., & Waelbroeck, C. (2005c). Reconstruction of sea-surface temperatures from assemblages of planktonic foraminifera: Multi-technique approach based on geographically constrained calibration data sets and its application to glacial Atlantic and Pacific Oceans. *Quaternary Science Reviews*, *24*(7-9), 951-998.

Kučera, M. (2007). Chapter Six Planktonic Foraminifera as Tracers of Past Oceanic Environments. In C. Hillaire-Marcel & A. de Vernal (Eds.), *Developments in Marine Geology* (Vol. 1, pp. 213-262). Elsevier B.V.

Lam, A. R., & Leckie, M. R. (2020). Late Neogene and Quaternary diversity and taxonomy of subtropical to temperate planktic foraminifera across the Kuroshio Current Extension, northwest Pacific Ocean. *Micropaleontology*, *66*(3), 177-268.

Lambeck, K., Rouby, H., Purcell, A., Sun, Y., & Sambridge, M. (2014). Sea level and global ice volumes from the Last Glacial Maximum to the Holocene. *Proceedings of the National Academy of Sciences of the United States of America*, *111*(43), 15296-15303.

Linick, T. W., Damon, P. E., Donahue, D. J., & Jull, A. J. T. (1989). Accelerator mass spectrometry: The new revolution in radiocarbon dating. *Quaternary International*, *1*, 1-6.

Lončarić, N., Peeters, F. J. C., Kroon, D., & Brummer, G. J. A. (2006). Oxygen isotope ecology of recent planktic foraminifera at the central Walvis Ridge (SE Atlantic). *Paleoceanography*, *21*(3), 1-18.

Lowe, J. J., & Walker, M. (2015). *Reconstructing Quaternary Environments* (3 ed.). Routledge.

MacAyeal, D. R. (1993). Binge/purge oscillations of the Laurentide ice sheet as a cause of the North Atlantic's Heinrich events. *Paleoceanography*, *8*(6), 775-784.

Mangerud, J. (1972). Radiocarbon dating of marine shells, including a discussion of apparent age of Recent shells from Norway. *Boreas*, *1*(2), 143-172.

Marcott, S. A., Clark, P. U., Padman, L., Klinkhammer, G. P., Springer, S. R., Liu, Z., Otto-Bliesner, B. L., Carlson, A. E., Ungerer, A., Padman, J., He, F., Cheng, J., & Schmittner, A. (2011). Ice-shelf collapse from subsurface warming as a trigger for Heinrich events. *Proceedings of the National Academy of Sciences of the United States of America*, *108*(33), 13415-13419.

Max, L., Nurnberg, D., Chiessi, C. M., Lenz, M. M., & Mulitza, S. (2022). Subsurface ocean warming preceded Heinrich Events. *Nature Communications*, *13*(1), 4217.

McCartney, M. S. (1992). Recirculating components to the deep boundary current of the northern North Atlantic. *Progress in Oceanography*, *29*(4), 283-383.

McManus, J. F., Francois, R., Gherardi, J.-M., Keigwin, L. D., & Brown-Leger, S. (2004). Collapse and rapid resumption of Atlantic meridional circulation linked to deglacial climate changes. *Nature*, *428*, 834-837.

Mokeddem, Z., McManus, J. F., & Oppo, D. W. (2014). Oceanographic dynamics and the end of the last interglacial in the subpolar North Atlantic. *Proceedings of the National Academy of Sciences of the United States of America*, *111*(31), 11263-11268.

Morey, A. E., Mix, A. C., & Pisias, N. G. (2005). Planktonic foraminiferal assemblages preserved in surface sediments correspond to multiple environment variables. *Quaternary Science Reviews*, *24*(7-9), 925-950.

Ng, H. C., Robinson, L. F., McManus, J. F., Mohamed, K. J., Jacobel, A. W., Ivanovic, R. F., Gregoire, L. J., & Chen, T. (2018). Coherent deglacial changes in western Atlantic Ocean circulation. *Nature Communications*, *9*(1), 1-10.

NGRIP members. (2004). High-resolution record of Northern Hemisphere climate extending into the last interglacial period. *Nature*, *431*(7005), 147-151.

Orsi, A. H., Johnson, G. C., & Bullister, J. L. (1999). Circulation, mixing, and production of Antarctic Bottom Water. *Progress in Oceanography*, *43*, 55-109.

PALSEA members. (2010). The sea-level conundrum: case studies from palaeo-archives. *Journal of Quaternary Science*, *25*(1), 19-25.

Parker, A. G., Goudie, A. S., Stokes, S., White, K., Hodson, M. J., Manning, M., & Kennet, D. (2006). A Record of Holocene Climate Change from Lake Geochemical Analyses in Southeastern Arabia. *Quaternary Research*, *66*(3), 465-476.

Pearson, P. N., & Kučera, M. (2018). Taxonomy, biostratigraphy, and phylogeny of Oligocene Turborotalia. In *Atlas of Oligocene Planktonic Foraminifera* (Vol. 46, pp. 385-392): Cushman Foundation of Foraminiferal Research, Special Publication.

Peltier, W. R., & Fairbanks, R. G. (2006). Global glacial ice volume and Last Glacial Maximum duration from an extended Barbados sea level record. *Quaternary Science Reviews*, *25*(23-24), 3322-3337.

Pickart, R. S., McKee, T. K., Torres, D. J., & Harrington, S. A. (1999). Mean Structure and Interannual Variability of the Slopewater System South of Newfoundland. *Journal of Physical Oceanography*, *29*(10), 2541-2558.

Pickart, R. S., Spall, M. A., Ribergaard, M. H., Moore, G. W. K., & Milliff, R. F. (2003). Deep convection in the Irminger Sea forced by the Greenland tip jet. *Nature*, *424*, 152-156.

Pinet, P. R. (2016). *Invitation to Oceanography* (7th ed.). Jones & Bartlett.

Rahmstorf, S. (2002). Ocean circulation and climate during the past 120,000 years. *Nature*, *419*(6903), 207-214.

Rahmstorf, S. (2006). Thermohaline Ocean Circulation. In S. A. Elias (Ed.), *Encyclopedia of Quaternary Sciences* (pp. 1-10). Elsevier.

Rasmussen, S. O., Vinther, B. M., Clausen, H. B., & Andersen, K. K. (2007). Early Holocene climate oscillations recorded in three Greenland ice cores. *Quaternary Science Reviews*, *26*(15-16), 1907-1914.

Rasmussen, S. O., Bigler, M., Blockley, S. P., Blunier, T., Buchardt, S. L., Clausen, H. B., Cvijanovic, I., Dahl-Jensen, D., Johnsen, S. J., Fischer, H., Gkinis, V., Guillevic, M., Hoek, W. Z., Lowe, J. J., Pedro, J. B., Popp, T., Seierstad, I. K., Steffensen, J. P., Svensson, A. M., . . . Winstrup, M. (2014). A stratigraphic framework for abrupt climatic changes during the Last Glacial period based on three synchronized Greenland ice-core records: refining and extending the INTIMATE event stratigraphy. *Quaternary Science Reviews*, *106*, 14-28.

Reimer, P. J., Austin, W. E. N., Bard, E., Bayliss, A., Blackwell, P. G., Bronk Ramsey, C., Butzin, M., Cheng, H., Edwards, R. L., Friedrich, M., Grootes, P. M., Guilderson, T. P., Hajdas, I., Heaton, T. J., Hogg, A. G., Hughen, K. A., Kromer, B., Manning, S. W., Muscheler, R., . . . Talamo, S. (2020). The IntCal20 Northern Hemisphere Radiocarbon Age Calibration Curve (0–55 cal kBP). *Radiocarbon*, *62*(4), 725-757.

Reyes, A. V., Carlson, A. E., Beard, B. L., Hatfield, R. G., Stoner, J. S., Winsor, K., Welke, B., & Ullman, D. J. (2014). South Greenland ice-sheet collapse during Marine Isotope Stage 11. *Nature*, *510*(7506), 525-528.

Reynolds, L., & Thunell, R. C. (1985). Seasonal succession of planktonic foraminifera in the subpolar North Pacific. *Journal of Foraminiferal Reasearch*, *15*(4), 282-301.

Ruddiman, W. F. (1977). Late Quaternary deposition of ice-rafted sand in the subpolar North Atlantic (lat 40° to 65°N). *Geological Society of America Bulletin*, *88*(12), 1813-1827.

Ruddiman, W. F. (2014). *Earth's Climate: Past and Future* (3 ed.). W. H. Freeman and Company.

Rudels, B. (2002). The East Greenland Current and its contribution to the Denmark Strait overflow. *ICES Journal of Marine Science*, *59*(6), 1133-1154.

Rutledal, S. (2017). *Assessing linkages between ice sheet calving, subpolar gyre hydrography and deep water ventilation during the last deglaciation* [Master's thesis, University of Bergen].

Rørvik, K. L., Laberg, J. S., Hald, M., Ravna, E. K., & Vorren, T. O. (2010). Behavior of the northwestern part of the Fennoscandian Ice Sheet during the Last Glacial Maximum – a response to external forcing. *Quaternary Science Reviews*, *29*(17-18), 2224-2237.

Sahoo, N., Saalim, S. M., Matul, A., Mohan, R., Tikhonova, A., & Kozina, N. (2022). Planktic Foraminiferal Assemblages in Surface Sediments From the Subpolar North Atlantic Ocean. *Frontiers in Marine Science*, *8*, 1-19.

Schiebel, R., Bijma, J., & Hemleben, C. (1997). Population dynamics of the planktic foraminifer Globigerina bulloides from the eastern North Atlantic. *Deep-Sea Research*, *44*(9-10), 1701-1713j.

Schiebel, R., & Hemleben, C. (2017). *Planktic Foraminifers in the Modern Ocean* (2 ed.). Springer Nature.

Schmidt, G. A. (1999). Forward modeling of carbonate proxy data from planktonic foraminifera using oxygen isotope tracers in a global ocean model. *Paleoceanography*, *14*(4), 482-497.

Schmidt, G. A., Bigg, G. R., & Rohling, E. J. (1999). *Global Seawater Oxygen-18 Database - v1.22*. Retrieved 7.3.2023 from https://data.giss.nasa.gov/o18data/

Screen, J. A., & Simmonds, I. (2010). The central role of diminishing sea ice in recent Arctic temperature amplification. *Nature*, *464*(7293), 1334-1337.

Shipboard Scientific Party. (2003). *MD132—P.I.C.A.S.S.O. IMAGES XI Cruise Report* (2910180336). https://epic.awi.de/id/eprint/34710/

Simstich, J., Sarnthein, M., & Erlenkeuser, H. (2003). Paired δ18O signals of Neogloboquadrina pachyderma (s) and Turborotalita quinqueloba show thermal stratification structure in Nordic Seas. *Marine Micropaleontology 48*(1-2), 107-125.

Skinner, L. C., Muschitiello, F., & Scrivner, A. E. (2019). Marine Reservoir Age Variability Over the Last Deglaciation: Implications for Marine CarbonCycling and Prospects for Regional Radiocarbon Calibrations. *Paleoceanography and Paleoclimatology*, *34*(11), 1807-1815.

Smith, W. H. F., & Sandwell, D. T. (1997). Global Sea Floor Topography from Satellite Altimetry and Ship Depth Soundings. *Science*, *277*, 1956-1962.

Spindler, M., & Dieckmann, G. S. (1986). Distribution and abundance of the planktic foraminifer Neogloboquadrina pachyderma in sea ice of the Weddell Sea (Antarctica). *Polar Biology*, *5*(3), 185-191.

Stanford, J. D., Hemingway, R., Rohling, E. J., Challenor, P. G., Medina-Elizalde, M., & Lester, A. J. (2011a). Sea-level probability for the last deglaciation: A statistical analysis of far-field records. *Global and Planetary Change*, *79*(3-4), 193-203.

Stanford, J. D., Rohling, E. J., Bacon, S., & Holliday, N. P. (2011b). A review of the deep and surface currents around Eirik Drift, south of Greenland: Comparison of the past with the present. *Global and Planetary Change*, *79*(3-4), 244-254.

Stow, D. A. V., Faugères, J.-C., Howe, J. A., Pudsey, C. J., & Viana, A. R. (2002). Bottom currents, contourites and deep-sea sediment drifts: current state-of-the-art. In *Deep-water Contourite systems: Modern Drifts and Ancient Series, Seismic and Sedimentary Characteristics* (22 ed., pp. 7-20). Geological Society of London.

Stuiver, M., Pearson, G. W., & Braziunas, T. (1986). Radiocarbon Age Calibration of Marine Samples back to 9000 Cal Yr BP. *Radiocarbon*, *28*(2B), 980-1021.

Swift, J. H., & Aagaard, K. (1981). Seasonal transitions and water mass formation in the Iceland and Greenland seas. *Deep-Sea Research*, *28A*(10), 1107-1129.

Swift, J. H. (1984). The circulation of the Denmark Strait and Iceland-Scotland overflow waters in the North Atlantic. *Deep-Sea Research*, *31*(11), 1339-1355.

Talley, L. D., Pickard, G. L., Emery, W. J., & Swift, J. H. (2011). Atlantic Ocean. In *Descriptive Physical Oceanography* (pp. 245-301).

Tanhua, T., Olsson, K. A., & Jeansson, E. (2008). Tracer Evidence of the Origin and Variability of Denmark Strait Overlow Water. In R. R. Dickson, J. Meincke, & P. Rhines (Eds.), *Arctic-Subarctic Ocean Fluxes* (pp. 475-503). Springer.

Taylor, P. C., Cai, M., Hu, A., Meehl, J., Washington, W., & Zhang, G. J. (2013). A Decomposition of Feedback Contributions to Polar Warming Amplification. *Journal of Climate*, *26*(18), 7023-7043.

Teller, J. T., Leverington, D., & Mann, J. D. (2002). Freshwater outbursts to the oceans from glacial Lake Agassiz and their role in climate change during the last deglaciation. *Quaternary Science Reviews*, *21*(8-9), 879-887.

Thiagarajan, N., Subhas, A. V., Southon, J. R., Eiler, J. M., & Adkins, J. F. (2014). Abrupt pre-Bolling-Allerod warming and circulation changes in the deep ocean. *Nature*, *511*(7507), 75-78.

Thiede, J. (1975). Distribution of foraminifera in surface waters of a coastal upwelling area. *Nature*, *253*(5494), 712-714.

Tolderlund, D. S., & Bé, A. W. H. (1971). Seasonal Distribution of Planktonic Foraminifera in the Western North Atlantic. *Micropaleontology*, *17*(3), 297-329.

Urey, H. C. (1947). The Thermodynamics Properties of Isotopic Substances. *The Journal of the Chemical Society*(0), 562-581.

Volkmann, R. (2000). Planktic foraminifers in the outer Laptev Sea and the Fram Strait - Modern distribution and ecology. *Journal of Foraminiferal Research*, *30*(3), 157-176.

Våge, K., Pickart, R. S., Spall, M. A., Moore, G. W. K., Valdimarsson, H., Torres, D. J., Erofeeva, S. Y., & Nilsen, J. E. Ø. (2013). Revised circulation scheme north of the Denmark Strait. *Deep Sea Research Part I: Oceanographic Research Papers*, *79*, 20-39.

Walker, M. (2005). *Quaternary Dating Methods*. John Wiley & Sons, Incorporated.

Weaver, A. J., & Hughes, T. M. C. (1994). Rapid interglacial climate fluctuations driven by North Atlantic ocean circulation. *Nature*, *367*(6462), 447-450.

Williams, K. M. (1993). Ice Sheet and Ocean Interactions, Margin of the East Greenland Ice Sheet (14 Ka to Present): Diatom Evidence. *Paleoceanography*, *8*(1), 69-83.

Wold, C. N. (1994). Cenozoic sediment accumulation on drifts in the northern North Atlantic. *Paleoceanography*, *9*(6), 917-941.

Young, N. E., Briner, J. P., Miller, G. H., Lesnek, A. J., Crump, S. E., Thomas, E. K., Pendleton, S. L., Cuzzone, J., Lamp, J., Zimmerman, S., Caffee, M., & Schaefer, J. M. (2020). Deglaciation of the Greenland and Laurentide ice sheets interrupted by glacier advance during abrupt coolings. *Quaternary Science Reviews*, *229*, 1-30.

Žarić, S., Donner, B., Fischer, G., Mulitza, S., & Wefer, G. (2005). Sensitivity of planktic foraminifera to sea surface temperature and export production as derived from sediment trap data. *Marine Micropaleontology*, *55*(1-2), 75-105.

Appendix A

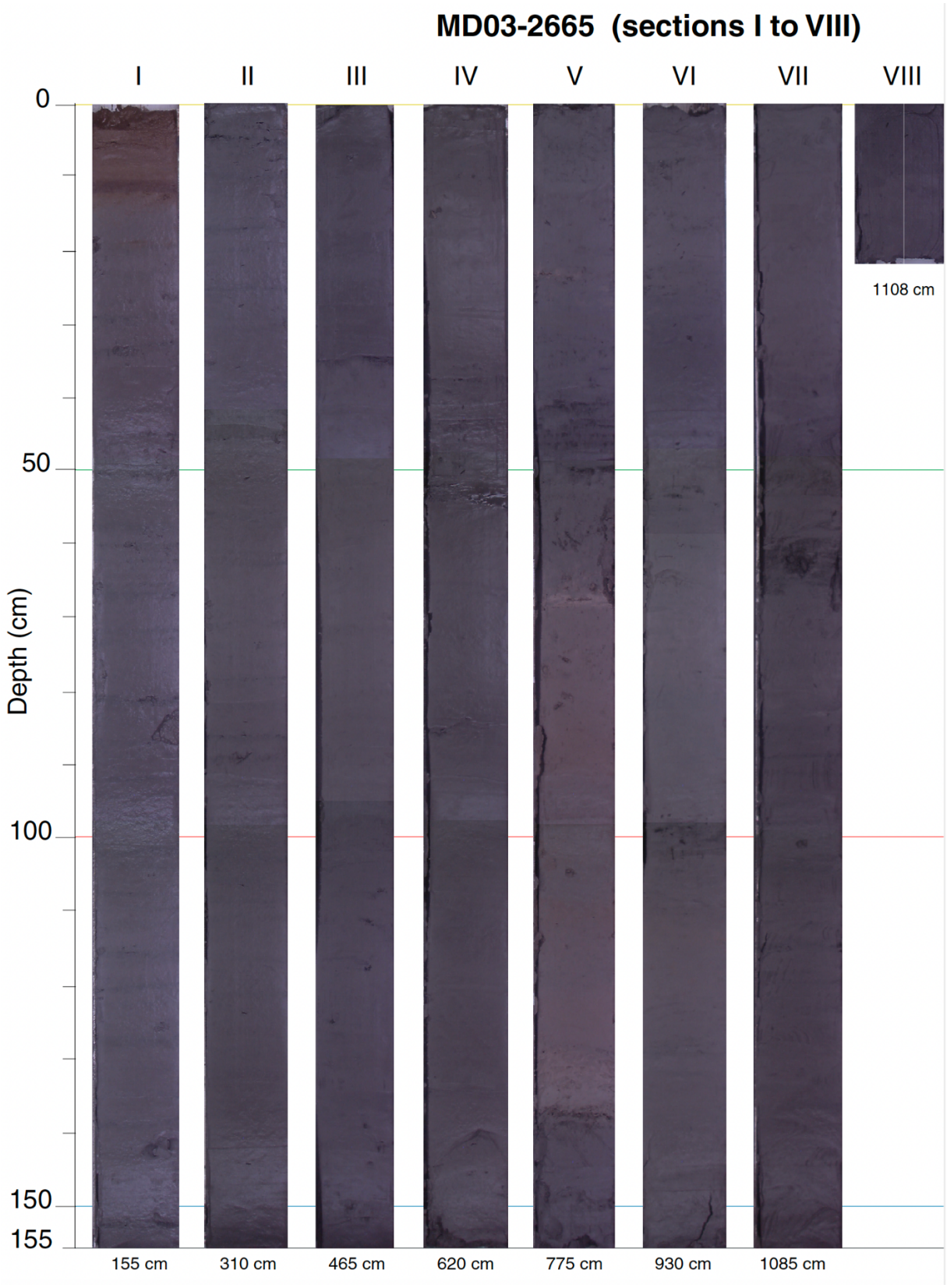
MD03-2665 (sections I to VIII)
I
II
III
IV
V
VI
VII
VIII
0
50
100
150
155
Depth (cm)
1108 cm
155 cm
310 cm
465 cm
620 cm
775 cm
930 cm
1085 cm

Appendix B

$\delta^{18}O$ and $\delta^{13}C$ measurements of MD03-2665.

Depth (cm)	NPS $\delta^{18}O$	NPS $\delta^{13}C$
0	2,427	0,647
1		
2	2,24	0,72
3	2,53	0,628
4		
5		
6		
7		
8	2,482	0,6
9		
10	2,47	0,69
11		
12	2,54	0,6
13		
14		
15		
16	2,433	0,6525
17		
18		
19		
20	2,413	0,573
21		
22		
23		
24	2,3275	0,684
25		
26		
27		
28	2,511	0,684
29		
30	2,48	0,61
31		
32	2,325	0,538
33		
34		
35		

Depth (cm)	NPS $\delta^{18}O$	NPS $\delta^{13}C$
36	2,4	0,5165
37		
38		
39		
40	2,319	0,567
41		
42		
43		
44	2,258	0,506
45		
46		
47		
48	2,258	0,506
49		
50	2,37	0,59
51		
52	2,365	0,628
53		
54		
55		
56	2,274	0,554
57		
58		
59		
60	2,44	0,66
61		
62		
63		
64	2,312	0,557
65		
66		
67		
68	2,3315	0,519
69		
70	2,37	0,59
71		

Depth (cm)	NPS $\delta^{18}O$	NPS $\delta^{13}C$
72	2,5225	0,691
73		
74		
75		
76	2,471	0,626
77		
78		
79		
80	2,487	0,572
81		
82		
83		
84	2,4345	0,6065
85		
86		
87		
88	2,448	0,635
89		
90	2,45	0,69
91		
92	2,421	0,6655
93		
94		
95		
96	2,3205	0,6205
97		
98		
99		
100	2,35	0,558
101		
102		
103		
104	2,28	0,611
105		
106		
107		
108		
109	2,311	0,6525
110	2,24	0,61
111		
112		

Depth (cm)	NPS $\delta^{18}O$	NPS $\delta^{13}C$
113	2,424	0,6655
114		
115		
116		
117	2,3385	0,617
118		
119		
120	2,41	0,73
121	2,505	0,669
122		
123		
124		
125	2,492	0,7075
126		
127		
128		
129	2,447	0,6095
130	2,39	0,63
131		
132		
133	2,453	0,681
134		
135		
136		
137	2,419	0,7735
138		
139		
140	2,44	0,61
141	2,388	0,7585
142		
143		
144		
145	2,4255	0,642
146		
147		
148		
149	2,472	0,715
150	2,43	0,62
151		
152		
153	2,463	0,6605

Depth (cm)	NPS $\delta^{18}O$	NPS $\delta^{13}C$
154		
155		
156		
157	2,451	0,649
158		
159		
160	2,21	0,52
161	2,3475	0,6875
162		
163		
164	2,256	0,694
165		
166		
167		
168	2,462	0,6005
169		
170	2,38	0,49
171		
172	2,318	0,6025
173		
174		
175		
176	2,3825	0,6265
177		
178		
179		
180	2,285	0,5
181		
182		
183		
184	2,347	0,6205
185		
186		
187		
188	2,34	0,5745
189		
190	2,31	0,47
191		
192		
193		
194	2,255	0,5745

Depth (cm)	NPS $\delta^{18}O$	NPS $\delta^{13}C$
195		
196		
197		
198	2,2855	0,4785
199		
200	2,44	0,59
201		
202	2,3415	0,589
203		
204		
205	2,432	0,657
206	2,448	0,675
207		
208		
209		
210	2,24	0,43
211		
212		
213		
214	2,2035	0,425
215		
216		
217		
218	2,288	0,5545
219		
220	2,36	0,56
221		
222	2,472	0,582
223		
224		
225		
226	2,226	0,5
227		
228		
229		
230		
231	2,24	0,343
232		
233		
234	2,239	0,5065
235		

Depth (cm)	NPS $\delta^{18}O$	NPS $\delta^{13}C$
236		
237		
238	2,272	0,517
239		
240	2,22	0,48
241		
242	2,2205	0,473
243		
244		
245	2,261	0,4835
246		
247		
248		
249		
250	2,2	0,41
251		
252		
253	2,219	0,534
254		
255		
256		
257		
258	2,22	0,39
259	2,1	0,49
260	2,14	0,25
261	2,22	0,39
262	2,28	0,62
263	2,31	0,51
264	2,18	0,42
265	2,27	0,48
266	2,26	0,38
267	2,12	0,31
268	2,22	0,49
269	2,3	0,57
270	2,34	0,4
271	2,19	0,53
272	2,32	0,42
273	2,2	0,37
274	2,13	0,37
275	2,22	0,5
276	2,22	0,51

Depth (cm)	NPS $\delta^{18}O$	NPS $\delta^{13}C$
277	2,32	0,53
278	2,21	0,43
279	2,13	0,32
280	2,25	0,35
281	2,15	0,36
282	2,19	0,48
283	2,24	0,44
284	2,12	0,4
285	2,18	0,4
286	2,16	0,42
287	2,22	0,31
288	2,16	0,26
289	2,27	0,33
290	2,32	0,36
291	2,34	0,46
292	2,28	0,45
293	2,17	0,22
294	2,12	0,33
295	2,29	0,41
296	2,13	0,25
297	2,13	0,24
298	2,25	0,32
299	2,3	0,4
300		
301	2,39	0,36
302	2,4	0,55
303	2,51	0,37
304	2,4	0,36
305	2,49	0,41
306	2,41	0,48
307	2,42	0,38
308	2,5	0,43
309	2,21	0,24
310	2,22	0,16
311	2,23	0,23
312	2,25	0,35
313	2,2	0,36
314	2,23	0,32
315		
316	2,3	0,345
317	2,4	0,23

Depth (cm)	NPS $\delta^{18}O$	NPS $\delta^{13}C$
318	2,28	0,27
319	2,33	0,46
320	2,5	0,37
321	2,57	0,25
322	2,4	0,45
323	2,44	0,34
324	2,5	0,3
325	2,64	0,3515
326	2,66	0,45
327	2,61	0,41
328	2,38	0,33
329	2,33	0,32
330		
331	2,27	0,33
332		
333		
334		
335	2,24	0,32
336	2,23	0,12
337	2,25	0,27
338	2,205	0,32
339	2,18	0,24
340	2,15	0,32
341	2,14	0,15
342	2,2	0,38
343	2,16	0,23
344	2,25	0,33
345	2,36	0,41
346	2,19	0,36
347	2,27	0,32
348		
349	2,24	0,34
350	2,25	0,33
351	2,35	0,29
352	2,21	0,28
353	2,34	0,5
354	2,4	0,46
355	2,31	0,35
356	2,19	0,32
357	2,43	0,32
358	2,32	0,44

Depth (cm)	NPS $\delta^{18}O$	NPS $\delta^{13}C$
359	2,28	0,36
360	2,37	0,33
361	2,45	0,38
362	2,38	0,19
363	2,22	0,33
364	2,48	0,4
365	2,27	0,37
366	2,18	0,35
367	2,36	0,2
368	2,27	0,17
369	2,23	0,2
370	2,53	0,35
371	2,48	0,36
372	2,43	0,27
373	2,37	0,44
374	2,3	0,18
375	2,4	0,42
376	2,31	0,09
377	2,41	0,19
378	2,49	0,4
379	2,44	0,365
380	2,31	0,17
381	2,37	0,28
382	2,22	0,09
383	2,44	0,36
384	2,25	0,18
385	2,38	0,24
386	2,57	0,4
387	2,63	0,38
388	2,55	0,26
389	2,38	0,29
390	2,365	0,3
391	2,56	0,34
392	2,36	0,2
393	2,41	0,31
394	2,3	0,35
395	2,4	0,32
396	2,38	0,32
397	2,23	0,2
398		
399		

Depth (cm)	NPS $\delta^{18}O$	NPS $\delta^{13}C$
400	2,36	0,36
401		
402		
403		
404		
405	2,65	0,36
406	2,56	0,34
407	2,48	0,02
408	2,72	0,42
409	2,52	0,11
410	2,67	0,32
411	2,64	0,35
412	2,63	0,29
413	2,45	0,22
414		
415	2,38	0,22
416	2,59	0,4
417	2,51	0,35
418	2,58	0,31
419	2,44	0,18
420	2,67	0,41
421	2,68	0,32
422	2,53	0,24
423	2,57	0,27
424		
425	2,48	0,29
426	2,68	0,36
427	2,65	0,32
428	2,54	0,25
429	2,68	0,37
430	2,62	0,25
431	2,74	0,27
432	2,65	0,25
433	2,67	0,29
434		
435	2,63	0,14
436	2,58	0,28
437	2,66	0,18
438	2,72	0,24
439	2,64	0,24
440	2,73	0,37

Depth (cm)	NPS $\delta^{18}O$	NPS $\delta^{13}C$
441	2,6	0,33
442	2,66	0,33
443	2,69	0,31
444		
445	2,65	0,31
446	2,58	0,1
447	2,66	0,23
448	2,6	0,31
449	2,66	0,14
450	2,77	0,27
451	2,59	0,31
452	2,74	0,35
453	2,69	0,3
454		
455	2,67	0,2
456	2,67	0,19
457	2,6	0,14
458	2,57	0,3
459	2,67	0,19
460	2,9	0,42
461	2,72	0,22
462	2,72	0,18
463	2,75	0,38
464		
465	2,86	0,31
466	2,68	0,32
467	2,88	0,27
468	2,84	0,32
469	2,79	0,38
470		
471	2,83	0,29
472	2,91	0,29
473	2,79	0,27
474	2,84	0,29
475	2,93	0,36
476	2,76	0,26
477	2,81	0,27
478	2,81	0,31
479	3,54	0,28
480		
481	2,79	0,14

Depth (cm)	NPS $\delta^{18}O$	NPS $\delta^{13}C$
482	3,08	0,27
483	3,4	0,38
484	3,65	0,29
485	3,1	0,3
486	3,48	0,55
487	3,12	0,3
488	3,24	0,32
489	3,09	0,41
490		
491	3,37	0,31
492	3,21	0,12
493	3,03	0,28
494	2,81	0,24
495	3,09	0,3
496	2,76	0,29
497	3,11	0,46
498	3,18	0,48
499	2,86	0,09
500		
501	2,91	0,19
502	2,66	0,1
503	2,73	0,21
504		
505		
506		
507		
508	2,9	0,09
509	2,64	-0,04
510		
511		
512		
513	3,06	0,38
514	2,74	0,33
515	2,84	0,32
516	3,02	0,29
517	2,7	0,25
518	2,87	0,21
519	2,91	0,28
520		
521	2,88	0,17
522	2,56	0,22

Depth (cm)	NPS $\delta^{18}O$	NPS $\delta^{13}C$
523	2,82	0,24
524	2,89	0,29
525	2,8	0,28
526	2,75	0,22
527	3,12	0,14
528	2,72	0,29
529	2,72	0,23
530		
531	3,21	0,08
532	3,47	0,29
533	3,23	0,29
534	2,88	0,28
535	2,98	-0,01
536	3,16	0,21
537	2,74	0,17
538	2,75	0,02
539		
540		
541		
542		
543		
544	2,67	0,31
545	2,69	0,4
546	2,94	0,27
547	3,16	0,33
548	3,2	0,41
549	2,79	0,33
550		
551	2,79	0,23
552	3,09	0,17
553	2,89	0,32
554	2,94	0,23
555	2,91	0,32
556	2,88	0,39
557	2,77	0,35
558	3,13	0,46
559	2,91	0,28
560		
561	3,27	0,31
562	2,89	0,18
563	2,93	0,16

Depth (cm)	NPS $\delta^{18}O$	NPS $\delta^{13}C$
564	3,11	0,14
565	2,9	0,26
566	3,35	0,3
567	2,89	0,15
568	2,85	0,14
569	2,95	0,24
570		
571	2,99	0,32
572	3,24	0,18
573	3,07	0,29
574	2,89	0,13
575	3,21	0,12
576	2,87	0,21
577	2,96	0,19
578	3,2	0,19
579	2,93	0,3
580		
581	2,94	0,16
582	3,1	0,27
583	3,02	0,35
584	3,22	0,34
585	2,91	0,19
586	2,86	0,21
587	3,18	0,28
588	3,22	0,36
589	3,13	0,15
590		
591	2,91	0,39
592	2,92	0,21
593	2,96	0,28
594	3,45	0,4
595	3,36	0,44
596	3,33	0,38
597	3,24	0,44
598	3,09	0,3
599	3,34	0,36
600		
601	3,64	0,35
602	3,47	0,19
603	3,58	0,29
604	3,5	0,26

Depth (cm)	NPS $\delta^{18}O$	NPS $\delta^{13}C$
605	3,4	0,32
606	3,62	0,23
607	3,62	0,22
608	3,57	0,22
609	3,6	0,24
610		
611	3,62	0,14
612	3,78	0,24
613	3,57	0,2
614	3,59	0,26
615	3,81	0,35
616	3,7	0,33
617	3,82	0,14
618	3,77	0,2
619	3,65	0,24
620		
621	3,48	0,13
622	3,54	0,2
623	3,46	0,19
624	3,46	0,13
625	3,44	0,16
626	3,42	0,01
627	3,48	0,09
628	3,51	-0,08
629	3,5	-0,08
630	3,48	0,05
631	3,39	0,06
632	3,71	0,11
633	3,55	-0,03
634	3,43	-0,08
635	3,48	-0,12
636	3,44	0
637	3,46	0,01
638	3,54	-0,05
639	3,5	-0,09
640	4,19	-0,02
641	4,28	-0,18
642	4,15	-0,1
643	4,18	-0,04
644	3,53	-0,02
645	4,64	-0,1

Depth (cm)	NPS $\delta^{18}O$	NPS $\delta^{13}C$
646	4,34	-0,12
647	4,41	-0,05
648	4,43	0,02
649	4,58	-0,19
650	4,7	-0,1
651	4,47	0,04
652	4,57	0,03
653	4,69	0,09
654	4,55	0,06
655	4,72	0,11
656	4,63	0,1
657	4,64	0,09
658	4,81	0,28
659	4,51	-0,03
660	4,69	0,18
661	4,63	0,13
662	4,61	0,13
663	4,67	-0,08
664	4,73	0,14
665	4,8	0,01
666	4,75	0,03
667	4,63	0,01
668	4,64	0,11
669	4,73	0,04
670		
671	4,56	0,16
672	4,75	-0,03
673	4,65	0,1
674	4,67	-0,04
675	4,41	-0,22
676	4,55	-0,06
677	4,56	-0,02
678	4,71	0,15
679	4,78	0,13
680		
681	4,62	-0,09
682	4,41	-0,01
683	4,35	0,06
684	4,24	-0,14
685	4,3	0,04
686	4,51	-0,06

Depth (cm)	NPS $\delta^{18}O$	NPS $\delta^{13}C$
687	4,48	0,06
688	4,48	-0,15
689	4,41	0,1
690		
691	4,2	-0,03
692	4,15	0,01
693	4,43	0,07
694	4,5	0,01
695	4,33	0,06
696	4,19	-0,01
697	4,29	0,25
698	4,3	0,15
699	4,25	0,09
700		

Appendix C

Foraminiferal assemblages and lithic counts.

Core	Depth (cm)	*N. pachyderma (s)*	*N. incompta*	*T. quinqueloba*	*G. bulloides*	*G. glutinata*	*G. inflata*	*O. universa*	OTHER	Number of splits	Total counts	Total number of Benthic foraminifera	Number of IRD grains	IRD %	*N. pachyderma coiling ratio (%)*	*N. pachyderma (s) %*	*N. incompta %*	*T. quinqueloba %*	*G. bulloides %*	*G. glutinata %*	*G. inflata %*
MD03-2665	400	114	55	230	107	4	5			3	515	10	0	0,00	67,46	22,14	10,68	44,66	20,78	0,78	0,97
MD03-2665	404	75	14	241	47					3	377	7	0	0,00	84,27	19,89	3,71	63,93	12,47	0,00	0,00
MD03-2665	408	65	20	159	56		3	1		5	304	5	0	0,00	76,47	21,38	6,58	52,30	18,42	0,00	0,99
MD03-2665	412	59	12	127	45		26		1	5	270	9	0	0,00	83,10	21,85	4,44	47,04	16,67	0,00	9,63
MD03-2665	416	75	35	190	53		7			3	360	15	0	0,00	68,18	20,83	9,72	52,78	14,72	0,00	1,94
MD03-2665	420	58	14	151	20	2	2		4	4	251	2	0	0,00	80,56	23,11	5,58	60,16	7,97	0,80	0,80
MD03-2665	424	157	28	132	42	13	13			3	385	8	0	0,00	84,86	40,78	7,27	34,29	10,91	3,38	3,38
MD03-2665	428	102	26	150	36	17	6			4	337	12	0	0,00	79,69	30,27	7,72	44,51	10,68	5,04	1,78
MD03-2665	432	99	34	140	28	5	1			5	307	13	0	0,00	74,44	32,25	11,07	45,60	9,12	1,63	0,33
MD03-2665	436	89	44	99	42	8	6			4	288	11	0	0,00	66,92	30,90	15,28	34,38	14,58	2,78	2,08
MD03-2665	440	125	68	172	34	7	9			4	415	16	0	0,00	64,77	30,12	16,39	41,45	8,19	1,69	2,17
MD03-2665	444	176	54	197	22	16	6		3	2	474	13	0	0,00	76,52	37,13	11,39	41,56	4,64	3,38	1,27
MD03-2665	448	115	57	121	39	20	10			3	362	11	0	0,00	66,86	31,77	15,75	33,43	10,77	5,52	2,76
MD03-2665	452	204	82	106	93	20	18		2	3	525	22	0	0,00	71,33	38,86	15,62	20,19	17,71	3,81	3,43
MD03-2665	456	83	42	83	66	17	3			2	294	29	0	0,00	66,40	28,23	14,29	28,23	22,45	5,78	1,02
MD03-2665	461	100	18	156	53	10	3		1	3	341	11	0	0,00	84,75	29,33	5,28	45,75	15,54	2,93	0,88
MD03-2665	464	113	29	39	56	13	4		1	3	255	7	0	0,00	79,58	44,31	11,37	15,29	21,96	5,10	1,57
MD03-2665	468	133	36	21	46	15	5			3	256	13	0	0,00	78,70	51,95	14,06	8,20	17,97	5,86	1,95
MD03-2665	472	130	74	138	42	13	8			4	405	11	0	0,00	63,73	32,10	18,27	34,07	10,37	3,21	1,98
MD03-2665	476	99	32	74	30	13	1		3	4	252	10	0	0,00	75,57	39,29	12,70	29,37	11,90	5,16	0,40
MD03-2665	481	90	21	61	114	10	12			3	308	36	0	0,00	81,08	29,22	6,82	19,81	37,01	3,25	3,90
MD03-2665	484	123	9	48	98	12	4			1	294	53	0	0,00	93,18	41,84	3,06	16,33	33,33	4,08	1,36
MD03-2665	488	247	8	46	72	8	4			2	385	34	0	0,00	96,86	64,16	2,08	11,95	18,70	2,08	1,04
MD03-2665	492	146	13	24	48	8	8			2	247	26	1	0,36	91,82	59,11	5,26	9,72	19,43	3,24	3,24
MD03-2665	496	99	6	61	85	16	5			2	272	16	0	0,00	94,29	36,40	2,21	22,43	31,25	5,88	1,84
MD03-2665	500	42		15	19	1	1			0	78		0	0,00	100,00	53,85	0,00	19,23	24,36	1,28	1,28
MD03-2665	503	19	2	10	18	1				0	50	1	0	0,00	90,48	38,00	4,00	20,00	36,00	2,00	0,00
MD03-2665	508	64	15	133	209	18	54			0	493	25	0	0,00	81,01	12,98	3,04	26,98	42,39	3,65	10,95
MD03-2665	512	16	11	85	23	7	4		2	0	148	12	4	2,44	59,26	10,81	7,43	57,43	15,54	4,73	2,70

MD03-2665	**516**	126	12	88	45	5	5			3	**281**	26	0	0,00	91,30	44,84	4,27	31,32	16,01	1,78	1,78
MD03-2665	**520**	198	25	93	106	10	8			3	**440**	32	0	0,00	88,79	45,00	5,68	21,14	24,09	2,27	1,82
MD03-2665	**524**	79	6	75	76	10	6	1		3	**253**	27	0	0,00	92,94	31,23	2,37	29,64	30,04	3,95	2,37
MD03-2665	**528**	79	13	89	70	12	9			2	**272**	22	0	0,00	85,87	29,04	4,78	32,72	25,74	4,41	3,31
MD03-2665	**532**	124	27	51	80	6	17	1		3	**306**	28	1	0,30	82,12	40,52	8,82	16,67	26,14	1,96	5,56
MD03-2665	**536**	109	14	132	68	11	4			3	**338**	15	0	0,00	88,62	32,25	4,14	39,05	20,12	3,25	1,18
MD03-2665	**541**	12	4	32	13	1				0	**62**	5	0	0,00	75,00	19,35	6,45	51,61	20,97	1,61	0,00
MD03-2665	**544**	126	22	79	56	13	8		1	1	**305**	28	0	0,00	85,14	41,31	7,21	25,90	18,36	4,26	2,62
MD03-2665	**548**	92	18	84	69	11	8			4	**282**	19	1	0,33	83,64	32,62	6,38	29,79	24,47	3,90	2,84
MD03-2665	**552**	167	23	94	65	3	4			4	**356**	29	0	0,00	87,89	46,91	6,46	26,40	18,26	0,84	1,12
MD03-2665	**556**	109	10	77	75	6	5			4	**282**	29	0	0,00	91,60	38,65	3,55	27,30	26,60	2,13	1,77
MD03-2665	**560**	148	24	165	147	9	6			3	**499**		0	0,00	86,05	29,66	4,81	33,07	29,46	1,80	1,20
MD03-2665	**564**	268	31	175	165	9	1			3	**649**	35	2	0,29	89,63	41,29	4,78	26,96	25,42	1,39	0,15
MD03-2665	**568**	180	22	112	83	4	2		2	3	**405**	14	1	0,24	89,11	44,44	5,43	27,65	20,49	0,99	0,49
MD03-2665	**572**	164	13	64	51	3	1			4	**296**		1	0,32	92,66	55,41	4,39	21,62	17,23	1,01	0,34
MD03-2665	**576**	133	12	84	73	1				5	**303**	6	0	0,00	91,72	43,89	3,96	27,72	24,09	0,33	0,00
MD03-2665	**580**	115	12	57	64	5	3		1	4	**257**	5	1	0,38	90,55	44,75	4,67	22,18	24,90	1,95	1,17
MD03-2665	**584**	195	13	114	103	5	1			3	**431**	22	3	0,66	93,75	45,24	3,02	26,45	23,90	1,16	0,23
MD03-2665	**588**	193	5	23	20	3	1			2	**245**	17	3	1,13	97,47	78,78	2,04	9,39	8,16	1,22	0,41
MD03-2665	**592**	266	12	21	41	2	1			2	**343**	22	4	1,08	95,68	77,55	3,50	6,12	11,95	0,58	0,29
MD03-2665	**596**	227	6	11	15	4	1			7	**264**	3	12	4,30	97,42	85,98	2,27	4,17	5,68	1,52	0,38
MD03-2665	**600**	278	9	1	5					4	**293**	2	27	8,39	96,86	94,88	3,07	0,34	1,71	0,00	0,00
MD03-2665	**604**	398	15	2	10	2	1			9	**428**	1	15	3,38	96,37	92,99	3,50	0,47	2,34	0,47	0,23
MD03-2665	**608**	266	6		5					6	**277**	3	63	18,37	97,79	96,03	2,17	0,00	1,81	0,00	0,00
MD03-2665	**612**	252	6	8	9					8	**275**	1	8	2,82	97,67	91,64	2,18	2,91	3,27	0,00	0,00
MD03-2665	**617**	307	3		2				2	4	**314**	4	41	11,42	99,03	97,77	0,96	0,00	0,64	0,00	0,00
MD03-2665	**620**	299	4	1	4					3	**308**	15	24	6,92	98,68	97,08	1,30	0,32	1,30	0,00	0,00
MD03-2665	**624**	330	6	1			2			5	**339**	8	6	1,70	98,21	97,35	1,77	0,29	0,00	0,00	0,59
MD03-2665	**628**	221	13	4	9	1	3			3	**251**	3	1	0,39	94,44	88,05	5,18	1,59	3,59	0,40	1,20
MD03-2665	**632**	215	12	22	14	2	1		1	4	**267**	4	22	7,51	94,71	80,52	4,49	8,24	5,24	0,75	0,37
MD03-2665	**636**	251	3	23	28				4	7	**309**	1	16	4,91	98,82	81,23	0,97	7,44	9,06	0,00	0,00
MD03-2665	**641**	258	4	8	22		1		1	8	**294**		51	14,78	98,47	87,76	1,36	2,72	7,48	0,00	0,34
MD03-2665	**644**	255	7	5	24	1	1			8	**293**	1	10	3,29	97,33	87,03	2,39	1,71	8,19	0,34	0,34
MD03-2665	**648**	235	2	2	14				2	8	**255**	1	17	6,23	99,16	92,16	0,78	0,78	5,49	0,00	0,00
MD03-2665	**652**	419	21		7	1				2	**448**	23	805	63,09	95,23	93,53	4,69	0,00	1,56	0,22	0,00
MD03-2665	**656**	420	11							6	**431**	1	37	7,89	97,45	97,45	2,55	0,00	0,00	0,00	0,00
MD03-2665	**660**	243	12							2	**255**	2	47	15,46	95,29	95,29	4,71	0,00	0,00	0,00	0,00

MD03-2665	**664**	343	7							3	**350**	2	32	8,33	98,00	98,00	2,00	0,00	0,00	0,00	0,00
MD03-2665	**668**	418	6							7	**424**		139	24,69	98,58	98,58	1,42	0,00	0,00	0,00	0,00
MD03-2665	**672**	429	16						1	7	**446**	2	63	12,33	96,40	96,19	3,59	0,00	0,00	0,00	0,00
MD03-2665	**676**	368	11							4	**379**	10	1132	74,42	97,10	97,10	2,90	0,00	0,00	0,00	0,00
MD03-2665	**680**	331	10							7	**341**	1	268	43,93	97,07	97,07	2,93	0,00	0,00	0,00	0,00
MD03-2665	**684**	248	5							6	**253**	1	237	48,27	98,02	98,02	1,98	0,00	0,00	0,00	0,00
MD03-2665	**688**	367	8							8	**375**	2	24	5,99	97,87	97,87	2,13	0,00	0,00	0,00	0,00
MD03-2665	**692**	261	6							8	**267**		11	3,96	97,75	97,75	2,25	0,00	0,00	0,00	0,00
MD03-2665	**696**	443	12							2	**455**	7	989	68,16	97,36	97,36	2,64	0,00	0,00	0,00	0,00
MD03-2665	**700**	367	8							7	**375**	1	30	7,39	97,87	97,87	2,13	0,00	0,00	0,00	0,00

Appendix D

Radiocarbon ages from core MD03-2665 determined by accelerator mass spectrometry

Depth (cm)	Lab code [a]	Species [b]	Uncorrected ^{14}C age (yr) ± 1σ error	Calendar age BP [c] (mean probability)	1σ age range	ΔR
2	KIA	Gbull	890 ± 30	426	205-521	-24 ± 76
5	KIA	NPD	995 ± 25	477	307-621	-24 ± 76
18	KIA	Gbull	1525 ± 35	901	681-1108	-24 ± 76
38	KIA	mixed Gbull + NPS	2020 ± 30	1432	1225-1649	-24 ± 76
65	KIA	Gbull	2635 ± 30	2179	1930-2428	-24 ± 76
106	KIA	Gbull	3605 ± 45	3347	3060-3622	-24 ± 76
140	KIA	Gbull	4280 ± 30	4211	3885-4501	-24 ± 76
230	KIA	Gbull	6160 ± 30	6421	6182-6672	-24 ± 76
271	KIA	mixed Gbull + NPS	7175 ± 30	7435	7222-7613	-24 ± 76
285	KIA	mixed Gbull + NPS	7415 ± 50	7675	7492-7853	-24 ± 76
285*	KIA		4980 ± 35			
300	KIA	NPD	7895 ± 40	7906	7707-8081	-24 ± 76
313	KIA	mixed Gbull + NPS	7810 ± 35	8038	7862-8195	-24 ± 76
323	KIA	mixed Gbull + NPS	7995 ± 40	8136	7977-8289	-24 ± 76
343	KIA	mixed Gbull + NPS	7795 ± 45	8304	8158-8450	-24 ± 76
343	KIA	mixed Gbull + NPS	7870 ± 55			
350	KIA	mixed Gbull + NPS	7980 ±45	8377	8242-8536	-24 ± 76
355	KIA	mixed Gbull + NPS	8030 ±45	8438	8307-8590	-24 ± 76
364	GifA	mixed Gbull + NPS	8500 ± 90	8577	8421-8745	-24 ± 76
375	KIA	mixed Gbull + NPS	8215 ± 45	8712	8540-8906	-24 ± 76
385	KIA	mixed Gbull + NPS	8435 ± 50	8850	8670-9010	-24 ± 76
393	KIA	Gbull	8535 ± 50	8957	8792-9113	-24 ± 76
404	KIA	mixed Gbull + NPS	8705 ± 45	9092	8910-9251	-24 ± 76
430	KIA		8885 ± 45	9379	9202-9551	-24 ± 76
460	KIA		9010 ± 45	9680	9497-9860	-24 ± 76
480	KIA		9310 ± 45	9909	9723-10090	-24 ± 76
490	GifA	mixed Gbull + NPS	9460 ± 70	10023	9843-10195	-24 ± 76
495	KIA	Gbull	9275 ± 45	10070	9895-10246	-24 ± 76
535	KIA	mixed	9115 ± 45	10536	10266-10834	-24 ± 76
560	GifA	Gbull	9850 ± 60	10912	10596-11277	-24 ± 76
598	KIA	NPS	10950 ± 45	11676	11231-12144	800 ± 100
610	GifA	NPS	11770 ± 70	11929	11426-12429	800 ± 100
616	KIA	NPS	12625 ± 60	12782	12560-12916	800 ± 100
620			**12896 ± 4**	**12908**	**12876-12970**	**0**
640	KIA	NPS	15300 ± 70	14510	14203-14682	800 ± 100
644			**14692 ± 4**	**14688**	**14611-14759**	**0**
670	KIA	NPS	19160 ± 110	21152	20355-21755	800 ± 100

[a] KIA – Leibniz Labor für Altersbestimmung und Isotopenforschung, Kiel, Germany; GifA - Laboratoire des Sciences du Climat et de l'Environnement, Gif-sur-Yvette, France

[b] Gbull – *G. bulloides*; NPD – *N. pachyderma*(d); NPS – *N. pachyderma*(s)

[c] ^{14}C ages were converted into calendar ages with the CALIB v.8.2 software and the MARINE20 calibration dataset. *Uncorrected ages in black are previously published in Kleiven et al. (2008), ages in blue are unpublished ages from this study, ages in red are duplicates and not used.*

Appendix E

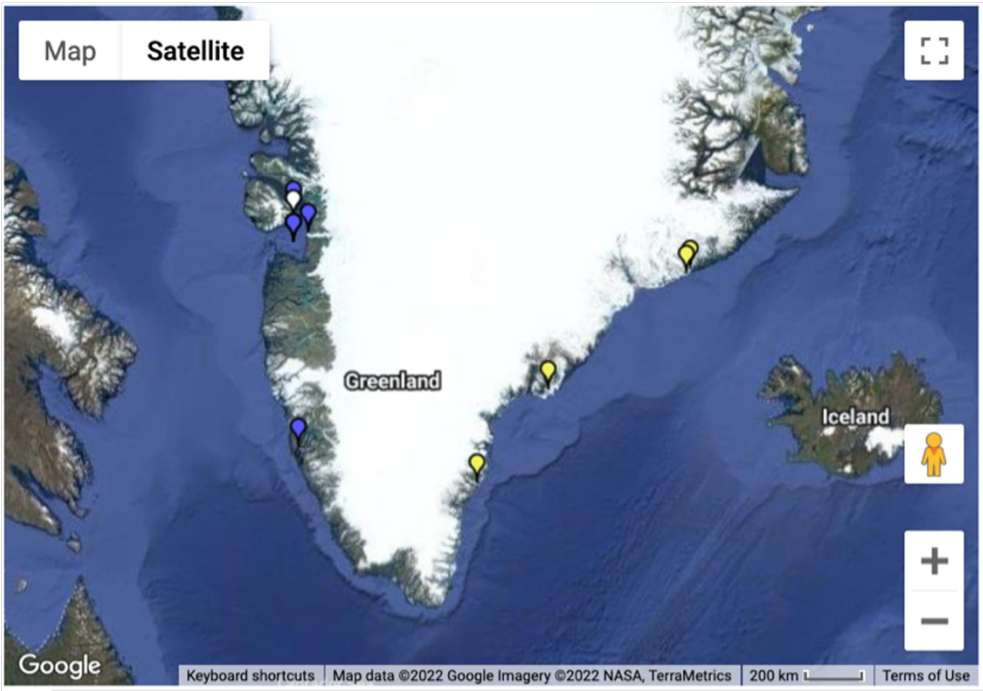

	MapNo	Lon	Lat	DeltaR	DeltaRErr	Reference	Locality	distance (km)
☐	670	-41.1200	63.2700	-32	51	Olsson, I U.:1980	Angmagssalik, E. Greenland	368
☐	669	-36.8800	65.6500	-22	69	Olsson, I U.:1980	Skjoldungen, E. Greenland	648
☐	34	-51.7500	64.2000	-31	84	Olsson, I U.:1980	Godthab, Greenland	767
☐	667	-28.7300	68.3500	-121	51	Olsson, I U.:1980	Kap Rink, E. Greenland	1073
☐	671	-28.5200	68.4200	-89	45	Olsson, I U.:1980	Kap Stephensen, E. Greenland	1085
☐	35	-51.1300	69.2200	-192	99	Olsson, I U.:1980	Jacobshavn, Greenland	1150
☐	987	-52.0000	69.0000	116	40	McNeely R., :2006	Disko, Greenland	1149
☐	990	-52.0000	69.0000	-4	25	McNeely R., :2006	Disko, Greenland	1149
☐	665	-52.0000	69.5000	-85	51	Olsson, I U.:1980	N.or W. Greenland	1195
☐	37	-52.0000	69.6800	-81	84	Olsson, I U.:1980	Mudderbugten, Disco, Greenland	1212

Calculate Average of ticked boxes ☐ Select All

MapNo	Lat	Lon	ΔR	σ
670	63.2700	-41.1200	-32	51
669	65.6500	-36.8800	-22	69
34	64.2000	-51.7500	-31	84
667	68.3500	-28.7300	-121	51
671	68.4200	-28.5200	-89	45
35	69.2200	-51.1300	-192	99
987	69.0000	-52.0000	116	40
990	69.0000	-52.0000	-4	25
665	69.5000	-52.0000	-85	51
37	69.6800	-52.0000	-81	84

npts: 10
Weighted Mean ΔR= -24
Uncertainty= 76
Explanation of calculation

$$\text{weighted mean of } \Delta R = \mu = \frac{\Sigma_i \frac{\Delta R_i}{\sigma_i^2}}{\Sigma_i \frac{1}{\sigma_i^2}}$$

where σ_i = uncertainty in ΔR_i

$$\text{weighted uncertainty in mean of } \Delta R = \frac{1}{\Sigma_i \frac{1}{\sigma_i^2}}$$

$$\text{variance of } \Delta R = \frac{\frac{1}{n-1} \cdot \Sigma_i \left(\frac{\Delta R_i - \mu}{\sigma_i} \right)^2}{\frac{1}{n} \cdot \Sigma_i \frac{1}{\sigma_i^2}}$$

$$\text{Standard Deviation of } \Delta R = \sqrt{\text{variance}}$$

The reported ΔR uncertainty is the maximum of the Standard Deviation of ΔR and the weighted uncertainty in mean of ΔR

Reference:

Data Reduction and Error Analysis for the Physical Sciences, P R Bevington, 1969, McGraw Hill.